A STUDY OF THE DIFFERENTIAL CROSS-SECTION AND ANALYZING POWERS OF THE $pp \rightarrow \pi^{+}d$ REACTION AT INTERMEDIATE ENERGIES.

by

GORDON LEWIS GILES

B.Sc. Honours Physics, University of British Columbia, 1978

M.Sc., McGill University, 1981

A THESIS SUBMITTED IN PARTIAL FULFILMENT OF

THE REQUIREMENTS FOR THE DEGREE OF

DOCTOR OF PHILOSOPHY

in

THE FACULTY OF GRADUATE STUDIES

Department of Physics

We accept this thesis as conforming

to the required standard

THE UNIVERSITY OF BRITISH COLUMBIA

February 1985

Department of Physics

The University of British Columbia
1956 Main Mall
Vancouver, Canada
V6T 1Y3

Date February, 1985

Abstract

The polarized and unpolarized differential cross-sections and the analyzing power angular distributions of the $pp \rightarrow \pi^+ d$ reaction have been measured to a statistical precision of better than one percent over several incident proton beam energies between 350 and 500 MeV for center-of-mass angles from 20° to 150°. The unpolarized differential cross-sections were measured at 350, 375, 425, and 475 MeV with unpolarized incident beams. The polarized differential cross-sections and analyzing powers were measured at 375, 450, and 498 MeV using polarized incident beams. Angular distributions of the unpolarized and polarized differential cross-sections are expanded into Legendre and Associated Legendre polynomial series respectively, and the a_i^{oo} and b_i^{no} expansion coefficients fit to the respective measurements. The resulting coefficients are compared with existing data and recent theoretical predictions.

The observation of significant non-zero a_8^{oo} coefficent is interpreted as indication of a significant contribution from the ${}^1G_4$ N-N partial wave channel at energies as low as 498 MeV.

Acknowledgements

I am grateful to my collegues E.G. Auld, G. Jones, G.J. Lolos, B.J. McParland, D. Ottewell, P.L. Walden and W.R. Falk, for their contributions during the course of this experiment. Furthermore, I would like to thank Jean Holt for her assistance with the drafting and artwork, and Dorothy Sample for her assistance with the analysis of the data. Special thanks are due to Sylvia Vecchione for her extensive assistance with the preparation of the manuscript.

I gratefully acknowledge Garth Jones, the chairman of my Ph.D. committee, for his skillful guidance throughout the course of my studies and the completion of this thesis.

Above all, I express my sincerest gratitude to my parents and family, for their continuous encouragement and support.

Table of Contents

List of Tables

List of Figures

1. INTRODUCTION

The study of the elementary pion production reaction, $pp \to \pi^+ d$, is of fundamental significance. Not only does this reaction provide insight into the fundamental process of pion creation itself, but simultaneously it provides insight into the nature of the inelastic behaviour of the nucleon-nucleon system. The understanding of this reaction with its relatively simple two-body initial and final states provides a basic element required for the description of the more general few-body systems. The $pp \to \pi^+ d$ reaction represents a special case of the more general $pp \to \pi^+ np$ reaction, one where the final state nucleons are bound (to form a deuteron). As the $pp \to \pi^+ d$ reaction and its inverse reaction ($\pi^+ d \to pp$) can both be measured in the laboratory, precise comparison of measurements of the observables (such as the differential cross-section and various spin-dependent quantities) provide a test of fundamental symmetries such as time reversal invariance. Furthermore, these two reactions represent the simplest cases of nuclear pion production (of the nuclear (p,π) reaction for example) and of nuclear pion absorption respectively, subjects of significant current interest[1,2,3].

Precision measurements of quantities such as the polarized and unpolarized differential cross-sections (and thereby the analyzing powers) of the $pp \to \pi^+ d$ reaction provide information regarding the nature of the highly inelastic intermediate state which characterizes this reaction.

The importance of spin-dependent observables of the nucleon-nucleon system has been reinforced by the observation of unexpected energy dependences of the $\Delta\sigma_L$ and $\Delta\sigma_T$ parameters of the proton-proton subsystem, (that is, the difference between total cross-sections of the parallel and anti-parallel proton spin states, where the polarization direction is either longitudinal, or transverse, to the direction of the proton's relative motion) dependences which were not at all evident in spin-independent observables[4,5]. Exotic reaction mechanisms, such as those which included a so-called "dibaryon resonance", have been proposed by some to explain such observations[6]. Whether the introduction of such mechanisms is indeed required has, however been the subject of much controversy [7,8].

Such observations have motivated interest in performing full partial-wave amplitude analyses of the reaction in order to explore the energy dependencies of the specific amplitudes. Such analyses require, however, a body of precise experimental data concerning the various polarization dependent observables.

In this thesis we describe the first precision measurements of both the spin-dependent polarized, and the spin-averaged unpolarized differential cross-sections of the $pp \rightarrow \pi^+ d$ reaction for incident proton energies from 350 to 498 MeV. In addition, we have measured and published the associated analyzing powers[9], the spin dependent quantity more generally (that is, the most often) measured.

Many provisions are designed into this experiment to ensure reliable results. A geometrically-simple two-arm apparatus (devoid of complicating magnets) was used to simplify the definition of the effective acceptance solid angle of the system. With this apparatus, differential cross-section measurements could be obtained over a large angular range in the center-of-mass system (20° to 150°), thereby permitting accurate determination of the higher-order terms in a spherical expansion of the differential cross-section. The beam current determination was carried out, in effect, through simultaneous measurement of the $pp \rightarrow pp$ elastic reaction (at 90° in the centre-of-mass system) from the same production target as that employed for the $pp \rightarrow \pi^+ d$ production. The required $pp \rightarrow pp$ elastic differential cross-sections and the associated solid angles of the pp-elastic monitor were measured prior to the pion production program. These results have since been published[10]. This method of beam current normalization has the great advantage of being independent of both the target thickness, and of the angle of the target with respect to the beam direction.

The nature of the kinematic transformation from the center-of-mass to laboratory coordinate systems is such that a forward and a backward pion are both coincident with deuterons emitted into a given laboratory solid angle. The apparatus was designed to permit simultaneous detection of these events. Because of the forward-backward symmetry of the differential cross-section (in the center-of-mass), a symmetry imposed by the fact that identical particles are involved, determination of laboratory angle dependent factors such as the system acceptance solid angles, and pion-decay and energy-loss corrections can be verified.

The small carbon background (arising from the polyethylene target material) was reduced through both the use of appropriate event selection and direct subtraction techniques. Overall, many steps have been taken throughout this experiment to ensure the reliability of our measurements of the fundamental $pp \rightarrow \pi^+ d$ reaction.

2. THEORY AND FORMALISM

2.1 THE DIFFERENTIAL CROSS-SECTIONS AND ANALYZING POWER

If a polarized proton beam is incident upon an unpolarized target, the differential cross-section $d\sigma/d\Omega$ can be written in terms of unpolarized and polarized components, that is;

$$d\sigma/d\Omega = d\sigma_0/d\Omega + \bar{P}\cdot\bar{n}\ d\sigma_1/d\Omega \tag{01}$$

where:

$d\sigma_0/d\Omega$	- Denotes the unpolarized differential cross-section.
$d\sigma_1/d\Omega$	- Denotes the polarized differential cross-section.
$\bar{P}$	- The incident proton beam polarization.

Here $\bar{n}$, is a unit vector normal to the scattering plane in the direction $\bar{k}_i \times \bar{k}_f$ (the Madison Convention). Clearly, if the incident beam is unpolarized ($|\bar{P}|=0$), then the unpolarized differential cross-section results.

If a polarized beam is to be used, then both the unpolarized and polarized differential cross-sections can be deduced from two measurements of the differential cross-section, each associated with differing orientations of the beam polarization vectors. Consider the special case of two such measurements performed with both of the beam polarization vectors perpendicular to the scattering plane and with opposite directions. Here, the dot products between the polarization vectors $\bar{P}_1$ and $\bar{P}_2$, with the unit vector $\bar{n}$, are represented by the scalar quantities $P\uparrow$ and $P\downarrow$ respectively, where;

$$P\uparrow = \bar{P}_1 \cdot \bar{n} = |\bar{P}_1| \tag{02}$$

$$P\downarrow = -\bar{P}_2 \cdot \bar{n} = |\bar{P}_2|$$

The corresponding differential cross-sections $d\sigma\uparrow/d\Omega$ and $d\sigma\downarrow/d\Omega$, then, are given by;

$$d\sigma\uparrow/d\Omega = d\sigma_0/d\Omega + P\uparrow\ d\sigma_1/d\Omega \tag{03}$$

$$d\sigma\downarrow/d\Omega = d\sigma_0/d\Omega - P\downarrow\ d\sigma_1/d\Omega$$

This system of linear equations is readily solved for the polarized and unpolarized differential cross-sections as a function of the two measured differential cross-sections and their associated polarizations; that is;

$$d\sigma_0/d\Omega = \tfrac{1}{2}(\ d\sigma\uparrow/d\Omega + d\sigma\downarrow/d\Omega\ ) \tag{04}$$

$$- \tfrac{1}{2}(\ d\sigma\uparrow/d\Omega - d\sigma\downarrow/d\Omega)\ P$$

and

$$d\sigma_1/d\Omega = (\ d\sigma\uparrow/d\Omega - d\sigma\downarrow/d\Omega\ )/(\ P\uparrow + P\downarrow\ )$$

where

$$P = \{\ (\ P\uparrow - P\downarrow\ )/(\ P\uparrow + P\downarrow\ )\ \}$$

The analyzing power A_{no}, is defined as the ratio of the polarized to unpolarized differential cross-section; that is;

$$A_{no} = (d\sigma_1/d\Omega) \ / \ (d\sigma_0/d\Omega) \qquad (05)$$

Clearly, two cross-section measurements, performed with differing beam polarizations, are required to define the analyzing power for a given experimental configuration (as is the case also for $d\sigma_1/d\Omega$).

Generally, measurement of the analyzing powers requires a less complex experimental procedure than that required for the measurement of the differential cross-section (polarized or unpolarized). Since the analyzing power is a ratio of two differential cross-sections, any systematic uncertainty in the absolute differential cross-sections (such as that due to uncertainties in solid angle, detection efficiency, and pion-decay and energy-loss corrections) simply cancel out.

2.2 PHENOMENOLOGICAL DESCRIPTIONS OF THE $pp \rightarrow \pi^+ d$ REACTION

2.3 SPIN AMPLITUDE ANALYSIS

The $pp \rightarrow \pi^+ d$ reaction can be described in terms of the spin structure of its initial and final states by a 4x3 dimensional T (transition) matrix. Each of these twelve complex amplitudes is, in turn, a function of energy and scattering angle, and is uniquely associated with a particular transition from one of the the four possible initial, to one of the three possible final spin states.

When the assumptions of parity conservation and time reversal invariance are invoked, the number of independent T matrix amplitudes reduces to six, less one arbitrary phase. Thus, there are in all, eleven independent parameters required to describe this reaction at each kinematic configuration.

When described in terms of the usual spin-triplet laboratory frame spin quantization directions[11], the T matrix has poor relativistic transformation properties. Alternatively, formalisms characterized by spin quantization directions either parallel (the helicity formalism) or transverse (the transversity formalism) to the direction of the associated particles' motion, have been developed[12,13]. The use of such formalisms is justified by the simpler relativistic transformation properties of the T matrix that result when the spin basis states are defined accordingly.

This spin amplitude formalism is also useful for providing a framework in which to conceptualize the $pp \rightarrow \pi^+ d$ reaction, in particular, to appreciate the complexity introduced by the spins of the particles, (defined, in this case, by only 6 complex amplitudes). Measurement of the angular structure of all of these amplitudes as a function of energy would require a very large number of experiments, depending, in part, on the number of angles required to define the angular distributions.

For beam energies in the $\Delta(1232)$ isobar resonance region, a description in terms of a partial wave expansion offers an attractive alternative. The partial wave formalism is based on the decomposition of each of the initial and final state wave functions into a sum over partial waves of specific angular momentum. For energies near the pion production threshold, where the centrifugal barrier limits the number of partial waves which can contribute, the system can be described in terms of a small number of partial wave amplitudes. As the energy increases, however, the number of amplitudes required to describe the system increases markedly. The various partial wave channels and the associated amplitude designations (following the notation of Mandl and Regge[14], and Blankleider and Afnan[15]) are listed in table (2.1). Also indicated in the table (2.1) are some of the possible NΔ intermediate states pertaining to the various partial wave channels.

Consider, for example, the reaction channel associated with the initial nucleon-nucleon $^1D_2$ state and the a_2 partial wave amplitude. Here, the two protons coupled to a singlet spin state (S=0) and a D state (l=2) of relative angular momentum prior to the interaction and the subsequent formation of a NΔ intermediate state. The $\frac{3}{2}$ spin of the delta can couple to the $\frac{1}{2}$ nucleon spin to form either a triplet (S=1) or a quintuplet (S=2) state. Since the total angular momentum (J=2) and the parity is conserved as the reaction proceeds, the relative motion of the NΔ system is restricted to a S state (l=0) for the quintuplet spin state, or a D state for either of these spin configurations. The NΔ

Table (2.1)

Partial Wave Channels and Amplitude Designation.

pp Initial State	NΔ Intermediate State	πd Final State	Amplitude Designation
$^{2S+1}l_J$ parity	$^{2S+1}l_J$	$^{2S+1}L_j l_J$	
$^1S_0^+$		$^3S_1 p_0^+$	a_0
$^3P_1^-$	$^{3,5}P_1^-$	$^3S_1 s_1^-$	a_1
	$^3F_1^-$	$^3S_1 d_1^-$	a_3
$^1D_2^+$	$^5S_2^+$	$^3S_1 p_2^+$	a_2
	$^{3,5}D_2^+$	$^3S_1 f_2^+$	a_7
$^3P_2^-$	$^{3,5}P_2^-$ $^{3,5}F_2^-\ldots$	$^3S_1 d_2^-$	a_4
$^3F_2^-$	$^{3,5}P_2^-$ $^{3,5}F_2^-\ldots$	$^3S_1 d_2^-$	a_5
$^3F_3^-$	$^{3,5}P_3^-$	$^3S_1 d_3^-$	a_6
	$^{3,5}F_3^-\ldots$	$^3S_1 g_3^-$	a_9
$^3F_4^-$	$^3F_4^-$	$^3S_1 g_4^-$	a_{10}
$^1G_4^+$	$^5D_4^+$	$^3S_1 f_4^+$	a_8
		$^3S_1 h_4^+$	a_{13}

Here, J represents the total angular momentum of each state, and l, the relative angular momentum of the two particles. In the case of the final state, where there are three particles, j and L denote the internal quantum numbers of the deuteron.

intermediate state then decays to the final state consisting of a deuteron (simplistically designated here as a triplet np system in a S state of relative angular momentum) and a pion that is in a relative p state of angular momentum with respect to the deuteron.

Early work[16,17] indicated that the $^1D_2$ NN partial wave provided the dominant contribution to the scattering amplitude. This observation was interpreted in terms of the formation of a NΔ intermediate state of a particularly simple configuration, in particular, a state with N and Δ particles in a S (l=0) state of relative motion.

2.4 ORTHOGONAL EXPANSION OF OBSERVABLES

Observables (O^{ν}), (where ν simply labels the observable) such as the differential cross-section and the spin correlation parameters A_{ij}, (following the proposal of Niskanen[18], and using the notation of Blankleider [15]) can be expanded in terms of orthogonal functions $P_i^{\nu}((\theta))$ (typically Associated Legendre functions) containing the angular dependence. Here, the superscript ν denotes the A_{no} and $d\sigma/d\Omega$. In general, however;

$$4\pi \ (d\sigma_0/d\Omega) \ O^{\nu} = \sum_i A_i^{\nu} \ P_i^{\nu} \qquad (06)$$

where the unpolarized differential cross-section has been factored out of the expression. The expansion coefficients A_i^{ν} are, in turn, linear combinations of bilinear products of the appropriate partial wave amplitudes, defined by;

$$A_i^{\nu} = \sum_{ij} C_i^{\nu}(i,j)\ a_i\ a_j{}^* \tag{07}$$

where, finally, the C_i^{ν} coefficients are a function of the appropriate angular momentum coupling coefficients.

As an example of such expansions, the specific cases of the unpolarized differential cross-section and the analyzing powers are summarized here. The differential cross-section can be expanded in terms of the (even order) Legendre function $P_i(\cos(\theta_\pi^*))$;

$$4\pi\ (d\sigma_0/d\Omega) = \sum_{i=0,2,\ldots} a_i^{oo}\ P_i(\cos(\theta_\pi^*)) \tag{08}$$

Similarly, the analyzing powers can be expanded in terms of the first order Associated Legendre functions (of all orders), $P_i^1(\cos(\theta_\pi^*))$, that is;

$$4\pi\ (d\sigma_0/d\Omega)\ A_{no} = \sum_{i=1,2,\ldots} b_i^{no}\ P_i^1(\cos(\theta_\pi^*)) \tag{09}$$

The coefficients relating the a_i^{oo} and b_i^{no} expansion coefficients to the (sum of) bilinear amplitude products[15] are listed in table (2.2) and table (2.3) respectively, for amplitudes up to a_8.

When considering the relationship of the unpolarized differential cross-section to the partial wave amplitudes, through the sum of appropriate bilinear amplitude combinations, several observations can be made. The a_0^{oo} coefficient (which is simply the total cross-section in this representation) depends only on the sum of the squares of the partial wave amplitudes. Therefore, it would be expected

Table (2.2)

The Differential Cross-Section Partial Wave Expansion Coefficients.

Bilinear Amplitude Products	a_0^{00}	a_2^{00}	a_4^{00}	a_6^{00}
$\|a_0\|^2$	1/4	0	0	0
$\|a_1\|^2$	1/4	0	0	0
$\|a_2\|^2$	1/4	1/4	0	0
$\|a_3\|^2$	1/4	-1/8	0	0
$\|a_4\|^2$	5/12	5/24	0	0
$\|a_5\|^2$	5/28	5/49	-5/49	0
$\|a_6\|^2$	1/4	3/14	1/28	0
$\|a_7\|^2$	1/4	2/7	3/14	0
$\|a_8\|^2$	1/4	25/84	81/308	25/132
$Re\{a_0a_2^*\}$	0	$-1\surd 1/2$	0	0
$Re\{a_0a_7^*\}$	0	$1/2\surd 3$	0	0
$Re\{a_0a_8^*\}$	0	0	-1	0
$Re\{a_1a_3^*\}$	0	$1/2\surd 1/2$	0	0
$Re\{a_1a_4^*\}$	0	$1/2\surd 5/2$	0	0
$Re\{a_1a_5^*\}$	0	$1/2\surd 5/7$	0	0
$Re\{a_1a_6^*\}$	0	$\surd 1/2$	0	0
$Re\{a_2a_7^*\}$	0	$-1/7\surd 3/2$	$-3/7\surd 6$	0
$Re\{a_2a_8^*\}$	0	$9/7\surd 1/2$	$5/7\surd 1/2$	0
$Re\{a_3a_4^*\}$	0	$1/4\surd 5$	0	0
$Re\{a_3a_5^*\}$	0	$1/2\surd 5/14$	0	0
$Re\{a_3a_6^*\}$	0	-1/7	9/14	0
$Re\{a_4a_5^*\}$	0	$-5/14\surd 1/14$	$10/7\surd 2/7$	0
$Re\{a_4a_6^*\}$	0	$1/7\surd 5$	$5/14\surd 5$	0
$Re\{a_5a_6^*\}$	0	$1/7\surd 10/7$	$5/7\surd 5/14$	0
$Re\{a_7a_8^*\}$	0	$-1/7\surd 1/3$	$-15/77\surd 3$	-25/1

The $\surd$ symbol implies the square root of the quantity to its right.

Table (2.3)

The Analyzing Power Partial Wave Expansion Coefficients.

Bilinear Amplitude Products	b_1^{no}	b_2^{no}	b_3^{no}	b_4^{no}	b_5^{no}
$Im\{a_0a_1^*\}$	-1/2√1/2	0	0	0	0
$Im\{a_0a_3^*\}$	1/2	0	0	0	0
$Im\{a_0a_6^*\}$	0	0	-1/4	0	0
$Im\{a_1a_2^*\}$	1/4	0	0	0	0
$Im\{a_1a_4^*\}$	0	1/6√5/2	0	0	0
$Im\{a_1a_5^*\}$	0	-1/4√5/7	0	0	0
$Im\{a_1a_7^*\}$	0	0	1/2√1/6	0	0
$Im\{a_1a_8^*\}$	0	0	1/4√1/2	0	0
$Im\{a_2a_3^*\}$	1/20√1/2	0	-3/10√1/2	0	0
$Im\{a_2a_4^*\}$	-3/4√1/10	0	-1/2√1/10	0	0
$Im\{a_2a_5^*\}$	-3/4√1/35	0	-1/2√1/35	0	0
$Im\{a_2a_6^*\}$	3/5√1/2	0	3/20√1/2	0	0
$Im\{a_3a_4^*\}$	0	1/12√5	0	0	0
$Im\{a_3a_5^*\}$	0	-1/4√5/14	0	0	0
$Im\{a_3a_7^*\}$	3/20√3	0	-1/5√1/3	0	0
$Im\{a_3a_8^*\}$	0	0	-1/24	0	-1/6
$Im\{a_4a_5^*\}$	0	1.114	0	-5/7√1/14	0
$Im\{a_4a_6^*\}$	0	-1/21√5	0	-1/28√5	0
$Im\{a_4a_7^*\}$	1/4√3/5	0	1/2√1/15	0	0
$Im\{a_4a_8^*\}$	0	0	5/72√5	0	1/18√5
$Im\{a_5a_6^*\}$	0	1/7√5/14	0	3/28√5/14	0
$Im\{a_5a_7^*\}$	1/2√3/70	0	√1/210	0	0
$Im\{a_5a_8^*\}$	0	0	5/36√5/14	0	1/9√5/1
$Im\{a_6a_7^*\}$	1/70√3	0	1/10√1/3	0	5/14√1/3
$Im\{a_6a_8^*\}$	9/28	0	-1/36	0	-11/252

The √ symbol implies the square root of the quantity to its right.

to be affected primarily by the most dominant amplitudes, in a relatively direct manner. The higher order terms are, in general, composed of a sum of the real parts of the appropriate bilinear combinations, in addition to a sum over the squares of amplitudes. As such, they depend on the relative phases of the respective amplitudes. Although the complete description is complex, the following points emerge:

1) The existence of a non-zero a_2^{oo} coefficient implies a significant contribution from amplitudes a_2 or higher.

2) The existence of a non-zero a_4^{oo} coefficient implies a significant contribution from amplitudes a_5 or higher.

3) The existence of a non-zero a_6^{oo} coefficient implies a significant contribution from amplitudes a_8 or higher.

The highest order differential cross-section term (a_i^{oo}) observed experimentally, then, gives insight into the number of partial wave amplitudes (and their designations) which contribute significantly.

Similarly, the relationship between the expansion coefficients of the analyzing power (the b_i^{no}) and the sum of appropriate bilinear combinations of partial wave amplitudes (table (2.3)) indicate additional important properties of the reaction. In general, the b_i^{no} coefficients do not depend on squares of amplitudes, but depend instead, on the sum of the imaginary parts of the appropriate bilinear amplitude combinations. Therefore, the b_i^{no} coefficients are potentially very sensitive to relative phases of the amplitudes, and, as a consequence, are more sensitive to the variations of smaller amplitudes. In addition, many of the terms involve the product of a small amplitude with a dominant one (such as a_2), thus leading to enhanced effects from these small amplitudes -- in some respects, an "interference" between the small and large amplitudes.

Inspection of the b_i^{no} coefficients (table (2.3)), for example, indicates the general feature that the b_1^{no} and b_3^{no} coefficients depend significantly on the bilinear terms containing the a_2 amplitude, whereas the b_2^{no}, b_4^{no}, and b_5^{no} coefficients are, indeed, independent of this amplitude. Thus, one may expect the b_1^{no} and b_3^{no} coefficients to dominate as a result of the major role of the $^1D_2$ partial wave channel (corresponding to the a_2 amplitude) in the $\Delta(3,3)$ resonance region. Additionally, a non-zero b_5^{no} coefficient implies significant contributions from partial wave amplitudes of designation a_7 or higher.

2.5 DISCUSSION OF THEORY

To date, development of our theoretical understanding of the $pp \rightarrow \pi^+ d$ reaction has, roughly, kept pace along with the availability of experimental observations. A review of theoretical developments given by M. Betz, B. Blankleider, J.A. Niskanen and A.W. Thomas[19] serves as the basis of the following discussion.

Early attempts to generate a field theoretic model of the $pp \rightarrow \pi^+ d$ reaction provided some, if limited, insight.

Because of the large momentum transfer involved in this reaction, Geffen[20], initiated by Chew[21], suggested that the nature of the nucleon-nucleon short range interactions, and the deuteron D state were important factors in the description of the system. Rescattering of the pion was incorporated within the context of field theoretic models by Litchtenberg[22] shortly after observation of the $\Delta(3,3)$ resonance. Such models, however, are essentially non-relativistic and are usually limited to, at most, one rescattering of the pion (as a result of the first order perturbation techniques usually employed to evaluate them). Furthermore, they suffer from the ambiguities associated with double counting of the pion rescatterings when attempts to include initial and final state interactions are employed.

The most successful model, at least in terms of its quantitative, predictive power, is the coupled-channel model of Green and Niskanen[23,24,25]. It is based on a set of coupled differential equations which incorporate the NN and NΔ channels on an equal footing. The potentials involved in this non-relativistic model are of course, static and provide a framework for the inclusion of heavier meson exchange (exchange of the ρ meson for example). Although the three-body unitarity of the system is only approximately guaranteed, effectively, the summation over the pion multiple scattering series is complete. A reasonable fit to the data however, does involve suitable choices of appropriate parameters.

Recently, there has been considerable interest in the development of 'Unitary Models'[18 26 27], models which are based on the simultaneous consideration of all of the NN, NΔ and πd channels in terms of a set of coupled three-body differential equations. This approach ensures exact two-body and three-body unitarity for all channels, and permits the inclusion of relativistic kinematics. However, such equations are often evaluated using a Tamm-Dankoff approximation[18] where intermediate states with at most one pion are kept, thereby reducing the precision attainable by the technique. These models provide limited opportunity to fine tune their predictions for a given channel, as changes to the other two channels may be effected as a consequence. Despite the unified models' generally poor quantitative agreement with experimental data, these models do provide a framework for a more complete understanding of the few-body system.

3. EXPERIMENTAL APPARATUS AND METHOD.

3.1 INTRODUCTION

The experiment was designed so that the differential cross-section of the $pp \rightarrow \pi^+ d$ reaction could be measured accurately, to within a few percent, utilizing incident proton beams of an arbitrary, but known polarization. Either an unpolarized beam was used and the unpolarized differential cross-section measured, or polarized proton beams were used so both the analyzing power and the unpolarized differential cross-section could be deduced. In the latter case, the differential cross-section was extracted from two sets of differential cross-section measurements taken with oppositely oriented proton beam polarization directions. In principle, use of a polarized beam was adequate for all measurements desired. Nonetheless a more accurate determination of the unpolarized differential cross-section could be made with unpolarized beam, since its polarization is known to be zero exactly.

To achieve a high level of confidence in the results, many of the measurements were repeated a number of times using two or more independent methods. The deduction of the differential cross-section required measurements of the number of $pp \rightarrow \pi^+ d$ events observed, the efficiency with which they were detected, and a knowledge of the effective solid angle of the system. In addition, the overall normalization of the results required, measurement of the incident beam properties (beam energy, current, and polarization) and the effective number of target nuclei within the interaction volume. To facilitate the calculation of the effective solid angle, a detector system with a well defined, relatively simple geometric configuration was used for the detection of each of the particles in the final state of the reaction.

The data collected in this experiment contain redundant measurements of several quantities, which when analyzed provide checks of the system based on internal consistency. These factors contributed to the overall reliability of the final differential cross-section and analyzing power results.

3.2 CYCLOTRON

The TRIUMF cyclotron[28] accelerates both polarized and unpolarized H^- ions to a maximum energy of 520 MeV. The beam current is continuously variable up to a maximum value which depends on both the type of ion source, and on the internal radius, or energy, of the circulating beam. At the maximum orbital radius a 520 MeV beam could be obtained at a maximum current of about 140 μA with the unpolarized ion source, or about 500 nA with the polarized ion source. The beam can be independently extracted into one or more of the external beam lines by stripping electrons from the H^- ions with a thin metal foil. The energy of the external beam is continuously variable from 200 MeV to 520 MeV, depending on the radial position of this stripper foil.

During normal operation the cyclotron produces beam with a 100% macroscopic duty factor. The microstructure consists of proton pulses of roughly 5 nsec duration (also referred to as "beam buckets"), occurring every 43 nsec. The separation of the pulses corresponds to the period characterizing the applied radio frequency power (RF) which is the fifth harmonic of the cyclotron resonance frequency.

3.3 BEAM LINE AND TARGET LOCATION

The experiment was performed at target location 4BT1 on beam line 4B, represented schematically in figure (3.1). The beam was extracted from the cyclotron and transported through the 4B beam optic system defined by a series of dipole and quadrupole magnetic elements. At each beam energy the beam line was tuned by adjusting the strengths of the appropriate steering and focusing magnets in order to produce small beam spots (4 to 6 mm diameter) at both the 4BT1 and the 4BT2 target locations. This process was facilitated using monitors for indicating the position and profile of the beam at various points along the beam line. Additionally, the beam could be centered and its width verified at the target location by remotely viewing a scintillating target with a video monitor.

Figure (3.1)

TRIUMF Facility

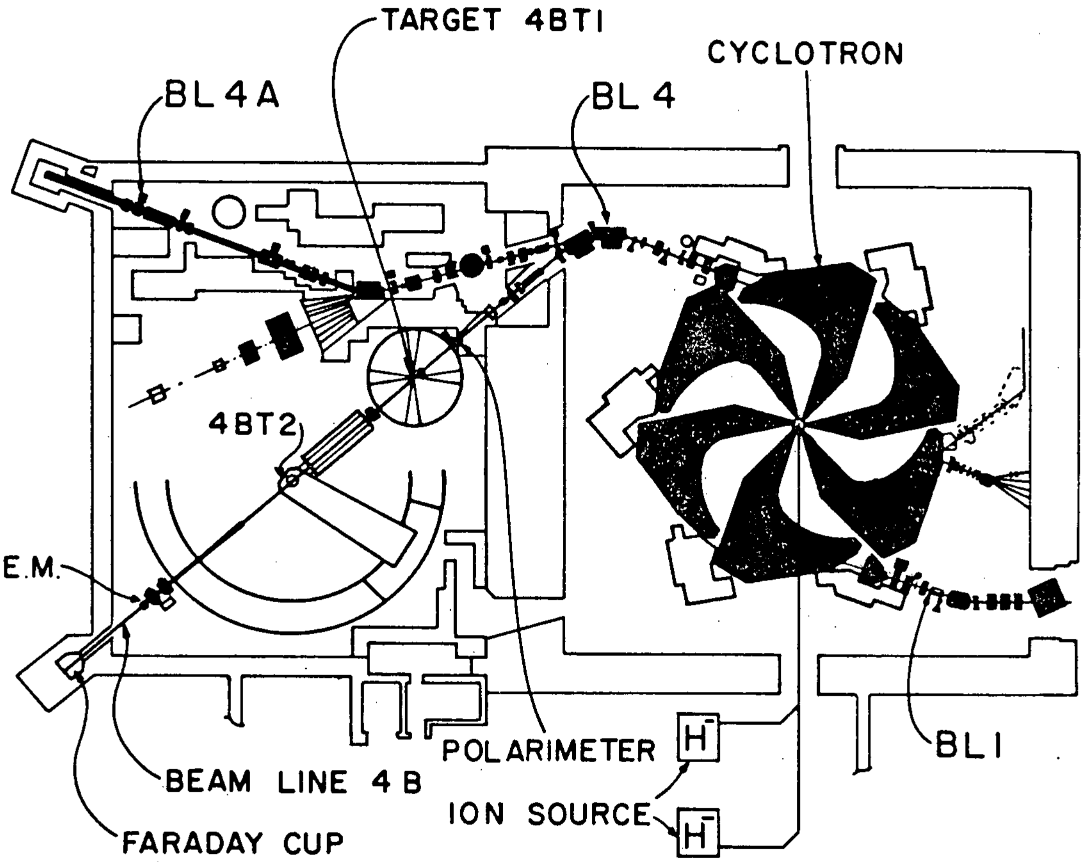

The TRIUMF Cyclotron and the proton experimental area. This exeriment was performed at target location 4BT1 on the primary proton beam-line 4B.

3.4 BEAM POLARIZATION AND CURRENT MONITOR

The four independent beam current monitors are shown schematically in figure (3.2). A polarimeter[29] based on pp-elastic scattering, located 2.7 m upstream of the target, was used to measure both the beam polarization and current. A pp-elastic monitor[10](see appendix (1) for a detailed discussion of the calibration of this, and other beam current monitors) consisting of the four scintillation counters denoted PL1, PL2, PR1, and PR2, measured the current using the technique of counting pairs of protons elastically scattered at 90° C.M. scattering angle. This choice of the scattering angle, due to symmetry, renders the monitor insensitive to the polarization of the beam. The rear detectors, at a radial distance of 71.9 cm from the target, defined the solid angle of this system. The beam's current was then measured two more times as it passed through a secondary emission monitor 21m downstream and was then eventually stopped in a Faraday cup current monitor situated at the end of the beam line.

3.5 APPARATUS

The apparatus was designed with due regard for the kinematic properties of the reaction, the interaction of the particles with the material along the trajectories, and the properties of pion decay into a muon plus anti-neutrino pair. The apparatus was of the two-arm type, consisting of counters for measuring the energy-loss, time-of-flight, and spatial

Figure (3.2)

Beam Line Monitors

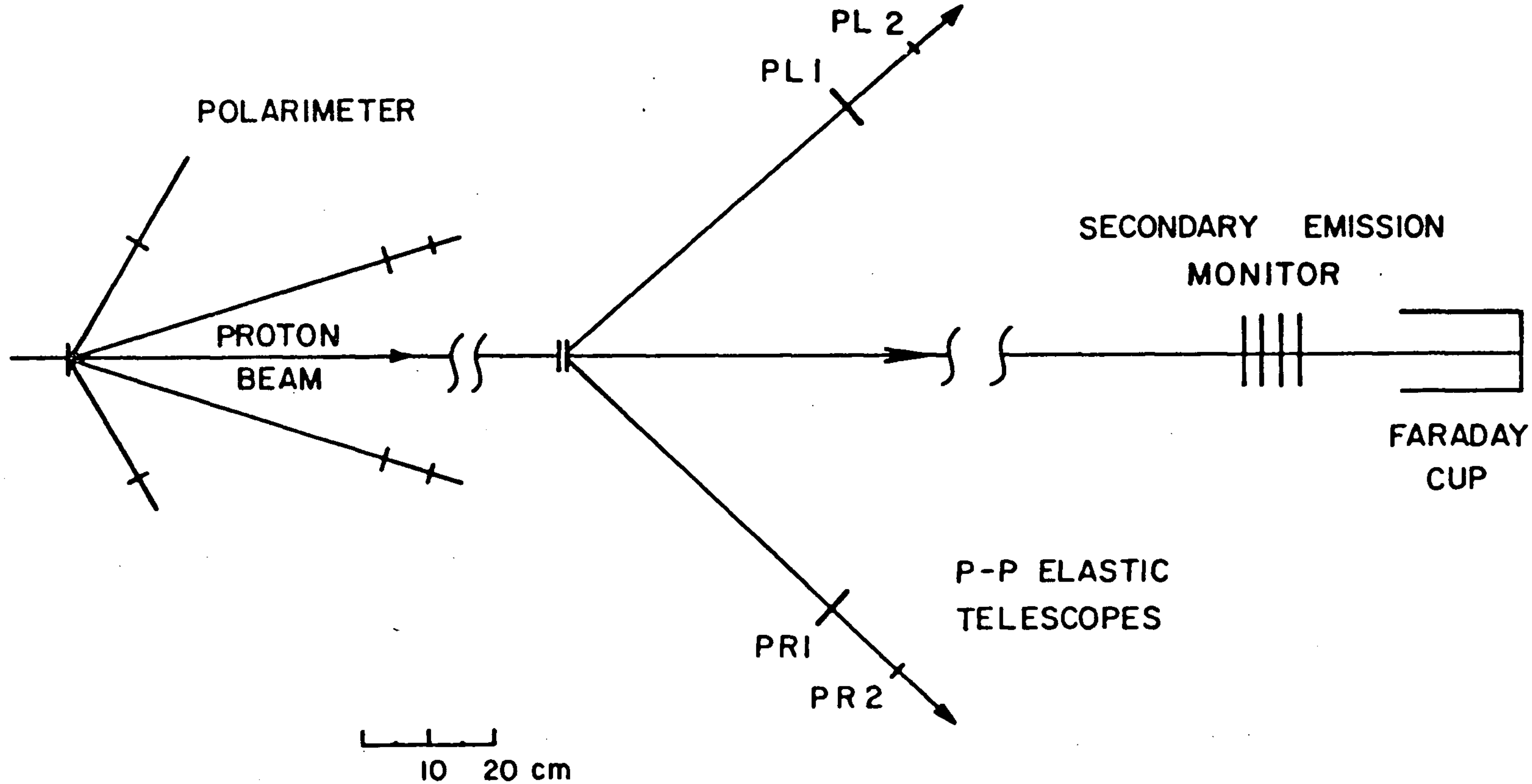

coordinates of both the charged particles in the final state. In fact, with the addition of a second pion arm it was possible to operate two such systems in parallel, since for a given deuteron angle, as defined by the deuteron detection arm position, the associated pion was emitted into one of two kinematically possible angles. The apparatus, which can be divided into several components, is schematically depicted in figure (3.3). The pp-elastic monitor was attached to a rectangular scattering chamber, as were the target holder assembly and the deuteron horn. Both the scattering chamber and its extension, the deuteron horn, were evacuated and contained windows appropriate for either the transmission of particles or the visual inspection of the interior region. Three particle detection systems, two for pions and one for deuterons, were fixed to arms which could rotate independently around the target axis.

3.6 SCATTERING CHAMBER

In addition to providing an evacuated volume in which the reactions occurred, the scattering chamber formed the structural frame work of the whole apparatus. It was constructed of 1/2 inch stainless steel having the outside dimensions of: 91.4cm long, 61.6cm wide and 45.7cm in depth. A target holding assembly was positioned as shown in figure (3.3)

The 0.010 inch mylar windows mounted on their window frames were attached to the chamber on either side of the

Figure (3.3)

Apparatus

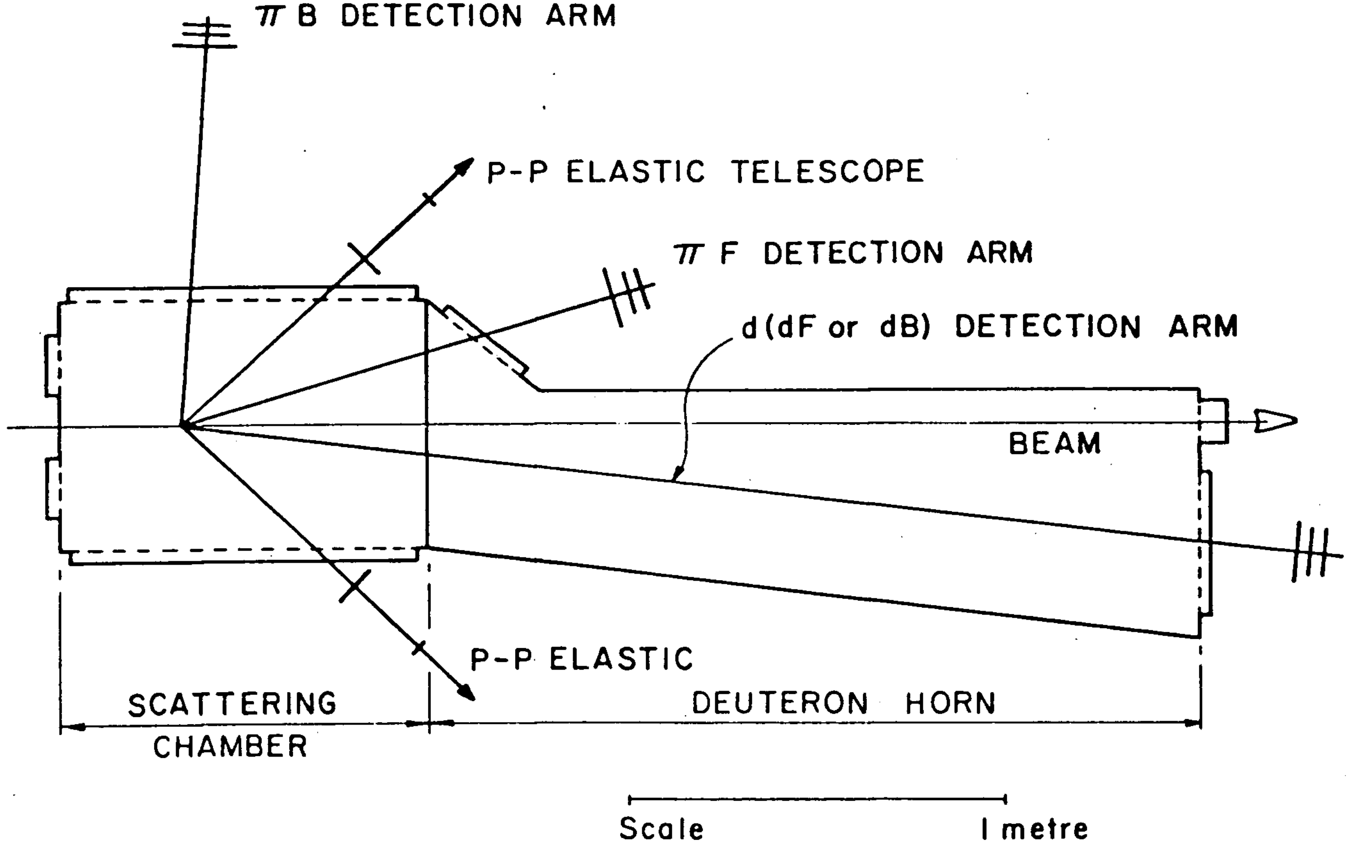

beamline to allow transmission of the pions and elastically scattered protons into the respective detection systems. Two (1/4 inch) lucite windows attached to the upstream end of the scattering chamber permitted visual inspection of the interior region of the chamber, particularly useful when examining the target holding assembly.

3.7 DEUTERON HORN

The deuteron horn was a downstream extension of the scattering chamber required for detecting the coincident deuterons by external counter systems at the small angles required. The geometry of the horn was dictated by the $pp \rightarrow \pi^+ d$ reaction kinematics. In particular, over the center-of-mass pion angles and energies explored in this experiment, deuterons with angles from 4° (relative to the beam direction), up to the maximum Jacobian angle of about 12°, had to be transmitted through the horn to the external detectors. The length of the horn depended on the minimum deuteron detection angle required. The minimum possible detection angle resulted when the detection system was in contact with the beam pipe. Given the 2 inch radius of the beam pipe, simple geometry dictated a 2.0 m deuteron arm length in order to achieve a minimum angle of less than 4°.

3.8 TARGETS AND BEAM ALIGNMENT

The targets were mounted on a target ladder which was in turn attached to, and controlled by, an electro-mechanical target holding device. The ladder contained four 1.5 inch square target positions, typically occupied by the following assortments of targets: a thin CH_2 (typically 45.3 mg/cm^2) target, a thick CH_2 (154.5 mg/cm^2) target, a carbon target(24.9 mg/cm^2), and a zinc sulfide scintillator. The remotely controlled target ladder could be positioned so that any of its four targets were located at the focal point of 4BT1. The focal point at 4BT1 was known relative to grid marked on the zinc sulfide scintillator, which could be viewed (through a lucite window) by a T.V. monitor. The resulting video image was of great help in tuning the 4B beam line and cyclotron.

3.9 PARTICLE DETECTION SYSTEM

Each particle detection system, schematically represented in figure (3.4), consisted of a multi-wire proportional chamber (MWPC) followed by a scintillator telescope. One such system was attached to each of the three movable arms, as depicted in figure (3.3). The forward pion arm was designated the πF arm, and the backward pion arm the πB arm. Similarly the deuteron arm was designated as either the dF or dB arm, depending which pion arm it was associated with, or simply as the d arm when such an association was irrelevant.

Figure (3.4)

Particle Detection System

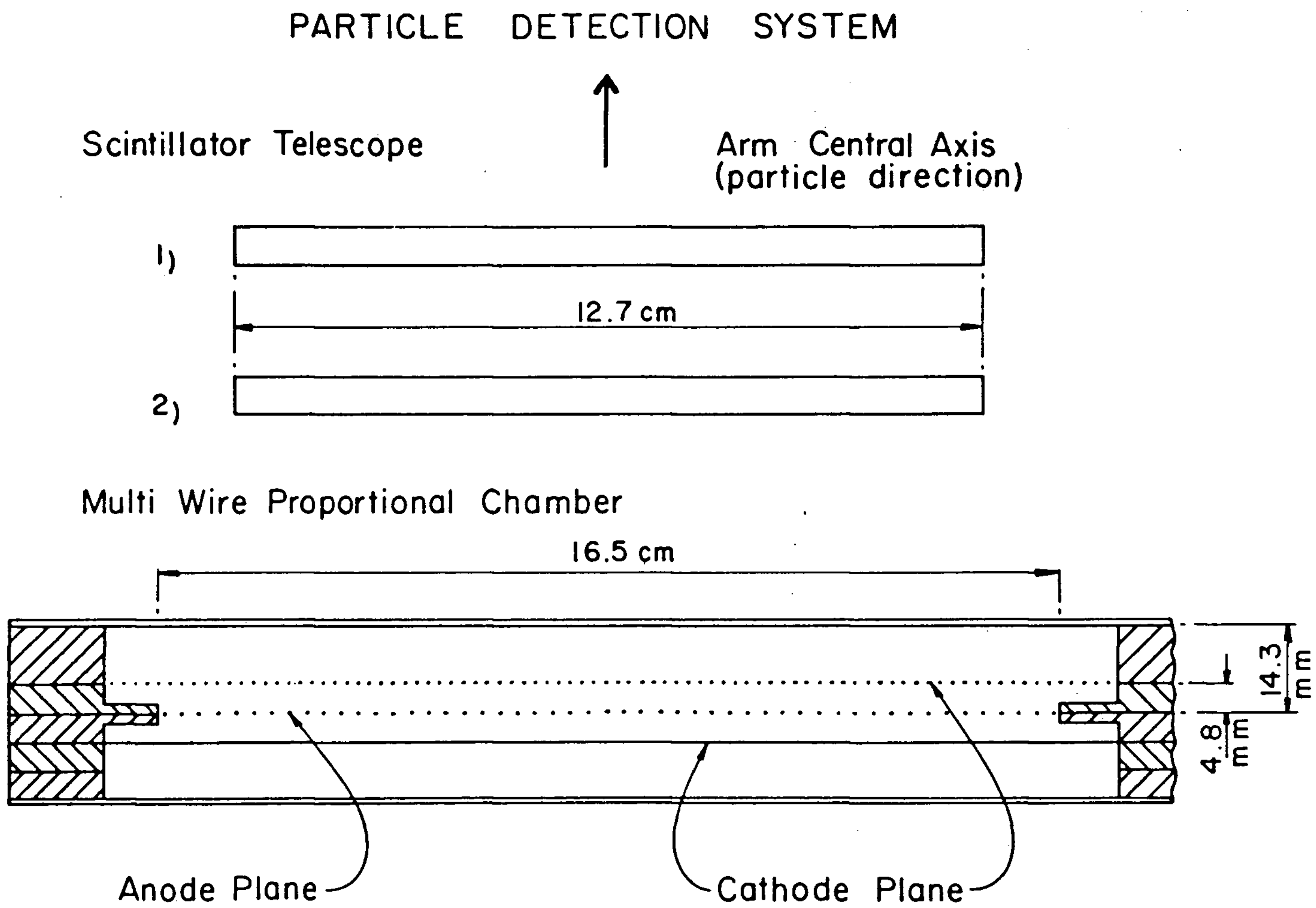

With the MWPC's employed, spatial coordinates of a particle trajectory could be determined with a resolution of better than 1.0 mm. The MWPC, which had an active area of 15.2 x 15.2 cm^2 consisted of three parallel wire planes, a delay-line read-out system, gas containment windows, and provisions for gas circulation. The chambers were operated with a positive high voltage applied to the central anode plane, which was separated from the adjacent cathode planes by 0.48 cm (3/16 inches). The anode plane consisted of 75 (0.20 cm, or 0.008 inch diameter) gold-plated tungsten wires having a separation of 2.0 mm. The two cathode planes each consisted of 150 active sense wires (of 0.006 cm, or 0.0025 inch diameter) separated by 1.0 mm. One end of each cathode plane was electrically connected to a distributed delay-line, with the individual cathode wires connected uniformly along the delay-line.

Spatial information is deduced from the difference in the times it takes signals to traverse the delay-line from the position of the activated sense wire, to both ends of the delay-line, as measured with TDC units. The spatial calibration of this difference of times is treated in section (4.5). During proper operation of the chambers the sum of the two propagation times is constant to within approximately 50 ns. This width of acceptable sum times results primarily from the variation in the distances travelled by electrons and positive ions in the magic gas mixture, from the point of their formation to the point of their detection by a sense wire. A sum time outside of this time interval could indicate the detection of a separated pair of particles or inefficient operation of the chamber.

The wire plane assembly was immersed in a constant flow of 'magic gas'[30] composed of 70% Argon, 29.7% Butane, and 0.3% Freon, at a pressure only slightly exceeding atmospheric.

Two thin plastic scintillators with a 12.7 x 12.7 cm^2 (5 x 5 $inch^2$) active area formed the subsequent telescope. Table (3.1) indicates the radial distances of these detectors from the target, the offsets of the scintillators from the central trajectories, and the thicknesses of the scintillating material (see also table (4.4)). The scintillation light was transmitted through lucite light guides onto RCA 8575 photomultiplier tubes.

3.10 ELECTRONIC LOGIC AND SYSTEMS

The electronic logic and signal processing system, in association with the on-line data analysis system, was responsible for the logical definition of a potential $pp\rightarrow\pi^+d$ event, and it's subsequent processing prior to recording on magnetic tape. Furthermore, it permitted periodic monitoring of all the beam current and polarization monitors, as well as the important characteristics of the events themselves.

The electronic logic used to define a potential $pp\rightarrow\pi^+d$ event (the trigger system) is represented schematically in

Table (3.1)

The Detector Geometry.

Description	Detection Arm		
Detector	d (dF and dB)	πF	πB
Designation			
MWPC	(d) dF dB	πF	πB
Scintillator#1	(d1) dF1 dB1	$\pi F1$	$\pi B1$
Scintillator#2	(d2) dF2 dB2	$\pi F2$	$\pi B2$
Radii			
MWPC	257.7cm	131.2cm	99.0cm
Scintillator#1	261.5cm	138.4cm	107.4cm
Scintillator#2	262.7cm	139.6cm	108.6cm
Thickness			
MWPC			
Scintillator#1	6.35cm	3.18cm	1.59cm
Scintillator#2	6.35cm	6.25cm	6.35cm

Detector Geometry Table Definitions

Designation: The symbolic name associated with the various detectors. As the forward and backward branch deuteron detectors are the same physical system, the F and B distinction is omitted in the appropriate cases. Radii The distances from the target to the front surface of the detectors. Thicknesses The width of the scintillator material.

figure (3.5). The six linear scintillator signals transmitted to the counting room by coaxial cable, were directed to discriminators modules which generated logic pulses (fired) for input signals whose amplitude exceeded a preset threshold level. The linear signals were also (after suitable delay) analyzed by analogue-to-digital converters (ADC) in a CAMAC system which also contained time-to-digital converters (TDC) for measuring relative timing of the associated logic signals. The outputs from the four discriminators which define the forward, and the four which define the backward branch of the system, were brought to a three out of four 'majority' coincidence in the respective branch coincidence unit. If any three out of the four associated scintillators fired, these coincidence units produced a logic signal, thus defining a potential $pp \rightarrow \pi^+ d$ event. A trigger signal was then formed (by the subsequent "OR" logic module) and processed by a logic system that interrupted the data acquisition computer, thus activating a "circuit busy" condition, which inhibited processing of subsequent trigger signals, until the computer had finished accessing all data for the event under consideration. In addition, the 'circuit busy' condition disabled all monitor scalers. The event coincidence signal as well as interrupting the computer was used to start all of the TDC units.

Figure (3.5)

Electronic Trigger Logic and Schematic Diagram

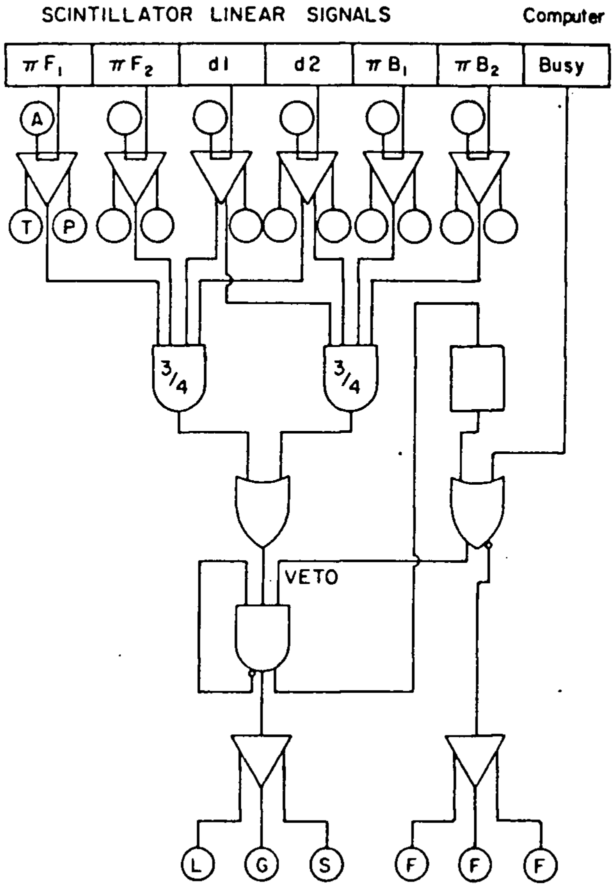

LEGEND OF ELECTRONIC MODULES

COINCIDENCE UNIT
(3/4 DESIGNATES MAJORITY LOGIC
LRS 365) OR LRS 465

OR UNIT
LRS 622

GATE GENERATOR
LRS 222

DISCRIMINATOR
LRS 621 OR 821

CAMAC MODULE FUNCTIONS

(L) CAMAC LAM GENERATOR AND PATTERN UNIT STROBE. EEG C212

(P) PATTERN UNIT BIT REGISTER. EEG C212

(G) ADC GATE. LRS 2249

(A) ADC ANALOGUE.

(S) TDC START. LRS 2228

(T) TDC STOP.

(F) LIVE GATE. (TO CAMAC SCALERS)

3.11 TRIGGER CIRCUIT TIMING

Appropriate delays were provided to the scintillator linear signals so that the relative timing of the pion and deuteron signals at their respective discriminators was that shown in figure (3.6). The d2 scintillator timing was advanced by 2ns relative to that of d1, such that the d1 signal was last to enter the coincidence, so defining the overall timing when both detectors recorded the same particle. In figure (3.6), linear signals from the pion scintillator are shown, indicating the relative timing between the pions and the uncorrelated (random) protons when considered with respect to the deuteron signals. The relative timing of the associated logic signals prior to entering the respective branch coincidence unit (figure (3.5)) are also indicated in figure (3.6). The logic signals from the pion scintillators were advanced by 20ns, such that the timing of the event trigger was also defined by the d1 scintillator for both $pp \rightarrow \pi^+ d$ events and in-phase random events. As a result of the 80ns width of the pion scintillator logic signals, trigger signals were also generated by detection of early (one beam bucket) random events. These occur with the same probability as those generated by the detection of in-phase random events. Thus direct estimation of the background levels associated with in-phase random events was readily obtained. The trigger signal was used to start all of the CAMAC TDC clocks. The deuteron and pion scintillator logic signals were then delayed appropriately and used to stop the

Figure (3.6)

Relative Timing of Linear and Logic Signals

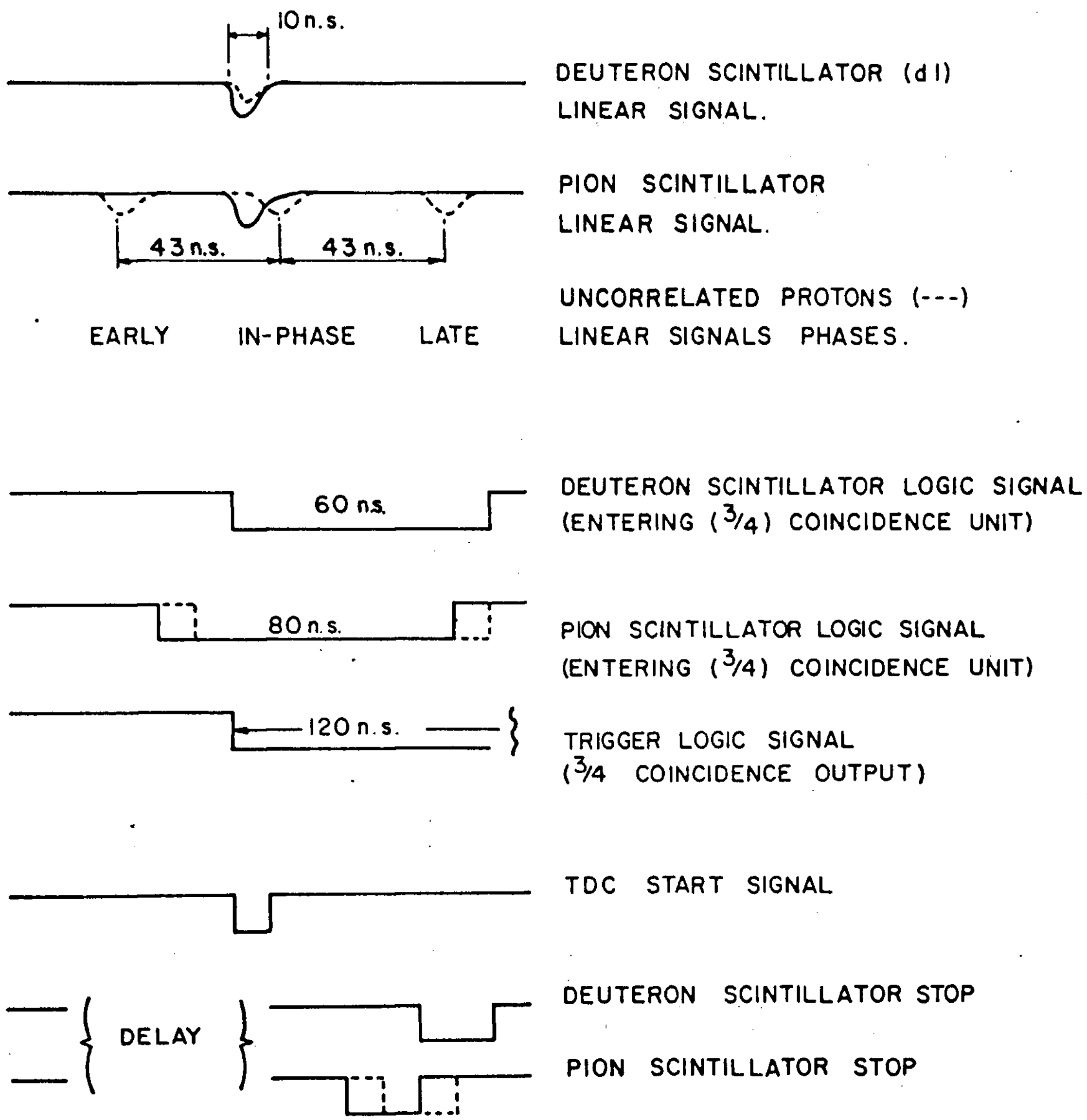

TDC Units associated with them. The MWPC logic signals (four for each of the three chambers) were also delayed appropriately and used to stop the appropriate TDC units. Additionally, the trigger signal was used to generate an ADC "gate", that is, it defined the interval of time over which the CAMAC ADC units integrated the linear signals at its inputs. The quantities scaled by the CAMAC scalers are listed in table (3.2). When the experiment was performed with unpolarized beam, the scalers were permitted to accumulate for the whole duration of a run. When a polarized beam was used, the scalers were read and cleared on a periodic basis, and integrated over each of the beam polarization states by the (auxiliary) data acquisition software.

3.12 DATA ACQUISITION SOFTWARE

The data acquisition system employed for this experiment was a version of the TRIUMF data acquisition system MULTI[31], running on a PDP 11/34 computer under the RSX-11M operating system. As the highest system priority, data were read from the CAMAC modules on an event-by-event basis and stored directly on magnetic tape. On being interrupted by an event, a "computer busy" signal was issued and the data acquisition electronics inhibited until the data handling task was completed. In addition, the MULTI system directed simple on-line calculations and histograming of a subset of the data.

Table (3.2)

Quantities Processed by CAMAC Scalars.

Quantities Accumulated with "Live Gated" Scalers.

Quantity
Number of events
Time intervals
Radio frequency cycles
PP-Elastic monitor events
Faraday Cup monitor events
Polarimeter events

Quantities Accumulated with "Free Running" Scalers.

Quantity
Time intervals
PP-Elastic monitor events
Polarimeter events

Scaler accumulations subject to the "Live Gate" condition are corrected for the system busy time (see figure (3.5)). All of the above quantities were scaled separately for each of the three beam polarization states when a polarized beam was used.

Two additional programs were developed to enhance the on-line calculational power, and to maintain a running sum of scaler quantities that were set to zero each time they were read.

4. ANALYSIS OF THE DATA.

4.1 INTRODUCTION.

The $pp \rightarrow \pi^+ d$ event definition together with more general properties of the data are discussed in the context of a precision data analysis system with the capability of processing a large volume of data. A detailed discussion is presented of the background contribution from carbon nuclei (a component of the production target) and of the effects of pion-decay and energy-loss (and of the detector calibrations) on the acceptance solid angle. The unpolarized and polarized differential cross-sections and analyzing powers, and their associated uncertainties are presented. Finally, angular distributions of the unpolarized and polarized differential cross-sections angular distributions are expanded in terms of Legendre or Associated Legendre polynomials and the corresponding a_i^{oo} and b_i^{no} coefficients deduced.

4.2 EXPERIMENTAL EVALUATION OF THE DIFFERENTIAL CROSS-SECTION

The dependence of the differential cross-section of the $pp \rightarrow \pi^+ d$ reaction on experimentally measured quantities is developed through a series of steps. In the ideal case where the only reaction occurring was that of the $pp \rightarrow \pi^+ d$, the number of observed events $N_{pp \rightarrow \pi^+ d}$, would be given by;

$$N_{pp\rightarrow\pi^+d} = N_{int}\ \epsilon\ d\sigma/d\Omega\ \Delta\Omega^{\dagger} \tag{01}$$

where:

- $d\sigma/d\Omega$ - The $pp\rightarrow\pi^+d$ reaction differential cross-section.
- N_{int} - The number of potential interactions { N(beam) N(target) }.
- ϵ - The combined detector efficiencies.
- $\Delta\Omega^{\dagger}$ - The effective acceptance solid angle.

However, events arising from processes other that of the $pp\rightarrow\pi^+d$ reaction were also observed. As some of these could not be distinguished from the $pp\rightarrow\pi^+d$ events of interest during the event-by-event analysis of the data, the magnitude of their contribution to the total number of observed events has to be determined indirectly. The number of primary events which satisfied the $pp\rightarrow\pi^+d$ event definition included a small number of background events as well as random coincidences, in addition to the $pp\rightarrow\pi^+d$ events of interest. That is,

$$N_p = N_{pp\to\pi^+d} + N_c + N_r \tag{02}$$

where:

N_p	- The total number of events that satisfied the $pp\to\pi^+d$ event definition
$N_{pp\to\pi^+d}$	- The number of true $pp\to\pi^+d$ events contained in the primary event sample.
N_c	- The number of carbon bacground events contained in the primary event sample.
N_r	- The number of uncorrelated events (randoms) contained in the primary event sample.

It will be shown that the number of random events can be extracted from analysis of the data, and that the carbon background can be described by an effective differential cross-section $d\sigma_c/d\Omega$. Thus, the number of observed events is given by the relationship;

$$N_p = N_{int}\ \epsilon\ \{\ d\sigma/d\Omega + \tfrac{1}{2}d\sigma_c/d\Omega\ \}\ \Delta\Omega^{\dagger} + N_r \tag{03}$$

Here N_{int} is the product of the number of incident protons and the number of hydrogen atoms in the target (occurring as CH_2 molecules). Thus, $d\sigma/d\Omega$ is obtained by solving the above expression:

$$d\sigma/d\Omega = \{ (N_p - N_r) / (N_{int} \epsilon \Delta\Omega^{\dagger}) \} - \tfrac{1}{2}d\sigma_c/d\Omega \tag{04}$$

Each component of this function will be discussed.

4.3 EVENT-BY-EVENT DATA ANALYSIS

The on-line data acquisition system accepted all events which satisfied the two-arm coincidence criterion (backgrounds as well as the $pp \rightarrow \pi^+ d$ events of interest) and recorded these on magnetic tape. In addition to the problem of handling the background information, one had to contend as well with the fact that some of the $pp \rightarrow \pi^+ d$ events of interest were lost due to detector inefficiencies. Therefore, the off-line data acquisition system had both to identify the $pp \rightarrow \pi^+ d$ events within a data set and correct the number observed for the inefficiency of the detection system.

4.3.1 TREATMENT OF THE RAW DATA

There were two types of events that were written onto magnetic tape on an event-by-event basis. The events were numbered sequentially, and the number was attached to each event. The two types of events, designated type A and type B, were written in units referred to as blocks. Each block consisted of approximately fifteen type A events followed by one type B event.

Type A events represent the information required to define each event (ADC, TDC, and MWPC data). Type B events represent quantities integrated over the type A events comprising the block, such as polarimeter counts and time intervals. Due to software errors, the (MULTI[31]) data acquisition program failed to operate as specified, resulting in data being written in an unpredictable order at times.

It is, however, possible to compensate for this abnormality. The identification of an abnormality and the corrective action taken is based on the observed sequence of event numbers. In all, there are three types of errors that can be identified.

1) Duplicated data blocks
2) Missing data blocks
3) Missing type B events

The duplicated data blocks are identified by the observed duplication of a series of event numbers. The corrective action in this case is rejection of the duplicated events.

Similarly, a missing data buffer is identified by a series of missing event numbers (associated with the anticipated series of type A and type B events). In addition, the block of missing events has to occur between the last type B event of the previous block, and the first type A event of the subsequent data block. No corrective action is required (other than to renumber the subsequent events).

A more serious condition occurred when a type B event is (apparently) arbitrarily omitted. If this condition is not rectified, the beam current (and other quantities summed by the CAMAC scalers) is disproportionately low. The condition is, however, clearly identified when one event number (and only one) is missing in a data block, where a type B event is expected. The corrective action requires three steps.

1) All of the events between two complete data blocks are ignored

2) All subsequent scalar numbers are reduced by the amount integrated over the ignored data blocks

3) The subsequent events are renumbered

The software errors responsible for these conditions were located and were verified to be the cause of the observed problems.

4.3.2 THE PRIMARY EVENTS

Primary events were a subset of all recorded events satisfying the $pp \to \pi^+ d$ event definition. Included in this subset, however, were events associated with the carbon impurity of the target and events that were recorded as a result of random coincidences (false triggers) between uncorrelated elastically scattered protons. The methods used to estimate the size of this relatively small background (about three per cent) are discussed later in section (4.6). The primary event type was defined by its ability to satisfy a set of cuts appropriately placed on a number of experimental observables. The data were compared on an event-by-event basis with the event definition, and the number of primary events determined. Missing from this subset, however, were those $pp \rightarrow \pi^+ d$ events associated with data that failed to satisfy the event definition due to inefficient detectors.

The event definition was based on three types of quantities:

1) Time-of-flight quantities; associated with measurements of time intervals.

2) Pulse-height quantities; associated with measurements of the pulse-heights of specified electronic detector signals.

3) Kinematic quantities; associated with the kinematic correlation of the two-body final state.

Time-of-flight and pulse-height measurements were both determined from scintillation detector signals and were therefore (weakly) correlated. As the kinematic quantities were calculated from the spatial coordinates of the trajectories as determined by the multi-wire proportional chambers, they were independent of the pulse-height and time-of-flight information.

4.3.2.1 Pulse-Height Distributions

Charged particles lose energy while traversing matter such as scintillators. Some of this energy is converted to light. The light pulses are detected by high gain photomultiplier tubes which produce a current pulse for each light pulse incident. The total charge of each current pulse was converted into digital form by an analogue-to-digital converter (ADC) and recorded. The deuteron, pion, muon and proton pulse-heights were expected to vary linearly with the energy deposited by the particle of interest in the scintillators. Significant deviation from such a relationship was only expected for the low energy pions and muons.

The pulse-height distributions characteristic of the particles passing through the scintillators comprising the pion and deuteron arms (and their correlation) is indicated in figure (4.1). Peaks in the distribution are associated with the $pp \rightarrow \pi^+ d$ reaction, and with (random) background events. Three qualitative features of the pulse-height distribution displayed in figure (4.1) are:

1) The number of $pp \rightarrow \pi^+ d$ events is significantly greater than the number of random background events.

2) The clean separation of the $pp \rightarrow \pi^+ d$ events and the random background distributions.

3) The long tail on the high pulse-height side of the distributions (related to the Landau energy-loss distribution).

Lower limit cuts imposed on both of the allowed pion and deuteron pulse-height values, separate the $pp \rightarrow \pi^+ d$ events from the random background. Because of the Landau shape, upper limit constraints were not be applied since some $pp \rightarrow \pi^+ d$ events would be rejected as a result.

Figure (4.1)

PION AND DEUTERON PULSE-HEIGHT DISTRIBUTIONS

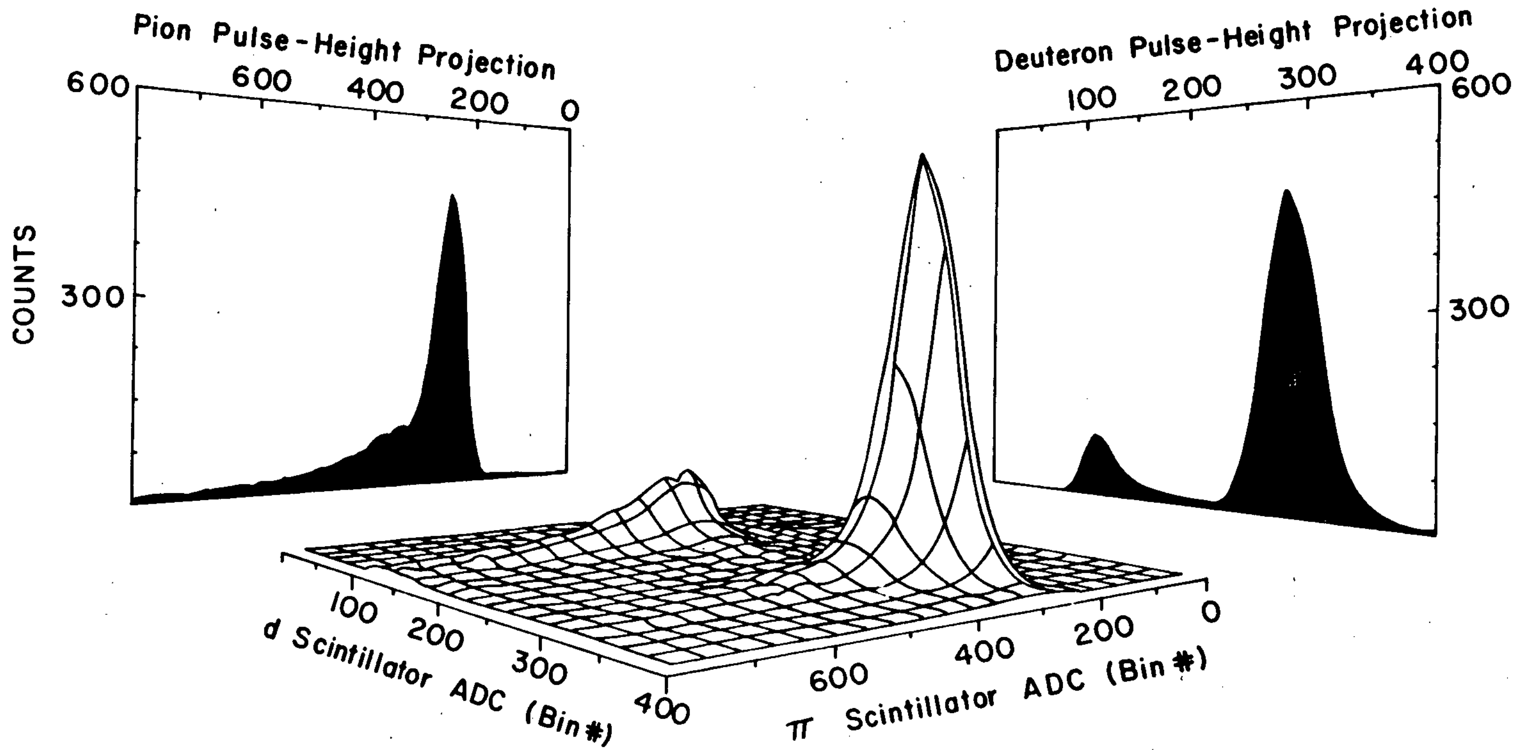

POLYETHYLENE (CH_2) TARGET

Figure (4.2) depicts the pion and deuteron pulse-height distribution obtained when data were collected using a pure carbon target. The prominent $pp \rightarrow \pi^+ d$ peak of the pulse-height distribution collected using the polyethelene target is absent, while the qualitative features of the distribution associated with the uncorrelated proton background are essentially identical. A small number of events (about three percent of the $pp \rightarrow \pi^+ d$ signal, when properly normalized) were distributed over the area of deuteron and pion pulse-heights characterizing the $pp \rightarrow \pi^+ d$ events arising from a CH_2 target. These events are referred to as carbon background events.

The position of the centroids of the pulse height distributions for the $pp \rightarrow \pi^+ d$ reaction were a function of the incident proton beam energy. As a result, the 'cut' values of $pp \rightarrow \pi^+ d$ pion and deuteron detector pulse-heights varied on a run to run basis. The energy-loss dE/dx of the particles has an inverse dependency on their energies[oo]. Thus, the pion and deuteron scintillator pulse-heights are expected to vary as the inverse square of the particle's velocity.

The central positions of the pion and deuteron pulse-height distributions were measured and fit to linear functions of the inverse square of the corresponding velocity, as determined kinematically. The central position of the pion and deuteron distributions along with the prediction of the resulting fits are indicated in

Figure (4.2)

PION AND DEUTERON PULSE-HEIGHT DISTRIBUTIONS

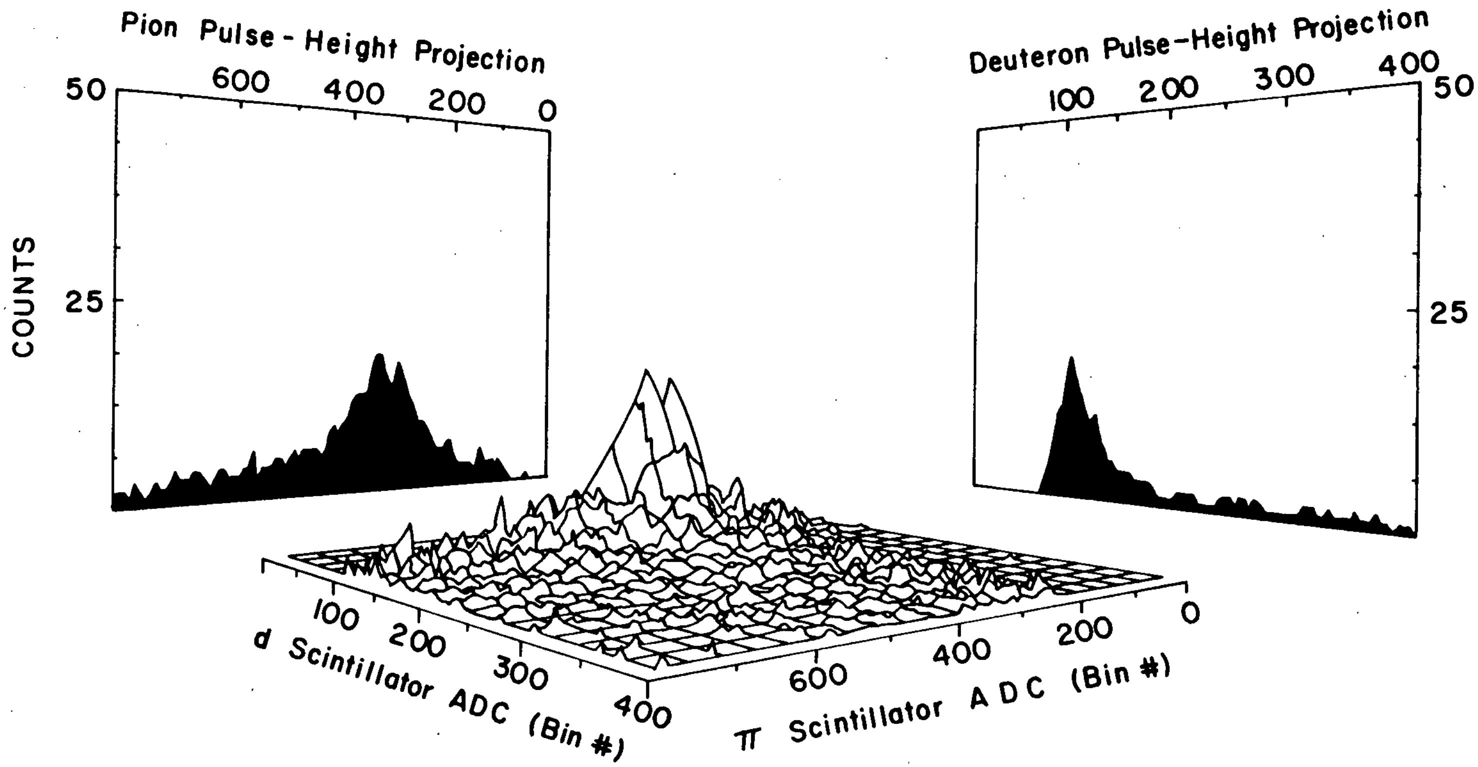

CARBON TARGET

figure (4.3) and figure (4.4). The values of the lower limit that defined the allowed values of the pion and deuteron pulse-heights are related to the central values of the respective distributions by a constant difference and are indicated in the figures.

4.3.2.2 Time-of-Flight Distributions

Time intervals between the trigger signal timed to the deuteron arm scintillators and the detection of a particle by the pion arm scintillators were recorded by a CAMAC TDC in digital form. The recorded values of the time intervals are linearly related to their actual value through the TDC module calibrations.

A two-dimensional plot of a typical pion TDC spectrum vs. the deuteron dE/dx is depicted in figure (4.5). The prominent peak of the distribution, associated with the $pp \rightarrow \pi^+ d$ reaction, is clearly separated from those peaks identified with background. The single background peak evident in the pulse-height distribution (figure (4.1)) is now split into several peaks centered at different pion time-of-flight values.

Selection of events associated with the $pp \rightarrow \pi^+ d$ reaction could be obtained by testing their pion time-of-flight values and determining whether they were contained within an appropriate range of allowed values.

The series of background peaks arise from the detection of uncorrelated protons associated with different RF beam 'buckets' (R.F. cycles). Figure (4.6) depicts the

Figure (4.3)

Deuteron Scintillator Pulse-Height Distribution Peaks and Cuts.

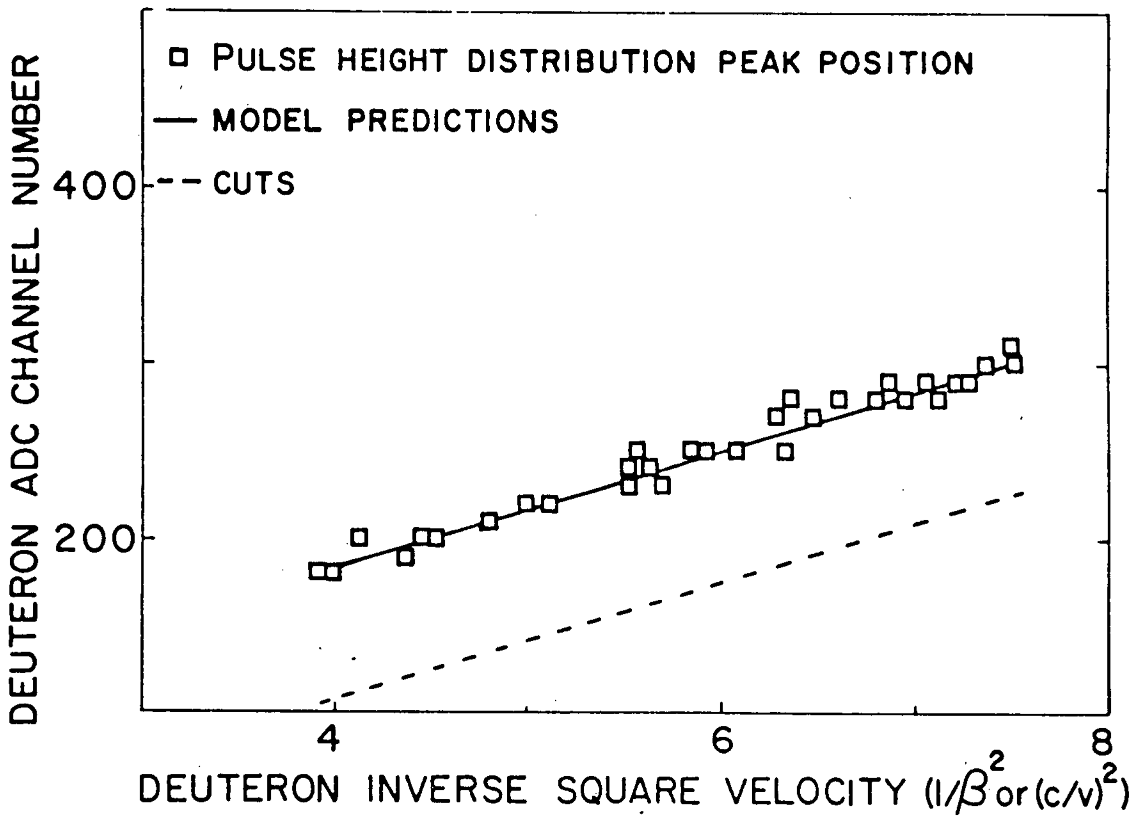

Experimentally determined pulse-height distribution peaks (most probable values) are plot against the inverse square deuteron velocity. No upper limit cuts are applied to pulse-height values.

Figure (4.4)

Pion Scintillator Pulse-Height Distribution Peaks and Cuts.

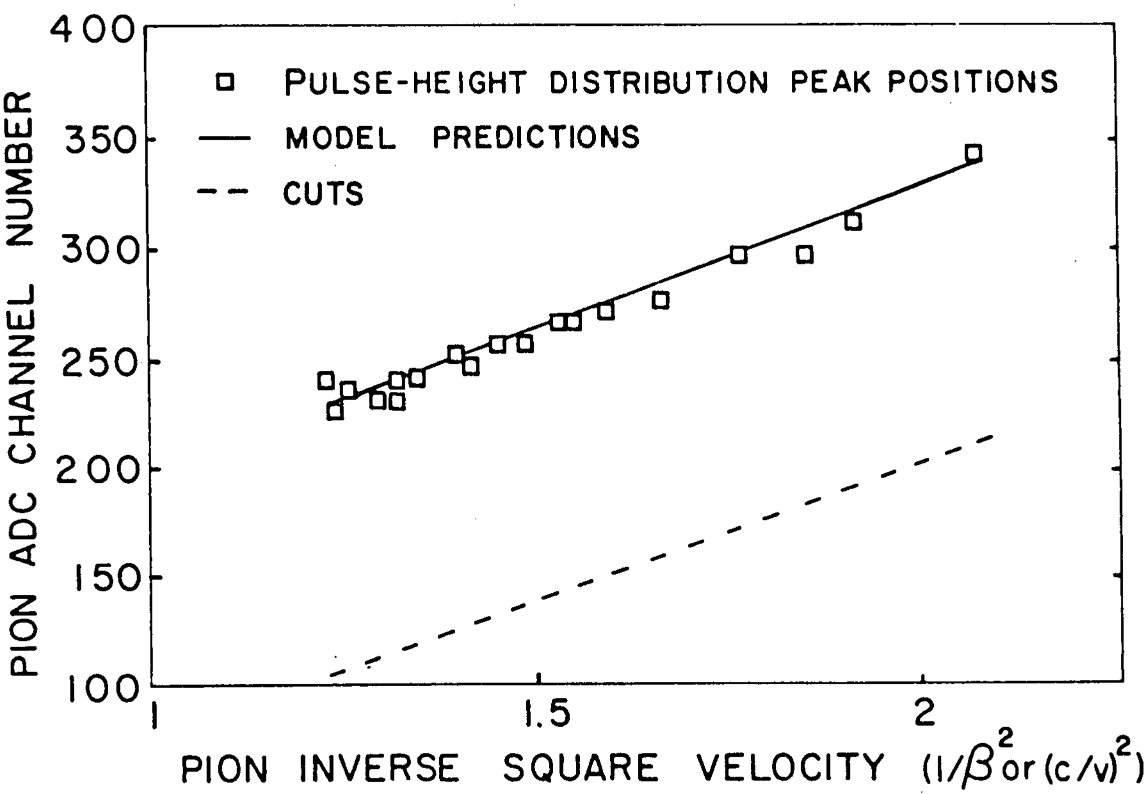

Experimentally determined pulse-height distribution peaks (most probable values) are plot against the inverse square pion velocity. No upper limit cuts are applied to pulse-height values.

Figure (4.5)

TIME-OF-FLIGHT AND DEUTERON PULSE-HEIGHT DISTRIBUTIONS

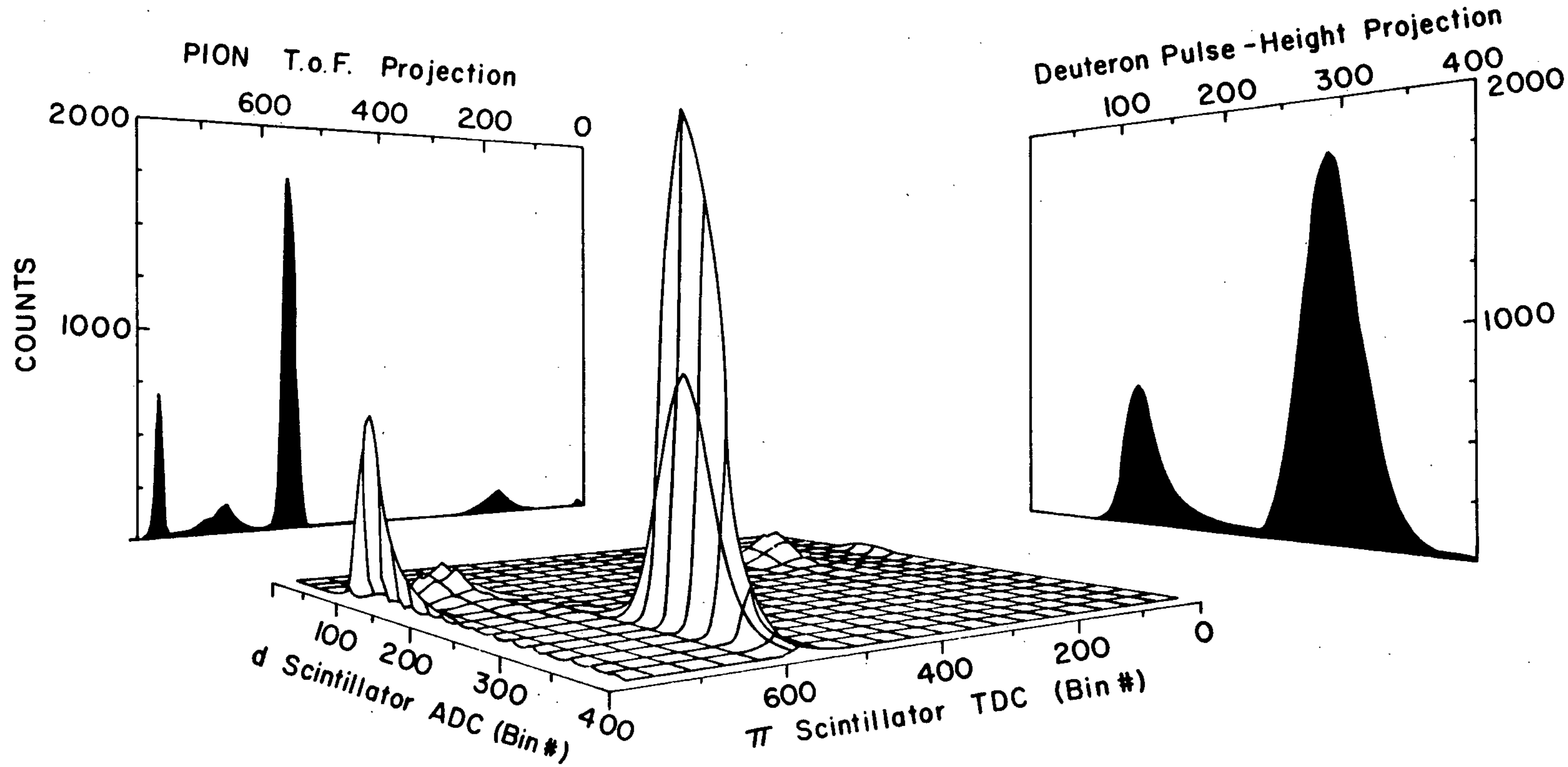

POLYETHYLENE (CH_2) TARGET

Figure (4.6)

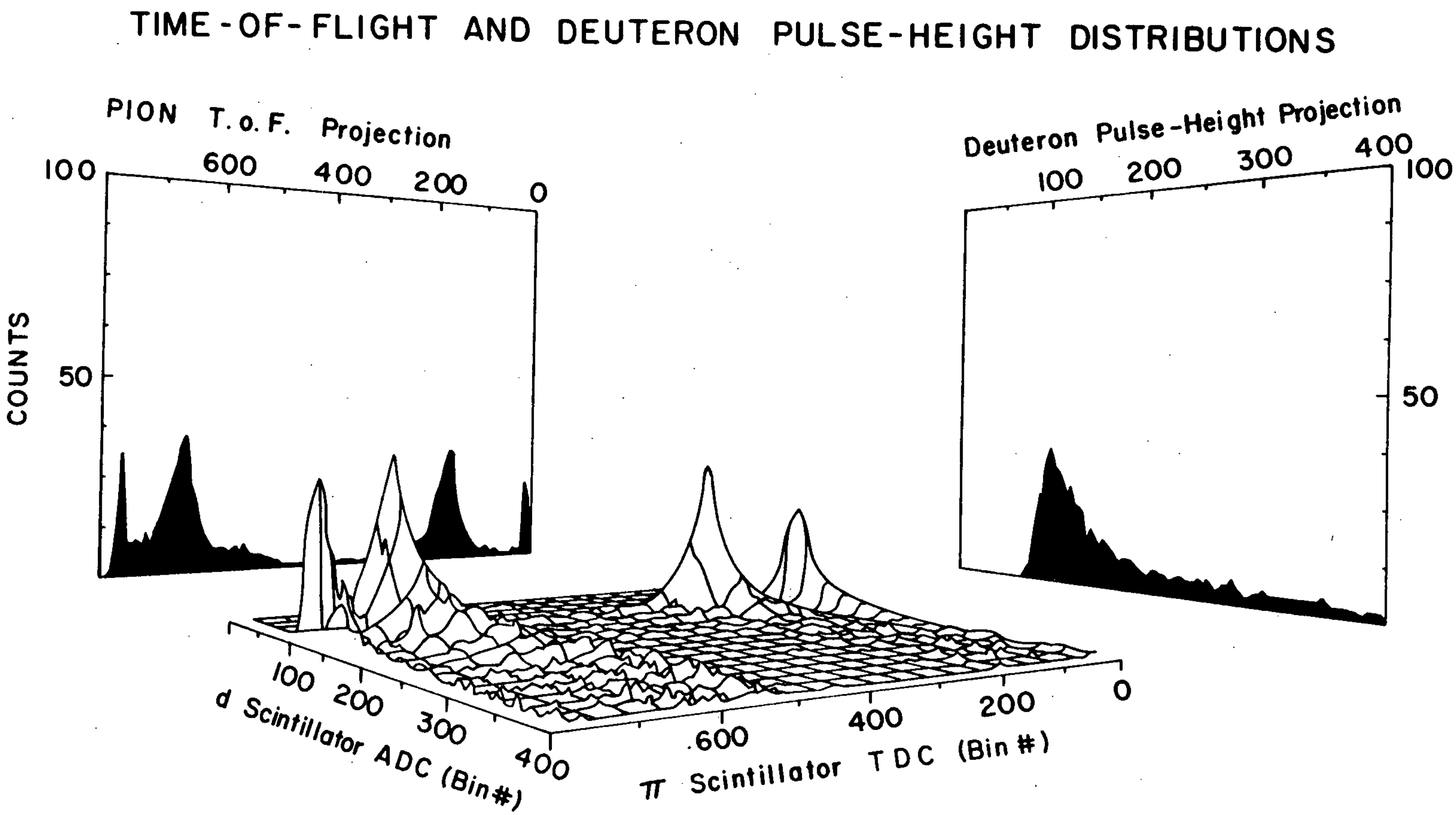

CARBON TARGET

corresponding two dimensional plot for a carbon target. As expected, the prominent peak corresponding to $pp \to \pi^+ d$ events is absent, while peaks representing the background are qualitatively unchanged (the number of counts in both plots are not normalized to each other). Nonetheless, there were a small number of carbon background events located in the region where $pp \to \pi^+ d$ events would be expected when a polyethelene target was used.

The position of the $pp \to \pi^+ d$ time-of-flight peak varied as a function of the beam energy and pion angle (as did the values of the associated upper and lower limits used to define the allowed time-of-flight values of a $pp \to \pi^+ d$ event). Again, cut levels are defined by linear alogarithms.

Centroids of the time-of-flight distributions were measured for a fraction of the runs and were fit to the corresponding calculated values, assuming a linear relationship. The results of such a fit are shown in figure (4.7). Also indicated are the values of the upper and lower limits which differ from the value of the respective centroid by a constant value.

4.3.2.3 Kinematic Distributions

Since the coordinates of both final state particles were measured, it was possible to check on an event-by-event basis whether the angular coordinates of the two particles were correlated as the reaction kinematics predicted. This was possible not only for the $pp \to \pi^+ d$ events but also the $pp \to pp$ events, where they were detected. The angular

Figure (4.7)

Time-of-Flight Distribution Peaks and Cuts.

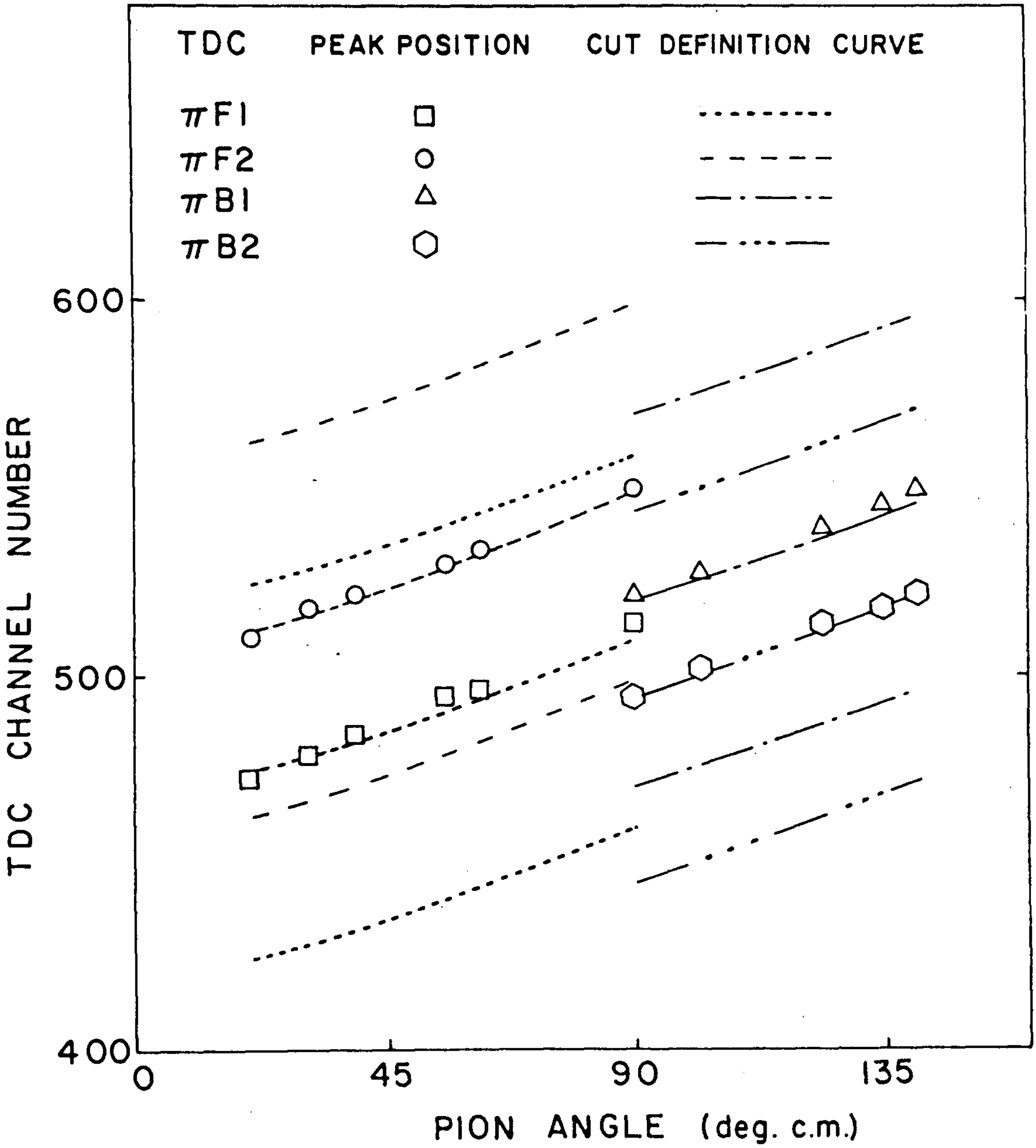

Experimentally determined distribution peaks are plot against the pion angle. The set of curves at the lower pion angles are associated with the forward arm scintillators (πF1 and πF2) and the others with the backward pion detection arm scintillators (πB1 and πB2).

correlation is defined as the correlation of the polar coordinates (θ) and the angular coplanarity is defined as the correlation of the azimuthal (ϕ) coordinates.

As a notational aid to specify in which detection arm, an otherwise indistinguishable proton is detected, the following notation is introduced;

p_1 - Implies proton detection by the pion detector.

p_2 - Implies proton detection by the deuteron detector.

The angular correlation is defined by;

$$\Delta\theta_{\pi d} = \Theta_{\pi d}(\theta_{\pi}) - \theta_{d} \tag{05}$$

$$\Delta\theta_{pp} = \Theta_{pp}(\theta_{p_2}) - \theta_{p_1}$$

where:

$\Delta\theta_{\pi d}$ - The angular correlation of the $pp \rightarrow \pi^+ d$ reaction products.

$\Delta\theta_{pp}$ - The angular correlation of the $pp \rightarrow pp$ reaction products.

$\Theta_{\pi d}(\theta_{\pi})$ - The deuteron angle determined kinematicalally from the (measured) pion angle and incident proton energy.

$\Theta_{pp}(\theta_{p_2})$ - The proton angle (pion detector side) determined kinematicalally from the (measured) θ_{p_2} proton angle and incident beam energy.

θ_{p_1} - The (proton) polar angle measured with detectors mounted on the pion arm.

θ_{p_2} - The (proton) polar angle measured with detectors mounted on the deuteron arm.

The angular coplanarity is defined by;

$$\Delta\phi_{\pi d} = (\phi_{\pi} - \pi) - \phi_{d} \qquad (06)$$

$$\Delta\phi_{pp} = (\phi_{p_2} - \pi) - \phi_{p_1}$$

where:

$\Delta\phi_{\pi d}$ - The angular coplanarity of the $pp \rightarrow \pi^+ d$ reaction products.

$\Delta\phi_{pp}$ - The angular coplanarity of the $pp \rightarrow pp$ reaction products.

ϕ_{p_1} - The (proton) azimuthal angle measured from detectors mounted on thepion arm.

ϕ_{p_2} - The (proton) azimuthal angle measured from detectors mounted on the deuteron arm.

Clearly, the angular correlations so defined are zero if the particles are perfectly correlated. In general, the angular distribution associated with each reaction is represented by a sharp peak about a central value. An example of a typical angular correlation distribution is shown in figure (4.8) .

Figure (4.8)

A Typical Angular Correlation Distribution.

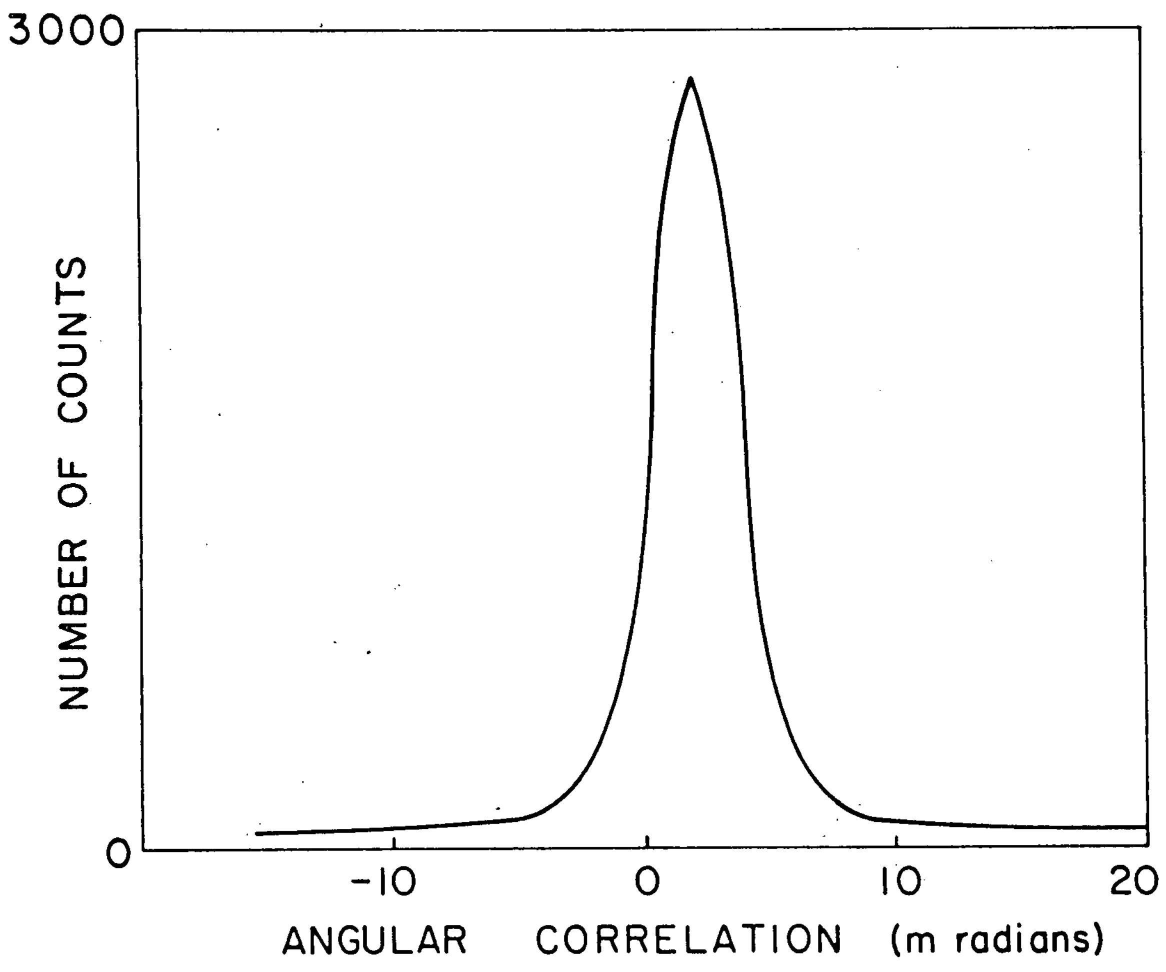

The events associated with the extreme edges of the distribution result from the detection of random (uncorrelated) proton events and of deuteron-muon pairs.

4.3.3 THE UNCORRELATED EVENTS: RANDOMS.

It was evident (see figure (4.5) for example), that the time-of-flight values associated with random events could, in a small number of cases, fall within the range of allowed values associated with the $pp \rightarrow \pi^+ d$ reaction. Such events would satisfy the primary event definition and thus would be counted in the number of primary events.

The number of such random events contained in the sample could, however, be estimated from the time-of-flight distribution of random events associated with particles separated by one R.F. cycle from the events of interest. Since the two complete random distributions accepted by the on-line data acquisition system (separated by an interval of time associated with one R.F. cycle (43 nsec.)) were of similar shape, such a subtraction technique was permissible.

The number of random events, then, were approximated (to within counting statistics) as the number of such events that satisfied the $pp \rightarrow \pi^+ d$ event definition with a modified time-of-flight criteria. The time-of-flight values were required to fall within the range allowed for values associated with the $pp \rightarrow \pi^+ d$ reaction but shifted by an amount corresponding to one R.F. period. In general, the number of such random events represented an insignificant fraction (typically much less than one percent) of the number of primary events.

4.3.4 SCINTILLATOR EFFICIENCIES

It was possible to determine the efficiency of each scintillator during the event-by-event analysis of the raw data, because of the redundancy of the number of scintillators designed into the experimental system (see figure (3.3)). 'Trial' events, that is events which by reason of the kinematics and particle type should have caused a particular scintillator to fire, were identified. Trial events were accepted if a number of criteria were satisfied:

1) The $pp \rightarrow \pi^+ d$ angular correlation and coplanarity conditions were satisfied.

2) The other three scintillators fired (the event definition coincidence a involved 3/4 majority coincidence) with appropriate $pp \rightarrow \pi^+ d$ pulse-height values.

3) Appropriate time-of-flight values were obtained, and corresponded with those of the $pp \rightarrow \pi^+ d$ reaction. That is, the time-of-flight conditions were omitted for those scintillators whose efficiency was being determined.

A successful event was defined as a trial event in which the pulse-height for the detector being tested fell within the limits associated with the $pp \rightarrow \pi^+ d$ event definition.

Assuming binomial statistics, the efficiency of a scintillator, ϵ, and its uncertainty $\Delta\epsilon$ are given by:

$$\epsilon = n / N$$

$$\Delta\epsilon = \epsilon \sqrt{(1-\epsilon)/n} \tag{07}$$

where:

N - The number of trial events.

n - The number of successful events.

The efficiencies of the scintillators were examined for all of the runs and were observed to deviate from unity by only an insignificant amount (typically 0.1%) in the majority of cases. Somewhat larger deviations occurred when the average pion momentum was less than 100 MeV/C, In such cases, the second pion scintillator appeared to have a lower efficiency (as low as 98%). This, however, did not reflect a real inefficiency of the scintillator, but rather a breakdown of the method used to define the efficiency, in particular, the definition of the trial events. In such cases, a low momentum pion that satisfied the trial event definition, could stop in the material between the first and second scintillators, and therefore appear (artificially) as a scintillator inefficiency.

For the rest of the analysis such small inefficiencies of the scintillators were neglected. The apparent inefficiency of the pion arm (second scintillator) was then taken into account in the defintion of the solid angle acceptance of the detection system.

4.3.5 MULTI-WIRE PROPORTIONAL-CHAMBER EFFICIENCIES

The efficiency of each MWPC was determined by a method similar to that employed to determine the efficiency of the scintillators. First, trial events, were identified, namely those events associated with a particle that was inferred to have passed through a multi-wire proportional chamber. Then, the multi-wire chamber was tested to determine if it had detected the particle (a successful event). The definition of these trial events was:

1) All four scintillators detected particles with pulse-heights and time-of-flight values consistent with those of the $pp \rightarrow \pi^+ d$ event definition (the scintillators were smaller than the active surface of the MWPC).

2) The sum time (discussed in section(3.9)) associated with the conjugate wire chamber was within acceptable limits. This condition ensured that only single particles traversed the conjugate counter.

3) The position of the particle was within five centimeters of the center of the conjugate wire chamber.

Such a trial event was deemed successful if it satisfied the additional condition that both the X and Y delay-line sum times (That is, the sum of the total delay-line propagation times, discussed in section (3.9)) of the multi-wire proportional-chamber under consideration were within acceptable limits. Those few trial events associated with double tracks in the chamber under consideration were thus rejected since the delay-line read-out system only provides accurate position information for single tracks. The efficiency ϵ, and its error $\Delta\epsilon$, of the multi-wire proportional chamber were also described by equation (07).

4.3.6 BEAM POLARIZATION

The magnitude of the beam polarization normal to the reaction plane was monitored with the polarimeter[29]. The polarization was determined from the measured asymmetry, ϵ, of the left-right scattering of the incident beam from the polarimeter target:

$$P = \epsilon / A_p \tag{08}$$

Where A_p is the analyzing power of the polyethylene target of the polarimeter, the uncertainty in the polarization P, arises both from standard (Poisson) counting statistics as well as from a systematic uncertainty in the appropriate value of the analyzing power, A_p. Although the left-right asymmetry is dominated by the pp-elastic scattering from the hydrogen component of the target, quasi-free scattering from the protons in carbon also contributed, leading to corrections of 5-10% from the free p-p values. The values used for the analyzing power were obtained from internal TRIUMF communications.

4.3.7 BEAM CURRENT NORMALIZATION

The beam flux is determined from the pp-elastic scattering rate at 90° C.M. resulting from interaction of the incident beam with the protons in the target used for the $pp\rightarrow\pi^{+}d$ reaction production[10]. The number of scattered protons detected by the pp-elastic monitor are related to the pp-elastic differential cross-section $d\sigma_{pp}/d\Omega$ by;

$$d\sigma_{pp}/d\Omega = \tfrac{1}{2}\{ Ns / (N_{int}\ 2\ \Delta\Omega) - d\sigma_{c}/d\Omega \} \qquad (09)$$

These terms are defined in detail in appendix (1). The number of potential interactions N_{int} is identical for the simultaneous $pp\rightarrow\pi^{+}d$ reaction, and is given by;

$$N_{int} = Ns / \{ 2\Delta\Omega\ [\ 2d\sigma_{pp}/d\Omega + d\sigma_{c}/d\Omega\ ]\ \} \qquad (10)$$

where:

Ns	- Twice the number of pp-elastic events.
N_{int}	- The number of potential interactions (N(beam)*N(target))
$\Delta\Omega$	- The pp-elastic monitor acceptance solid angle.

The values of the $pp\rightarrow pp$ elastic cross-sections and solid angles used are listed in appendix (1). The value of N_{int} was subject typically to a 0.5% random error and a 1.8% systematic error.

4.4 SOLID ANGLES

4.4.1 GEOMETRIC SOLID ANGLES

The geometric solid angles as defined here represent both the solid angles subtended by individual detectors, and the joint geometric solid angle subtended by a combination of two detectors. They depend only on the apparatus geometry and the $pp \rightarrow \pi^+ d$ reaction kinematics.
The individual laboratory geometric solid angles of the pion and deuteron detectors, $\Delta\Omega_g$ and $\Delta\Omega_d$, are:

$$\Delta\Omega_g = \int_{\Omega_0} d\Omega \quad \text{and} \quad \Delta\Omega_d = \int_{\Omega_1} d\Omega \tag{11}$$

Where the domains of the integration variables are:

Ω_0 - The set of Laboratory angles $\{\theta,\phi\}$ subtended by the pion detector.

Ω_1 - The set of Laboratory angles $\{\theta,\phi\}$ subtended by the deuteron detector.

In both cases the domain of the integration variable was defined by a small rectangular surface (the detector) of linear dimensions Δx, and Δy, a distance r, from the target.

Consequently these integrals can be approximated by;

$$\Delta\Omega = \Delta\theta\Delta\phi \tag{12}$$

where:

$$\Delta\theta = 2 \tan^{-1}(\Delta x/2r)$$

$$\Delta\phi = 2 \tan^{-1}(\Delta y/2r)$$

4.4.2 TRANSFORMATION OF THE SOLID ANGLE TO THE CENTER-OF-MASS SYSTEM

Transformation of the laboratory solid angles to the center-of-mass (C.M.) system is, of course, dependent on the two-body kinematics of the $pp \rightarrow \pi^{+}d$ reaction. The corresponding center-of-mass solid angles (designated with a * superscript) are then:

$$\Delta\Omega_g^* = \int_{\Omega_0^*} d\Omega^* \quad \text{and} \quad \Delta\Omega_d^* = \int_{\Omega_1^*} d\Omega^* \tag{13}$$

Where the domains of the integration variables are:

Ω_0^* - The set of C.M. angles $\{\theta^*, \phi^*\}$ subtended by the pion detector.

Ω_1^* - The set of C.M. angles $\{\theta^*, \phi^*\}$ subtended by the deuteron detector.

Calculation of these quantities is simplified by the following three steps:

First, the center-of-mass solid angles were obtained by integrating over the laboratory coordinates, utilizing the solid angle transformations (Jacobians) $j_\pi(\theta_\pi)$ and $j_d(\theta_d)$. Where the pion solid angle transformation, $j_\pi(\theta_\pi)$, is;

$$j_\pi(\theta_\pi) = d\Omega^*_\pi/d\Omega_\pi \tag{14}$$

and that of the deuteron $j_d(\theta_d)$, is;

$$j_d(\theta_d) = d\Omega^*_d/d\Omega_d$$

Second, these Jacobians were approximated by their values at the central azimuthal angle and factored from the integral (such a procedure is invalid, however, at or near the peak deuteron angle). Thus:

$$\Delta\Omega^*_g = \int_{\Omega_0} j_\pi(\theta_\pi)d\Omega_\pi = j_\pi(\bar{\theta}_\pi)\int_{\Omega_0} d\Omega_\pi$$

$$= j_\pi(\bar{\theta}_\pi)\ \Delta\Omega_g$$

and (15)

$$\Delta\Omega^*_d = \int_{\Omega_1} j_d(\theta_d)d\Omega_d = j_d(\bar{\theta}_d)\int_{\Omega_1} d\Omega_d$$

$$= j_d(\bar{\theta}_d)\ \Delta\Omega_d$$

Third, as indicated, identification of the resultant integrals with the laboratory geometric solid angles (equation (11)).

The joint solid angle of the system is that defined by the coincident detection of both final-state particles. For the apparatus described, it was defined by the pion detector which subtended a smaller center-of-mass solid angle than the deuteron detector.

4.4.3 THE EFFECTIVE SOLID ANGLE

In addition to the constraints imposed by the geometry of the apparatus, the effective acceptance of the system was dependent on the nature of the physical interactions experienced by the particles as they traversed the apparatus. The effects of pion decay ($\pi^+ \rightarrow \mu^+ \bar{\nu}$), multiple scattering, energy-loss, and ranging-out can be combined with the geometric constraints to define an effective solid angle (C.M.) $\Delta\Omega^\dagger$. This effective solid angle incorporates an event detection efficiency, $\epsilon(r,\Omega^*,\hat{\Omega}^*)$, into the solid angle definition:

$$\Delta\Omega^\dagger = \int_{\Omega_0^*} \int_{\Omega_4^*} \epsilon(r,\Omega^*,\hat{\Omega}^*)\, d\hat{\Omega}^*\, d\Omega^* \tag{16}$$

where:

$\Delta\Omega^\dagger$	- The effective solid angle
$\epsilon(r,\Omega^*,\hat{\Omega}^*)$	- The event detection efficiency
$\hat{\Omega}^*$	- The initial pion direction.
(r,Ω)	- Polar coordinates of the detection point.
Ω_4^*	- The set of all possible pion production angles.

As defined here, the event detection efficiency represents the probability of detecting an event with an initial pion direction specified by the angular coordinates $\hat{\Omega}^*$, at a point specified by its distance r, and angular coordinates Ω^*, with respect to the target and beam direction. In this formalism pions created with trajectories so directed that they would miss the pion detector could, in principle, be detected following a change of direction. If the detection of either a pion or its associated muon decay product together with the correlated deuteron satisfies the event definition, then its detection efficiency can be written in terms of the detection efficiencies of the individual particles:

$$\epsilon(r,\Omega^*,\hat{\Omega}^*) = \epsilon_d(R(\hat{\Omega}^*))\{ \epsilon_\pi(r,\Omega^*,\hat{\Omega}^*) + \epsilon_\mu(r,\Omega^*,\hat{\Omega}^*)\} \tag{17}$$

where:

$R(\hat{\Omega}^*)$	- Represents the initial deuteron direction as a function of the correlated pion direction.
$\epsilon_d(R(\hat{\Omega}^*))$	- The deuteron detection efficiency.
$\epsilon_\pi(r,\Omega^*,\hat{\Omega}^*)$	- The pion detection efficiency.
$\epsilon_\mu(r,\Omega^*,\hat{\Omega}^*)$	- The muon detection efficiency.

If this form of the detection efficiency is substituted into the integrand of equation (16), then the effective solid angle separates into pion and muon components, $\Delta\Omega_{\pi}^{*}$ and $\Delta\Omega_{\mu}^{*}$ respectively:

$$\Delta\Omega^{\dagger} = \Delta\Omega_{\pi}^{*} + \Delta\Omega_{\mu}^{*} \tag{18}$$

where:

$$\Delta\Omega_{\pi}^{*} = \int_{\Omega_0^*} \int_{\Omega_4^*} \epsilon_{\pi}(r,\Omega^*,\hat{\Omega}^*)\ d\hat{\Omega}^*\ d\Omega^*$$

$$\Delta\Omega_{\mu}^{*} = \int_{\Omega_0^*} \int_{\Omega_4^*} \epsilon_{\mu}(r,\Omega^*,\hat{\Omega}^*)\ d\hat{\Omega}^*\ d\Omega^*$$

These two components have different properties, thus are evaluated separately.

4.4.4 THE PION COMPONENT OF THE EFFECTIVE SOLID ANGLE

The relatively simple nature of pion and deuteron propagation through the apparatus results in a significant simplification of the pion term of the effective solid angle (that is, the pion effective solid angle). If the pions and deuterons are each assumed to travel (on average) along straight lines, (as defined by the appropriate kinematic quantities) then three approximations may be employed:

First, the detector arrangement dictates that deuteron is always detected, hence:

$$\epsilon_{d}(R(\hat{\Omega}^*)) = 1 \tag{19}$$

Second, the radial dependence of the pion detection efficiency is expected to be proportional to the fraction,

f_π, of pions surviving decay in flight:

$$f_\pi = f_\pi(r) = \exp(\ m_\pi r/(\ \tau p_\pi)\ ) \tag{20}$$

where p_π is the pion momentum and τ is mean life at rest.

Third, the angle of detection Ω^*, becomes identical to the creation angle $\hat{\Omega}^*$.

Therefore the angular detection probability can be represented by a delta function, and the efficiency becomes;

$$\epsilon_d(R(\hat{\Omega}^*))\ \epsilon_\pi(r,\Omega^*,\hat{\Omega}^*) = f_\pi\ \delta(\ \hat{\Omega}^* - \Omega^*\ ) \tag{21}$$

Substituting this efficiency into the pion effective solid angle integration (equation (18)) yields:

$$\Delta\Omega_\pi^* = \int_{\Omega_0^*} \int_{\Omega_4^*} f_\pi\ \delta(\ \hat{\Omega}^* - \Omega^*\ )\ d\hat{\Omega}^*\ d\Omega^* \tag{22}$$

Integration over the initial pion direction variable $\hat{\Omega}^*$ is trivial, leaving;

$$\Delta\Omega_\pi^* = f_\pi(r) \int_{\Omega_0^*} d\Omega^*$$

The final integration is simply the geometric solid angle (equation (13)), and therefore;

$$\Delta\Omega_\pi^* = f_\pi \Delta\Omega_g^* \tag{23}$$

Furthermore, substituting equation (12) and equation (15) for the geometric solid angle yields;

$$\Delta\Omega_\pi^* = f_\pi\ j_\pi(\bar{\theta}_\pi)\Delta\theta\Delta\phi \tag{24}$$

This representation of the pion component of the effective solid angle was verified (to within a one percent) through Monte Carlo simulations of the experiment (appendix (2)) for runs of average pion momenta greater than 100 MeV/c (greater than approximately 35 MeV.).

4.4.5 THE MUON COMPONENT OF THE EFFECTIVE SOLID ANGLE

Evaluation of the muon component of the effective solid angle (equation (18)) is not as straightforward as it is in the case of the pion component. Primarily, this is a consequence of the generally non-colinear pion-muon trajectories. This point is reflected by non-zero values of the event detection efficiency $\epsilon_\mu(r,\Omega^*,\hat{\Omega}^*)$, in cases where the initial pion direction $\hat{\Omega}^*$, and detection point angular coordinates Ω^*, differ. Consequently, the pion production solid angle, as defined by the pion detector alone, is larger for detection of muons than it is if pions are detected. In addition, the acceptance of the deuteron detector is not large enough to detect all the deuterons associated with parent pion trajectories directed into the increased solid angle; therefore the (joint) muon solid angle was no longer determined by the pion detector acceptance alone. This can be shown by decomposing the solid angle into terms that display the explicit dependence on the deuteron arm geometry.

$$\Delta\Omega^*_\mu = \int_{\Omega^*_0} \int_{\Omega^*_4} \epsilon_\mu(r,\Omega^*,\hat{\Omega}^*)\, d\hat{\Omega}^*\, d\Omega^* \tag{25}$$

$$= \int_{\Omega^*_0} \{ \int_{\Omega^*_2} \epsilon_\mu(r,\Omega^*,\hat{\Omega}^*) d\hat{\Omega}^*$$

$$+ \int_{\Omega^*_3} \epsilon_\mu(r,\Omega^*,\hat{\Omega}^*) d\hat{\Omega}^* \} \, d\Omega^*$$

where the integration variables domains (sets) satisfy:

Ω^*_2 — $\{\hat{\Omega}^*\} : R(\hat{\Omega}^*) \in \{\Omega^*_d\}$

Ω^*_3 — $\{\hat{\Omega}^*\} : R(\hat{\Omega}^*) \notin \{\Omega^*_d\}$

$\Omega^*_4 = \Omega^*_2 \cup \Omega^*_3$

$\{\Omega_d\}$ — The set of angular coordinates subtended by the deuteron detector.

If the deuteron is assumed to travel (on average) in a straight line, then the detector geometry defines the following detection efficiency;

$$\epsilon_d(R(\hat{\Omega}^*)) = \begin{cases} 1; & \text{if } R(\hat{\Omega}^*) \in \{\Omega^*{}_d\} \\ 0; & \text{if } R(\hat{\Omega}^*) \notin \{\Omega^*{}_d\} \end{cases} \tag{26}$$

Clearly, the second term in the muon effective solid angle vanishes, leaving the double integral

$$\Delta\Omega_{\mu}^{*} = \int_{\Omega_0^*} \int_{\Omega_2^*} \epsilon_{\mu}(r,\Omega^{*},\hat{\Omega}^{*}) \; d\hat{\Omega}^{*} \; d\Omega^{*} \tag{27}$$

An integration over both of the pion and deuteron detector angular coordinates results.

4.4.6 SEMI-PHENOMENOLOGICAL MODEL OF THE MUON COMPONENT OF THE EFFECTIVE SOLID ANGLE

Evaluation of the muon component of the effective solid angle $\Delta\Omega_{\mu}^{*}$ was of sufficient complexity that non-analytic methods were employed. Its evaluation, therefore, was carried out in two steps. First, a semi-phenomenological model of the solid angle was developed. Then, determination of the free parameter of the model was carried out using the results of Monte-Carlos simulations of the experiment for a number of selected experimental configurations.

The solid angle subtended by the parent pions (whose daughter muons are detected) is again much larger than that of the associated deuteron $\Delta\Omega_{d}^{*}$, and is (approximatly) bound by a maximum muon solid angle $\Delta\hat{\Omega}_{\mu}^{*}$, defined by the Jacobian peak angle $\hat{\theta}_{\mu}$ characterizing the pion decay. That is;

$$\Delta\hat{\Omega}_{\mu}^{*} = 2\pi\{\ 1 - \cos(\ \hat{\theta}_{\mu}\ )\ \} \tag{28}$$

As a result of the greater size of this maximum muon solid angle relative to that of the associated deuteron $\Delta\Omega_{d}^{*}$, the joint solid angle of the two detection systems is no longer determined by the size of the pion detector alone (as it is for $\Delta\Omega_{\pi}^{*}$).

The initial investigation of the effect of pion decay on the effective solid angle involved comparison of the fraction of the total effective solid angle contributed by the muon ($\Delta\Omega_{\mu}^{*}/\Delta\Omega^{\dagger}$) to the ratio of the "maximum" muon to deuteron solid angles, ($\Delta\hat{\Omega}_{\mu}^{*}/\Delta\Omega_{d}^{*}$). Clearly, this ratio depends on the fraction of muons present, f_{μ}. That is;

$$\Delta\Omega_{\mu}^{*}/\Delta\Omega^{\dagger} = f_{\mu} \{ F(\Delta\hat{\Omega}_{\mu}^{*}/\Delta\Omega_{d}^{*}) \} \tag{29}$$

where:

$$f_{\mu} = f_{\mu}(r) = 1 - f_{\pi}(r)$$

Interestingly, as shown in figure (4.9), the Monte Carlo simulation of the experiment for a select set of configurations indicated a simple exponential relationship for F as a function of the argument displayed in equation (29). By interpolating the results of this figure to other values of the argument, ($\Delta\hat{\Omega}_{\mu}^{*}/\Delta\Omega_{d}^{*}$), the total effective solid angle could be determined using equation (18) rewritten as;

$$\Delta\Omega^{\dagger} = \Delta\Omega_{\pi}^{*}/(1 - \Delta\Omega_{\mu}^{*}/\Delta\Omega^{\dagger}) \tag{30}$$

Again, rewritten as a function of the parameter F, this yields;

$$\Delta\Omega^{\dagger} = \Delta\Omega_{\pi}^{*}/(1 - Ff_{\mu}) \tag{31}$$

Substituting the existing expression for the pion effective

Figure (4.9)

The Effective Muon Solid Angle F Parameters.

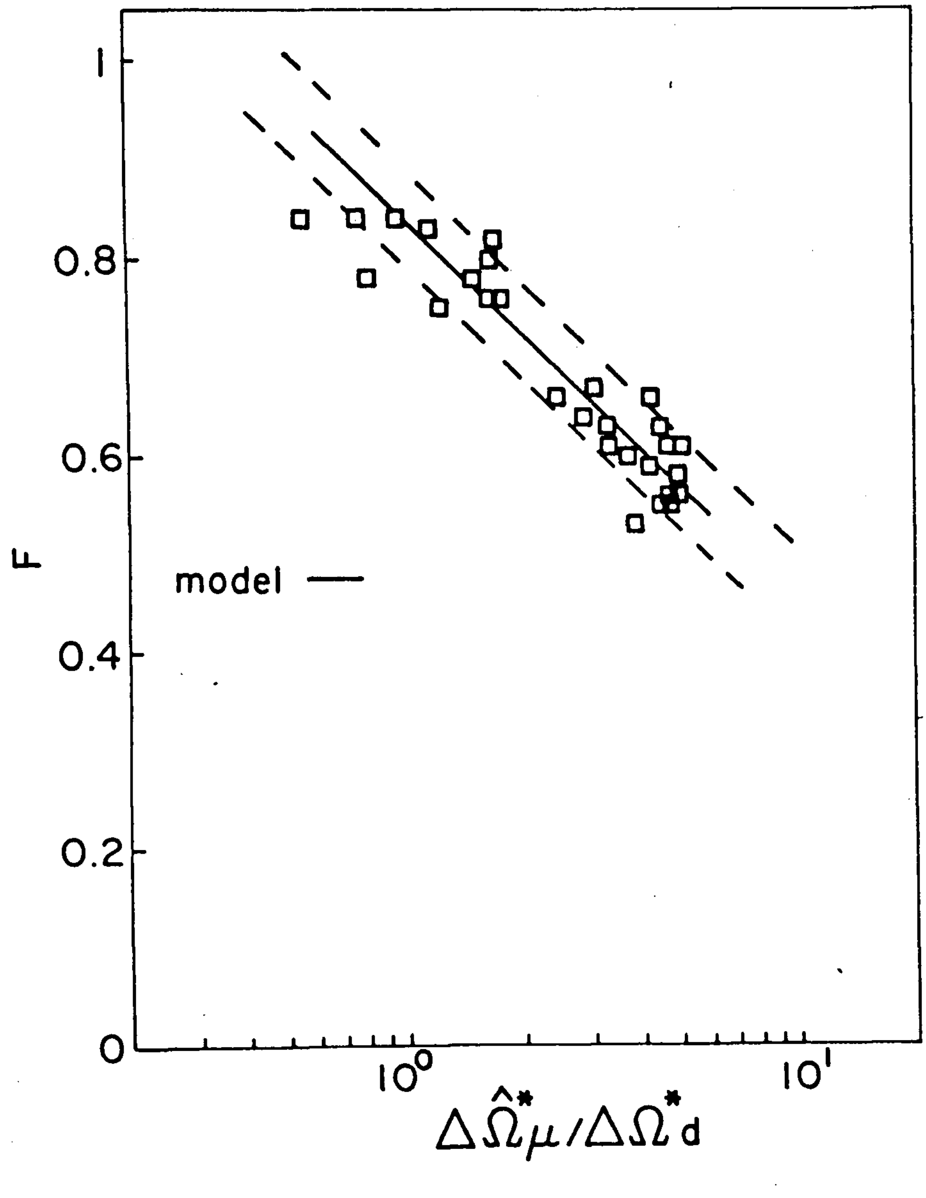

The F parameters determined from Monte Carlo simulations of the experiment for selected configurations. The solid line indicates the predictions of the Semi-phenomenological model of the effective muon solid angle fit to this data.

solid angles (equation (23)) into this equation yields;

$$\Delta\Omega^{\dagger} = \Delta\Omega_{g}^{*} \{ f_{\pi}/(1 - Ff_{\mu}) \} \tag{32}$$

The effective solid angle $\Delta\Omega^{\dagger}$ was determined in this way, to the first order, for all the experimental configurations employed. Final values of $\Delta\Omega^{\dagger}$ for a small number of cases involved additional correction for energy-loss effects as described in section (4.4.8).

4.4.7 COMPARISON OF THE SOLID ANGLE MODELS TO MONTE CARLO EVALUATIONS

Effective and geometric solid angles were evaluated in a Monte Carlo simulation which incorporated pion-decay multiple-scattering and energy-loss for both pions and muons. As the particle energy-loss contribution to the effective solid angles was found to be insignificant in the majority of cases, these energy-loss effects are neglected in the following discussion and treated as a small correction at a later point. Assumptions used to derive the pion effective solid angle expression (equation (24)) were verified, as were a select number of the associated solid angle predictions, to within a one percent (statistical) accuracy. Monte Carlo evaluations of the complete effective solid angle $\Delta\Omega^{\dagger}$, were then combined with values calculated for the geometric cross sections $\Delta\Omega_{g}^{*}$, the pion fractions f_{π}, and the muon fractions f_{μ}, to determine the aforementioned F parameters according to the formula;

$$F = \{ 1 - f_{\pi} (\Delta\Omega_g^* / \Delta\Omega^\dagger) \} / f_\mu \tag{33}$$

As depicted in figure (4.9), they were found to exhibit a reasonably linear dependence on the logarithm of the ratio $(\Delta\hat{\Omega}_\mu^* / \Delta\Omega_d^*)$;

$$F = \{ a \log_{10}(\Delta\hat{\Omega}_\mu^* / \Delta\Omega_d^*) + b \} \pm \Delta \tag{34}$$

where;

$$a = -0.39 \qquad b = 0.84 \qquad \Delta = 0.05$$

This, within the indicated uncertainty, provided a reasonable phenomenological description of the F parameters. The associated uncertainty of the effective solid angles is obtained by differentiating equation (33) with respect to F, and calculating the root mean square deviations of the appropriate variables.

$$\begin{aligned} d(\Delta\Omega^\dagger)/\Delta\Omega^\dagger &= \{ f_\mu / (1 - F f_\mu) \} \, dF \\ &\sim f_\mu \, dF \end{aligned} \tag{35}$$

where:

$d(\Delta\Omega^\dagger)$ - The uncertainty of the effective solid angle $\Delta\Omega^\dagger$.

dF - The uncertainty of the F parameter.

Given the uncertainty of F ($dF = \Delta = 0.05$), the uncertainty of the effective solid angle is typically less than two percent, depending (approximately) on the muon fraction.

4.4.8 ENERGY-LOSS

The Monte Carlo simulations indicated that if enerqy-loss of the particles was neglected, then small-angle multiple scattering effects cancelled out (refer to figure (4.10)). For low values of the pion energy, however, such a cancellation ceases to be exact. The effect is primarily due to the fact that the aperture that defines the geometric solid angle (the MWPC), and that for the particle identification system (the scintillators) are physically separated. The particles which are scattered into the system before the first aperture have further to travel and therefore more material to traverse than those which scatter out. As the pion (and muon) energies decrease, the particles that traverse larger distances suffer an increasing probability of either ranging-out (stopping) or of scattering out. Figure (4.11) shows the pion energy distribution as it shifts to lower energies traversing the apparatus. These effects lead to a reduction of the effective solid angle as the pion laboratory energy decreases beyond some threshold value. The magnitude of the associated correction is negligible (much less than 1%) for pions of momentum greater than 100 MeV/c. The values of effective solid angles corrected for energy-loss, and the size of the correction are tabulated in table (4.1).

Figure (4.10)

Schematic Representation of the Effect of Particle Energy-loss on the Effective Solid Angle.

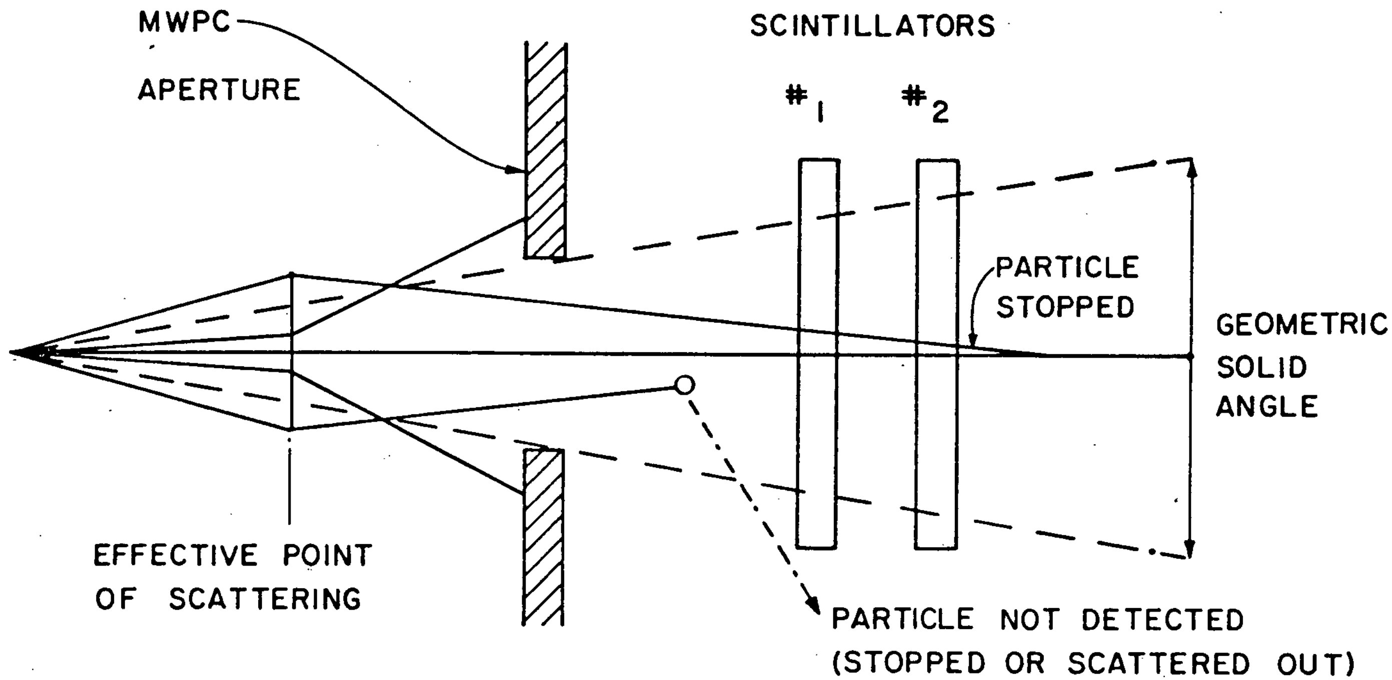

The trajectories of particles are indicated superimposed on the apparatus. The trajectories above the centre line represent those responsible for the cancellation of small-angle multiple-scatterings. Those below the line indicate the effect of ranging-out and large angle scatterings on the longer trajectory, and hence a mechanizm for the break down of such cancellations.

Figure (4.11)

Low Energy Pion Energy Distributions.

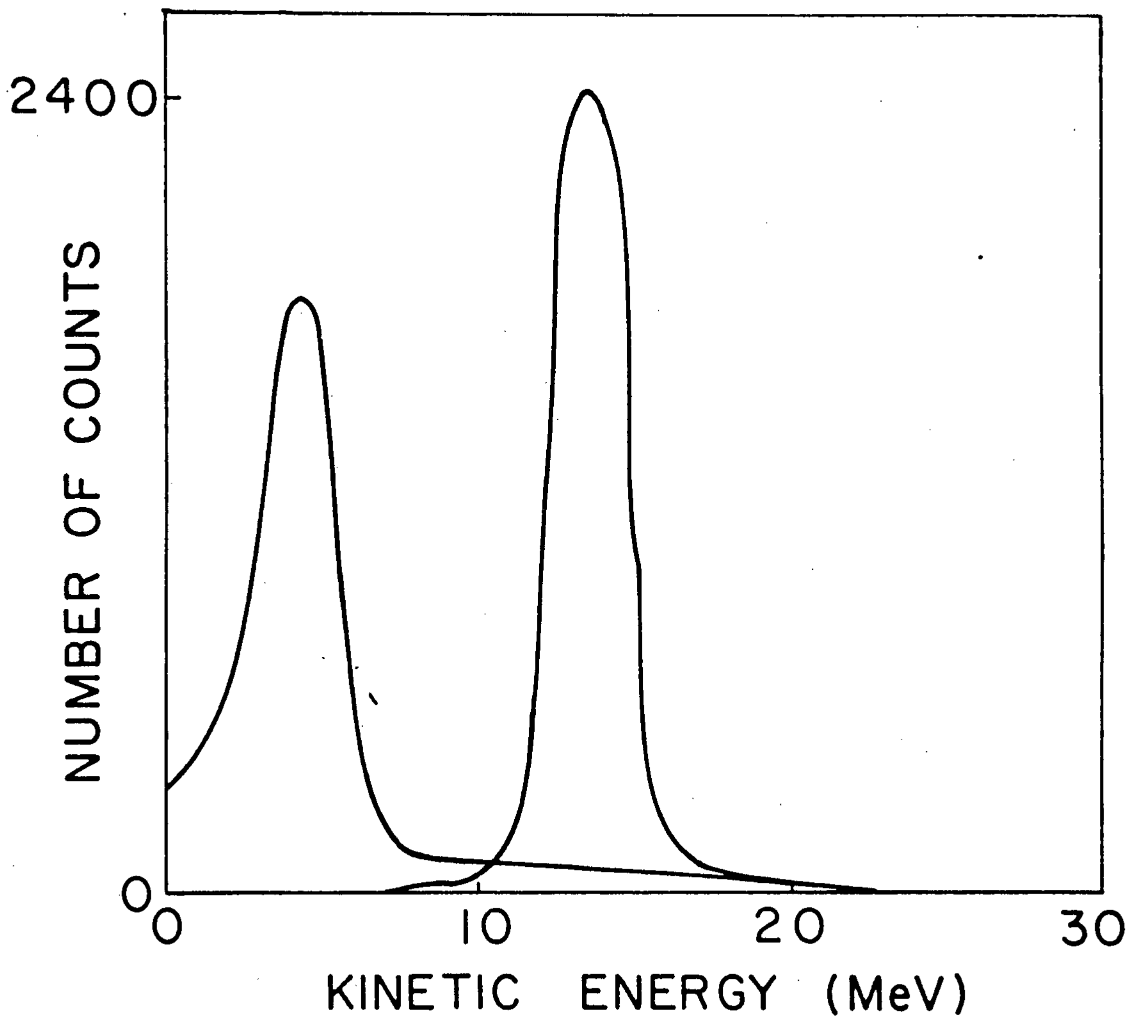

The energy distribution of pions is shown at the target (the higher energy distribution) and upon entering the final scintillator (sintillator #2).

Table (4.1)

The Corrections to Solid Angles Associated with Low Energy Pions.

Incident Proton Energy (MeV)	Pion Energy (MeV)	Pion Angle (C.M.) (degrees)	Target Thickness (cm)	Solid Angle correction Factor (± 2%)
350	12.3	138.6	0.340	-
350	14.0	134.9	0.300	0.91
350	16.0	131.0	0.270	0.95
350	17.0	128.9	0.260	0.96
350	28.1	110.2	0.330	0.98
375	13.8	146.1	0.071	0.89
375	21.3	132.6	0.110	0.98
375	28.5	121.9	0.083	0.99
375	35.1	113.0	0.070	1.00
375	14.1	145.4	0.250	-
375	18.6	136.9	0.320	0.94
375	19.6	135.2	0.340	0.95
375	23.6	128.8	0.350	0.96
375	33.3	115.3	0.240	1.01
425	26.2	142.7	0.069	0.99
425	32.7	134.3	0.089	1.00
450	26.1	150.5	0.058	0.96
450	31.3	143.2	0.067	1.00

4.5 DETECTOR AND GEOMETRIC CALIBRATIONS

Multi-wire proportional chambers delay-line read-out systems provide information on particle positions and trajectories as a function of delay-line timing differences measured with TDC's. In order to be able to infer spatial information, calibration of the system was necessary. The absolute positions of the MWPC's could then be determined through study of the results of simultaneous measurements of $pp \rightarrow \pi^+ d$ and $pp \rightarrow pp$ elastic reaction final state particle angular correlations. Detailed discussion of these calibrations, in addition to those of the scintillator positions is presented in the following sections.

4.5.1 MULTI-WIRE PROPORTIONAL CHAMBER CALIBRATION

Detection of an event initiated the reading of the spatial information from the cathode planes of the MWPC's. A delay-line read-out system such as that employed here involves the electrical connection of the various cathode wires at regularly spaced intervals along a delay-line (discussed in section (3.9)). A comparison of the arrival times of a cathode signal at the opposite ends of the delay-line thus provides quantities that must be calibrated to yield spatial coordinates.

When a MWPC was illuminated with radiation, data read from the cathode plane whose sense wires were oriented parallel to the anode plane wires contained information related to the position of the anode wires. An image of the anode wires could be observed by histograming the TDC channel number difference δ. This image, when combined with the known anode wire positions provided a straightforward means for internally calibrating this cathode plane.

Calibration of the delay-line read-out associated with the opposite cathode plane was more complex as no comparable interval technique could be employed. For this case, images of the scintillators were measured with the MWPC, and the calibration effected through the comparison of their apparent dimensions with those expected by geometry.

4.5.1.1 The Delay-Line

The printed circuit delay-lines used in such chambers are far from ideal. Electrical signals were both attenuated and dispersed when propagated along the delay-line. The overall effect (so far as the following analysis was concerned) was that the apparent group velocity of the signal varied along the delay-line. The form of the velocity dependence, however, was constrained to be symmetric about the center of the delay-line. For this reason, a small non-linear component was incorporated into the calibration relationship for the system (see section 4.5.1.3).

4.5.1.2 The Anode Wire Distribution Image

The anode wire distribution image function was denoted $T(\delta)$. It represented the probability of a delay-line signal being recorded with a (TDC) channel number difference δ, for full illumination of the MWPC surface. Such a distribution is illustrated in figure (4.12). Peaks associated with individual anode wires were easily identified. In addition, the envelope of the peaks was symmetric about the center. Figures (4.13) and (4.14) indicate the variation in the shape of the peaks associated with the central and edge regions respectively. These diagrams indicated that the distribution function could be approximated by a sum of normalized gaussian distributions of varying width (resolution) centered at each anode wire.

Let:

i = The sequential number of an anode wire.

δ_i = The channel difference number corresponding to the i^{th} wire.

σ_i = The standard deviation of the i^{th} Gaussian distribution.

Then,

$$T(\delta) = \sum_i \{ \exp(\delta-\delta_i)^2 / 2\sigma_i \} / \sqrt{2\pi\sigma_i} \qquad (36)$$

The parameters δ_i, and σ_i, were dependent on both the spacing of the anode wires and the electrical properties of the delay-line.

4.5.1.3 Calibration in the Vertical Direction

After the discrete relationship $\delta_i(x_i)$ between the channel number difference δ_i, and the corresponding position of the i^{th} anode wire x_i, was determined, inversion then

Figure (4.12)

The Anode Wire Distribution Image.

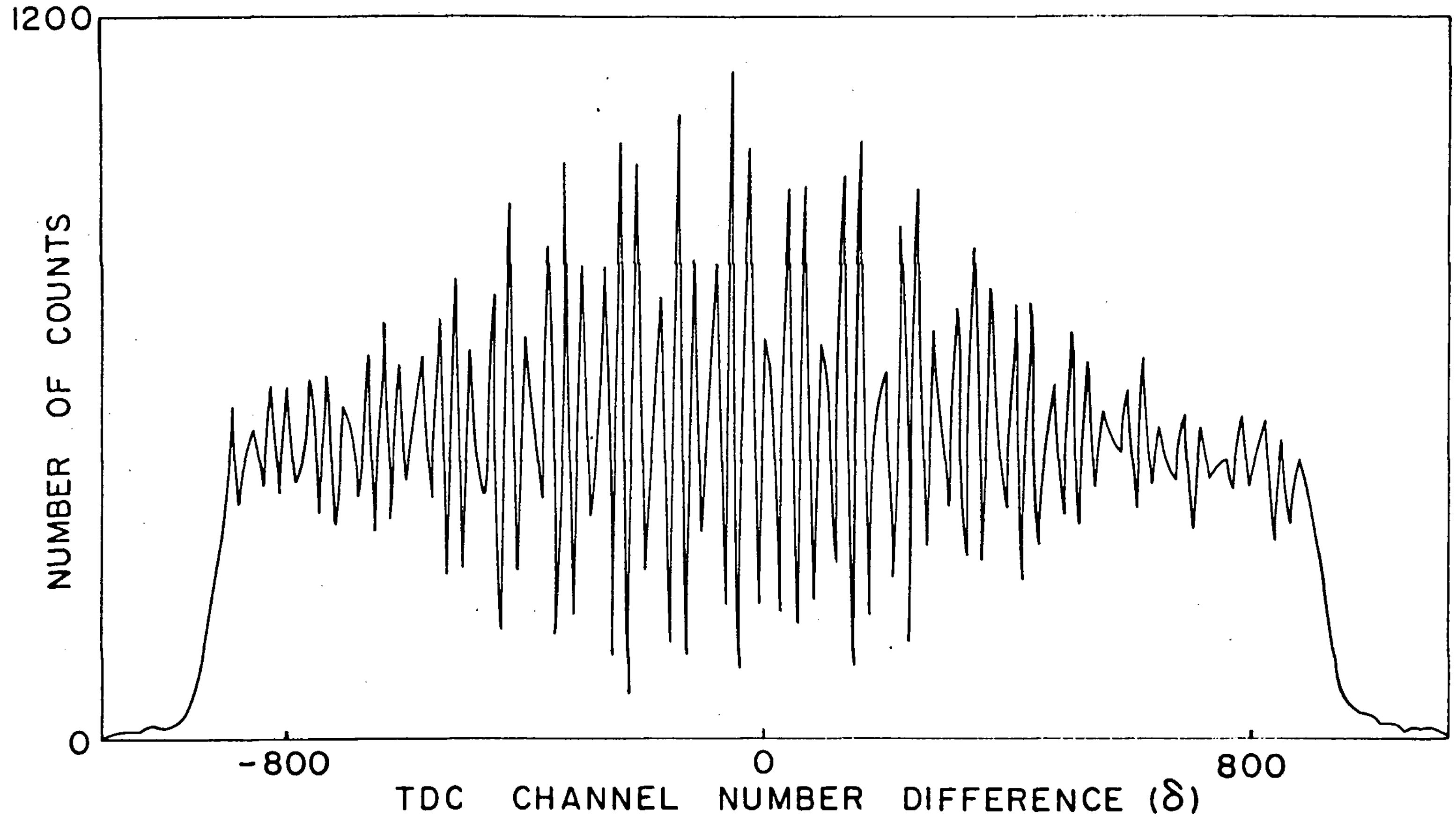

Figure (4.13)

The Anode Wire Distribution Image: Central region.

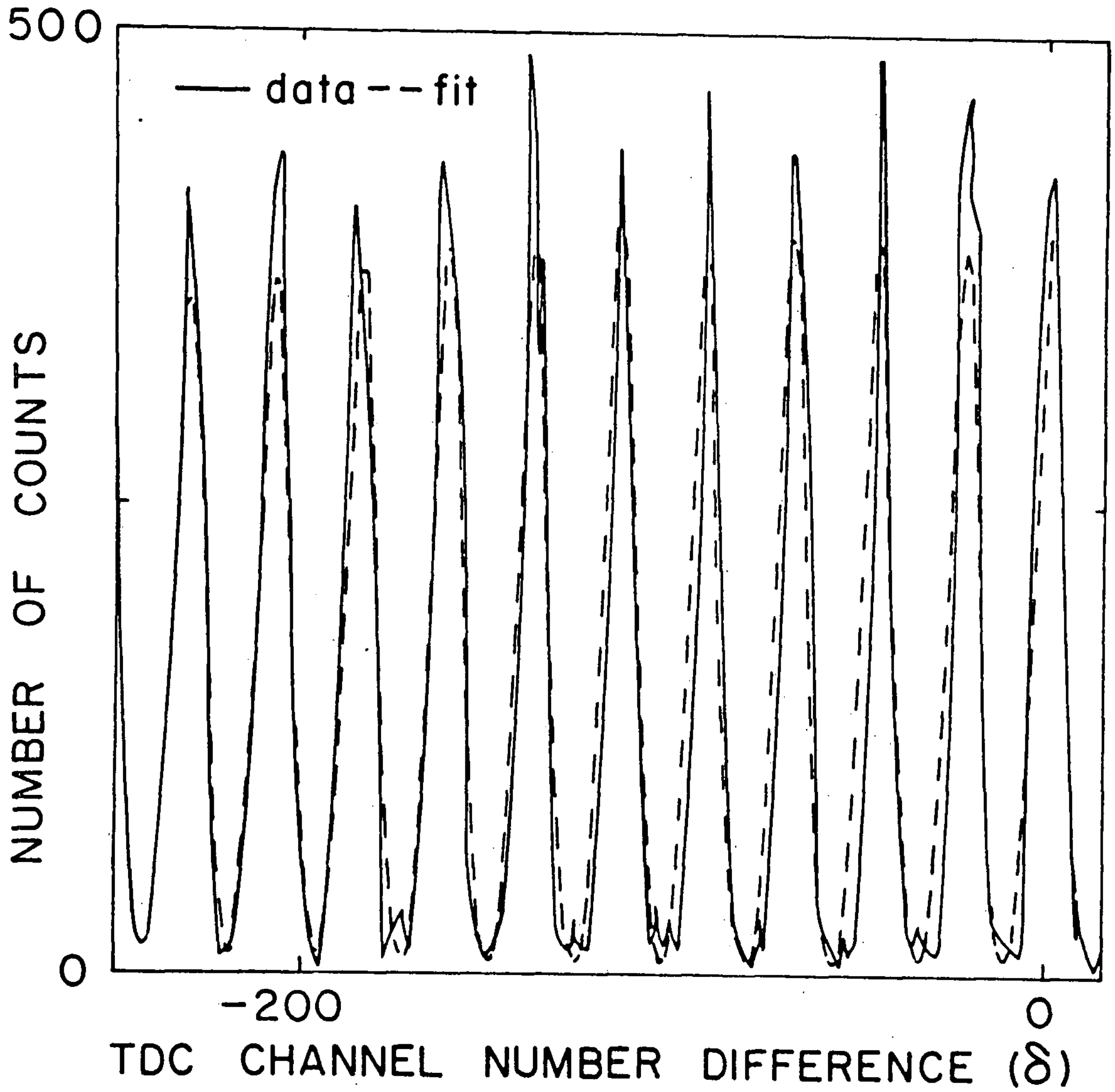

Figure (4.14)

The Anode Wire Distribution Image: Edge Region.

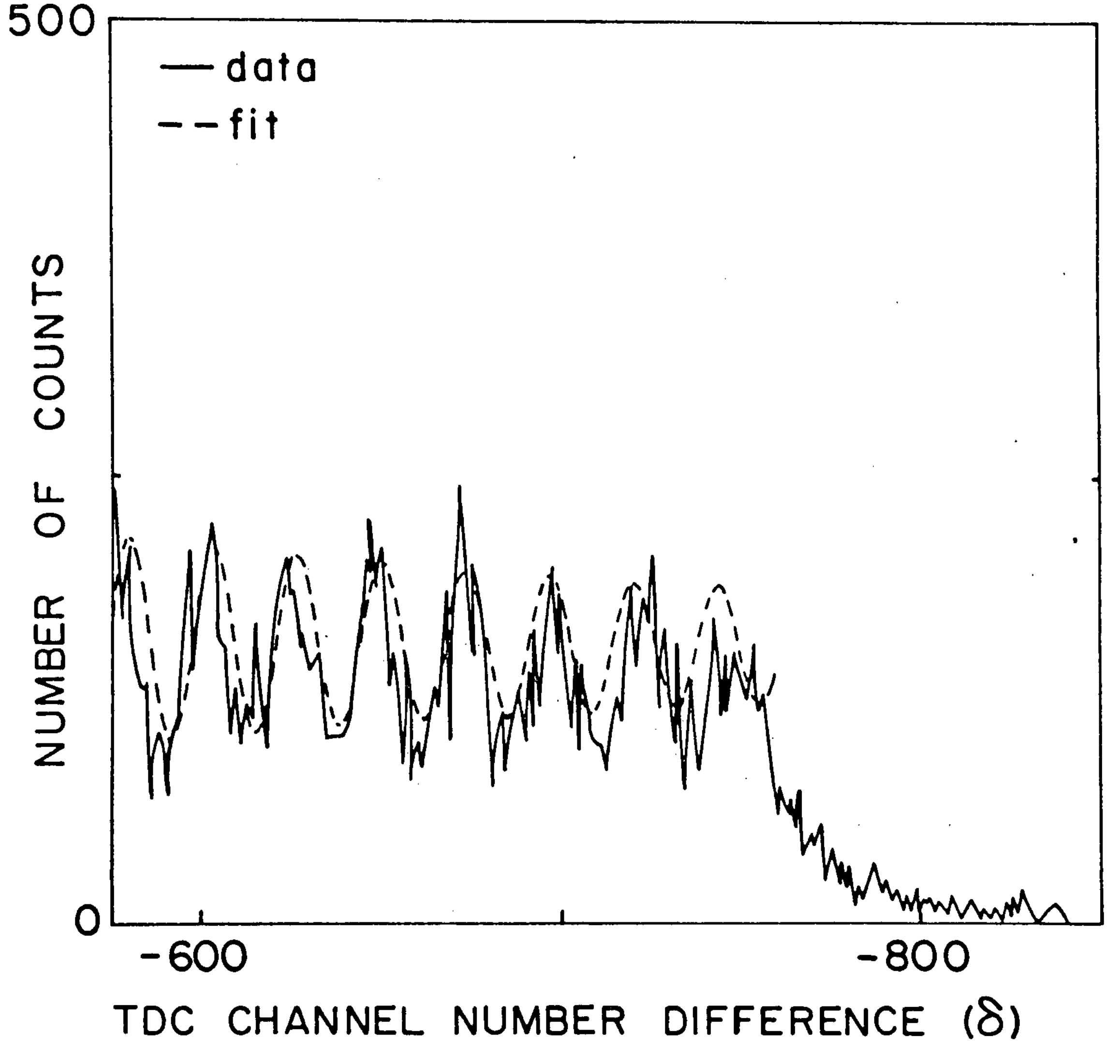

yielded the spatial position function $x(\delta)$. The symmetric form of the signal propagation velocity about the center of the delay-line x_c, constrains the form of δ. In particular, if the channel number difference δ_c is defined by;

$$\begin{aligned}\delta_c &= \delta(x_c) \\ &= \delta'(0)\end{aligned} \tag{37}$$

where:

$$\delta'(x) = \delta(\ x - x_c\ )$$

Then, given two positions, each a distance ΔX from the center of the delay-line, the function $\delta'(\pm\Delta X)$ is constrained to change by an equal magnitude, but by a differing direction (sign) relative to the central point ($\delta'(0)$), at each extreme point respectively, that is;

$$\delta'(\ \Delta x) = -\delta'(-\Delta x) \tag{38}$$

Therefore, $\delta'(x)$ is anti-symmetric, consequently, $\delta(x)$ is required to be anti-symmetric (neglecting an additive constant (instrumental)) about a central position x_c. Furthermore, a higher order term (cubic) was introduced to account for the non-linear effect of the position-dependendent signal propagation velocity within the delay-line. The functional relationship used was:

$$\delta(x)/a - \rho = (x-x_c)\{ 1 + \gamma(x-x_c)^2 \} \tag{39}$$

where

a - sets the overall scale

ρ - is an instrumental offset

x_c - defines the center (the point of anti-symmetry)

γ - defines the extent of non-linearity

The values of these parameters are obtained by a least squares fit of this function to the data points (x_i,δ_i).

As defined $\delta(x)$ is a cubic function which was readily inverted. By analogy with standard techniques[33], equation (39) was expressed in standard form;

$$0 = z^3 + 3qz - 2r \tag{40}$$

where:

$$z = x - x_c$$

$$3q = 1 / \gamma$$

$$-2r = (\rho - \delta/a) / \gamma$$

As the discriminant d, is positive, and all coefficients are real, then the real root of equation (40) is;

$$z = (r - \sqrt{d})^{1/3} + (r + \sqrt{d})^{1/3} \tag{41}$$

where the definition of the descriminant d, is ;

$$d = q^3 + r^2$$

Finally, the x coordinate is then;

$$x(\delta) = z + x_c \tag{42}$$

The results of such a calibration are depicted in figure (4.15) where the quantity $\Delta\delta_i$ is plotted versus the wire number for a typical run, where;

$$\Delta\delta_i = \delta_{i+1} - \delta_i \tag{43}$$

This quantity is shown since it is graphically more sensitive to the non-linear (γ) term then is $\delta_i(x)$. Here, the visible peak spacing represents the (0.2cm) anode wire separation. The parabolic shape, symmetric about the center wire (as opposed to a constant function) resulted from the non-linearity of the position function, $x(\delta_i)$.

4.5.1.4 Calibration in the Horizontal Direction

The read-out system of the cathode plane distinguished by sense wires perpendicular to those of the anode plane was calibrated with a different method. The size of each scintillator was measured with a MWPC. Comparison of its 'shadow' size to its known (projected) size provided the

Figure (4.15)

The Anode Wire Spacing.

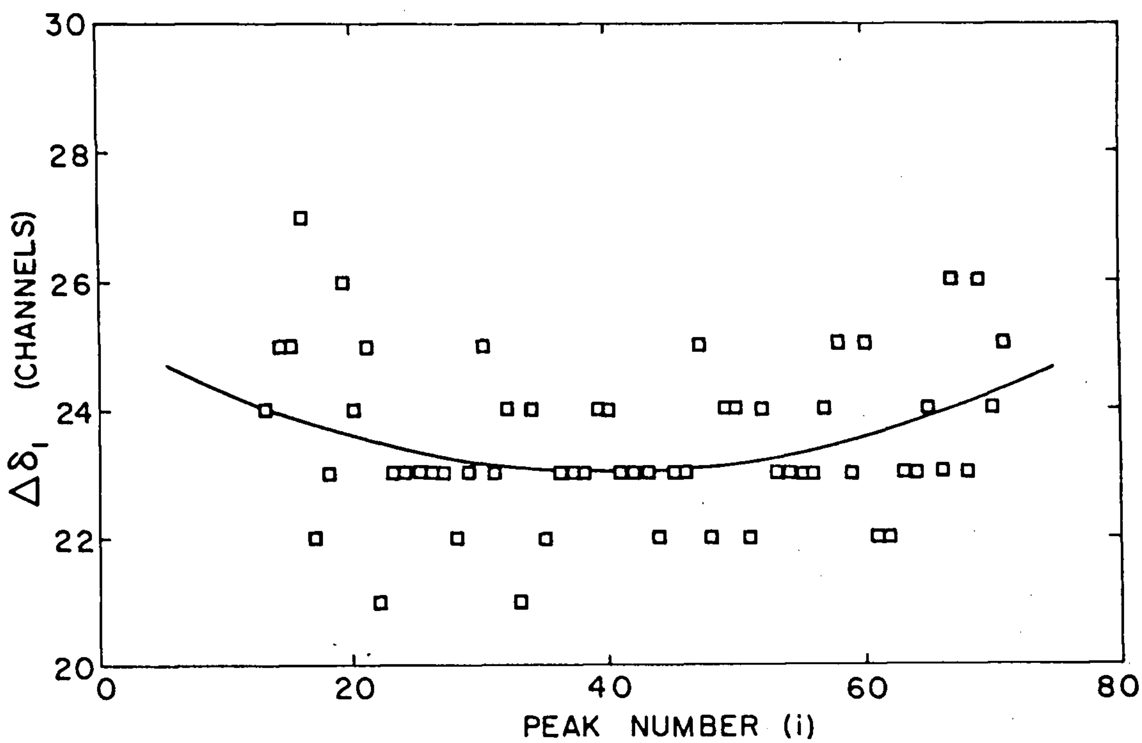

The interval ($\Delta\delta_i$) of the TDC Channel number difference δ, between anode wires as a function of the anode wire number. Each interval is associated with the 2.0 mm physical separation of the anode wires. The non-linear shape displayed indicates the non-linearity of the delay-line spatial calibration.

$$\sigma_i = a + b\{ 1 - \exp[(i - i_c) / 2\sigma_w] \} \tag{44}$$

where;

i_c = The center wire number.

σ_w = The Gaussian (envelope) width.

This form of the resolution σ_i, required for the description of $\Upsilon(\delta)$ shown in figure (4.12) and the previously determined channel number difference $\delta(x_i)$, were substituted into the equation (36) of the anode wire distribibution function $\Upsilon(\delta)$, and the free parameters a, and b, were fit (by least squares) to the data. The resulting a and b coefficients are used to calculate the resolution at the center, and at the edges of the detector. The results are:

Central Resolution: 0.05cm

Resolution more than 3cm from the center: 0.08cm

4.5.2 SCINTILLATOR CENTRAL OFFSETS

As described in the previous section, an image associated with each scintillator was projected with a particle beam onto a MWPC. The scintillator's image was measured and its dimensions and its position (in the Cartesian coordinate system appropriate to the MWPC) were deduced. The coordinates of the center of each scintillator are tabulated in table (4.2).

Table (4.2)

Relative Scintillator Central Offsets

Arm	x Centres		y Centres
	(c.m.)	(Degrees)	(c.m.)
D	0.57(16)	-0.13(4)	-0.04(20)
F	0.08(16)	0.04(7)	0.42(20)
B	0.00(16)	0.00(9)	0.00(20)

The measured separation of the scintillators within a detection telescope system (perpendicular to the central axis). The quantities in brackets represent the uncertainty of the last digits.

4.5.3 CALIBRATION OF THE DEUTERON ARM HORN APERTURE

An image of the deuteron horn aperture was formed on the deuteron MWPC. The vertical dimension and center of the aperture were deduced and the results also tabulated in table (4.3). Its known projected vertical length agrees with the value so determined.

4.5.4 ABSOLUTE CALIBRATION OF DETECTION ARM POLAR ANGLES

Because of systematic alignment errors in the measured positions of the two arms, it was possible for the angular coordinates of particles calculated as a function of their spatial coordinates (measured by a MWPC) to differ somewhat from the 'actual' values. The term 'absolute' used here, implies the actual values of the angular coordinates. The absolute polar coordinates (with respect to the beam direction) of a pair of correlated particles are absolutely specified by the two body kinematics of the reaction. The measurement of their associated azimuthal coordinates (measured in the plane normal to the beam direction), however, is known only relative to an arbitrary origin. This is due to the cylindrical symmetry of the reaction kinematics about the axis of the beam direction. Nonetheless, relative coordinates of the two particles were simply related by the coplanarity of the two-body final state.

The polar angle of a particle deduced from a MWPC spatial measurement (that is with no corrections applied)

Table (4.3)

Deuteron-Horn Aperture Positional Calibration.

Projected width:	10.5cm
Measured width:	10.5±0.02cm
Measured centre:	-1.0±0.02cm

was designated, by way of the superscripts indicated, $\hat{\theta}$, when deduced from the pion MWPC measurements, or $\check{\theta}$, when deduced from the deuteron MWPC measurements. In each case, the measured angle was related to the absolute angles, θ_π or θ_d, through the additive polar offsets η_π, or η_d;

$$\hat{\theta} = \theta_\pi - \eta_\pi; \qquad \text{Pion arm.} \tag{45}$$

$$\check{\theta} = \theta_d - \eta_d; \qquad \text{Deuteron arm.}$$

Absolute calibration of the polar offsets of both of the detection arms was based on the kinematic properties of two reactions that were measured simultaneously. At particular values of the incident beam energy and angular settings of the detection arms, both $pp \rightarrow \pi^+ d$ events and $pp \rightarrow pp$ elastic events could be simultaneously detected. The differing kinematic properties of the two reactions constrained the intersection (detection) of the trajectories of the associated reaction products to differing areal regions of the MWPC's active surfaces. The four regions, one for each of the reaction products, are indicated in figure (4.16). Since the pion and deuteron MWPC's define the acceptance solid angle for detection of the $pp \rightarrow \pi^+ d$ and $pp \rightarrow pp$ reactions respectively; the pion and deuteron MWPC's are fully illuminated with pions and protons respectively.

As a notational aid to specify in which detection arm, an otherwise indistinguishable proton is detected, the following notation is introduced;

Figure (4.16)

Pion, Deuteron, and Elastic-Proton Detection Regions.

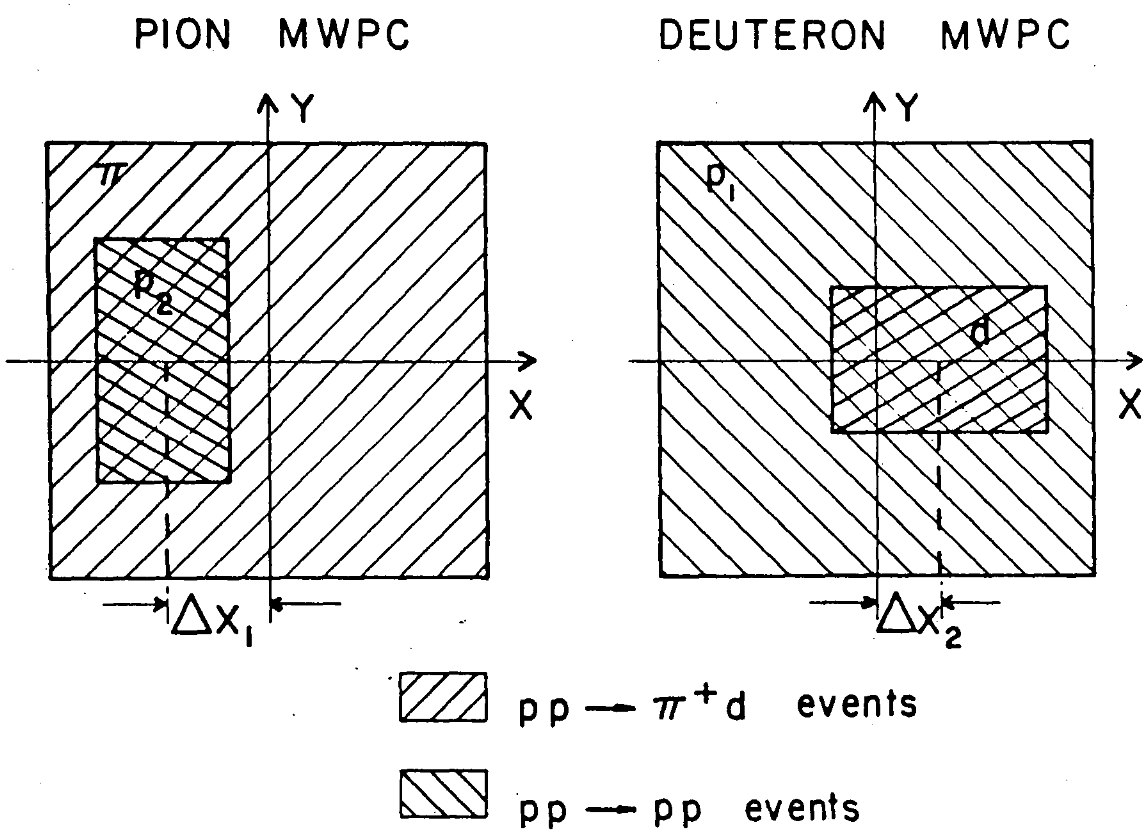

The shaded regions of each MWPC shematically indicate the areal regions of detection of particles associated with either of the two simultaneous reactions. The axes represent the rectangular coordinate system of the MWPC detector. The linear separation of two such regions on the MWPC surfaces X_1 and X_2, are related to the angular quantities Δ_1 and Δ_2, discussed in the text.

p_1 - Implies proton detection by the pion detector.

(46)

p_2 - Implies proton detection by the deuteron detector.

Although the regions depicted in figure (4.16) are specified in the Cartesian coordinate system appropriate to the appropriate MWPC, the associated polar angle distributions are qualitatively similar (within the small angle approximation framework).

The opening angles $\Delta_{pp\rightarrow\pi^+d}$ and $\Delta_{pp\rightarrow pp}$, of the indicated reactions is then defined by the central values of the polar angle distributions associated with the four regions indicated in figure (16), that is;

$$\Delta_{pp\rightarrow\pi^+d} = \theta_\pi + \theta_d = \hat{\theta}_\pi - \eta_\pi + \check{\theta}_{p_2} - \eta_d \qquad (47)$$

$$\Delta_{pp\rightarrow pp} = \theta_{p_1} + \theta_{p_2} = \hat{\theta}_{p_1} - \eta_\pi + \check{\theta}_{p_2} - \eta_d$$

where the superscripted quantities take on the central value of the associated polar angle distributions. The unknown polar offsets η_π and η_d, will cancel out when the difference of these opening angles is formed; that is;

$$\Delta_{pp\rightarrow\pi^+d} - \Delta_{pp\rightarrow pp} = \hat{\theta}_\pi + \check{\theta}_d - (\hat{\theta}_{p_1} + \check{\theta}_{p_2}) \qquad (48)$$

This expression can be rewritten in terms of quantities designated $\Delta 1$ and $\Delta 2$, which are defined in terms of the differences between the central positions of the two polar angle distributions observed on each MWPC respectively (refer to figure (4.16)). That is if:

$$\Delta_1 = \hat{\theta}_\pi - \hat{\theta}_{p_1} = \theta_\pi - \theta_{p_1} \tag{49}$$

$$\Delta_2 = \check{\theta}_d - \check{\theta}_{p_2} = \theta_d - \theta_{p_2}$$

then;

$$\Delta_{pp\to\pi^+d} - \Delta_{pp\to pp} = \Delta_1 + \Delta_2 \tag{50}$$

These Δ's then, are each defined within a specific MWPC, and are thus independent of the polar angle offsets η_π and η_d.

These Δ's could be deduced from the (uncalibrated) arm positions (which define $\hat{\theta}_\pi$ and $\check{\theta}_{p_2}$ by way of the acceptance solid angle definitions of the associated MWPC's) together with the measured angular correlations (section 4.3.2.3.) representing the deviations of distributions from their positions; that is;

$$\Delta_1 = \hat{\theta}_\pi - \{ \Theta_{pp}(\check{\theta}_{p_2}) - \Delta\theta_{pp} \} \tag{51}$$

$$\Delta_2 = \{ \Theta_{\pi d}(\hat{\theta}_\pi) - \Delta\theta_{\pi d} \} - \check{\theta}_{p_2}$$

But the Δ's could also be cast as a function of the absolute unknown angles θ_π and θ_{p_2};

$$\Delta_1 = \Theta_{\pi d}^{-1}(\theta_{p_2} + \Delta_2) - \Theta_{pp}(\theta_{p_2}) \tag{52}$$

$$\Delta_2 = \Theta_{\pi d}(\theta_\pi) - \Theta_{pp}(\theta_\pi - \Delta_1)$$

Where these two equations are dependent of course.

Once the values of the Δ's were determined from the experimental values (equation (51)) , they were substituted into equation (52); which was then solved numerically using the required kinematic functions, to yield the absolute polar values of the angles of the arms. The arm offsets, were then simply obtained from equation (45). As these offsets were not expected to change significantly throughout the experiment, they were calculated in detail only for one run. The results are tabulated in table (4.4).

4.5.5 CALIBRATION OF THE AZIMUTHAL ANGLE IN THE PLANE NORMAL TO THE BEAM DIRECTION

The angular offsets in this coordinate result from vertical offsets of the detection systems. The vertical offset with respect to the surveyed position of the forward pion detector was arbitrarily taken to be zero (as the origin for this coordinate is arbitrary). The relative vertical offset of the other detectors were then deduced on the basis of the measured coplanarity distribution (section 4.3.2.3.) of the two-body final states. The results of these calibrations are tabulated in table (4.4).

4.6 CARBON BACKGROUND

Carbon background events arose from interaction of the incident proton beam with nuclei of carbon in the target. Polyethelene, the target material, is a polymer consisting of hydrogen and carbon atoms in a two-to-one ratio. The

Table (4.4)

The Experimentally Determined Detector Offsets.

Arm	Axis	Survey	MWPC	Scint.#1	Scint.#2
d	X	-11.91(2)°	-11.878(3)°	-11.878(3)°	-12.01(4)°
	Y		0.91(1)cm	0.91(1)cm	0.87(2)cm
πF	X	0.26(4)°	-0.14(1)°	-0.14(1)°	-0.10(7)°
	Y		0.00cm	0.00cm	0.42(2)cm
πB	X	0.29(6)°	-0.05(1)°	-0.05(1)°	-0.05(9)°
	Y		0.06(1)cm	0.06(1)cm	0.06(2)cm

The Surveyed angle of the arm is mesured with respect to the physical centre of The MWPC. The center of the first scintillator is taken here as the MWPC centre, which is the reason for the magnitude of the difference between the survey and MWPC offsets.

fraction of events within a data set due to carbon background could be reduced by two methods:

1) Event Identification; imposition of suitable constraints quantities such as; the energy-losses, the time-of-flights, and (in the case of the analyzing power data) the angular correlations, required to define an event.

2) Background Subtraction; direct subtraction of the number of carbon background events as determined from data collected with a carbon target.

The fraction of carbon background events in a sample could not be reduced to less than approximately three percent by method (1). Examination of data collected with a carbon target indicated that the events which survived the pulse-height and energy-loss constraints had interesting properties. In particular, their angular correlation and coplanarity distributions were similar to those of the $pp \rightarrow \pi^+ d$ reaction. Although the distributions were considerably more diffuse, they were centered at the same angles as were those of the $pp \rightarrow \pi^+ d$ distributions. In short, the observed particles which had the same energy-loss and time-of-flight characteristics as those of the free $pp \rightarrow \pi^+ d$ reaction, were also distributed, on average, according to the same two-body kinematics.

Thus, the apparent $pp \rightarrow \pi^+ d$ character of these carbon background events suggested a quasi-free $pp \rightarrow \pi^+ d$ origin within the carbon nucleus[34]. That is, the incident proton interacted with one of the nucleons, (a proton) bound within the carbon nucleus, via a two-body reaction with the rest of the carbon nucleons participating only as 'spectators.' The momenta (and thus angular correlations) of the final-state particles could be spread out relative to those of the free pion production reaction because of the fermi momentum (characteristic of bound nucleons) of the struck nucleon.

4.6.1 MEASUREMENT OF THE CARBON BACKGROUND

Carbon background measurements were taken with a carbon target, at several proton beam energies and angular settings of the detection arms. The beam current was monitored by the polarimeter since the use of the pp-elastic monitor was inappropriate without a hydrogen bearing target. The precise calibration of the polarimeter was, however, unknown. Thus, in each case the data were cross normalized to a similar run taken with a polyethelene target where the beam current was measured with both pp-elastic and polarimeter monitors simultaneously. The number of carbon background events as a fraction of the number of $pp \rightarrow \pi^{+}d$ events was thereby determined. The results for a typical proton energy are illustrated in figure (4.17). The detector efficiencies were not taken into account during the following analysis due to the ambiguties associated with their definition when a carbon target was employed. Nonetheless, since the detector efficiencies were expected, in general, to vary slowly, and since the background is determined from a ratio of two (usually) consecutive runs, the detector efficiencies were expected to cancell.

A quantity analogous to the differential cross-section for the carbon background was formed. Its definition was based on two assumptions:
First, the reaction was a two-body process having the same kinematic description as that of the free $pp \to \pi^+ d$ reaction. Second, the acceptance (effective solid angle) of the detection apparatus was identical for the quasi-free and the $pp \to \pi^+ d$ reactions. The latter assumption, it will be shown, has limited regions of application. As a result of these two assumptions an effective carbon background differential cross-section is defined by;

$$d\sigma_c/d\Omega = 2\ f_c(\theta_\pi^*)\ d\sigma/d\Omega \qquad (53)$$

where:

$d\sigma_c/d\Omega$ - The carbon background differential cross-section.

$f_c(\theta_\pi^*)$ - The fraction of carbon background events to $pp \to \pi^+ d$ events.

$d\sigma/d\Omega$ The $pp \to \pi^+ d$ differential cross-section (estimated, see text)

The factor of two results from the ratio of hydrogen to carbon atoms in the target. As precision values of the carbon background were not required, the values of the $pp \to \pi^+ d$ differential cross-section were obtained from

Figure (4.17)

The Fractional Carbon Background at 450 MeV.

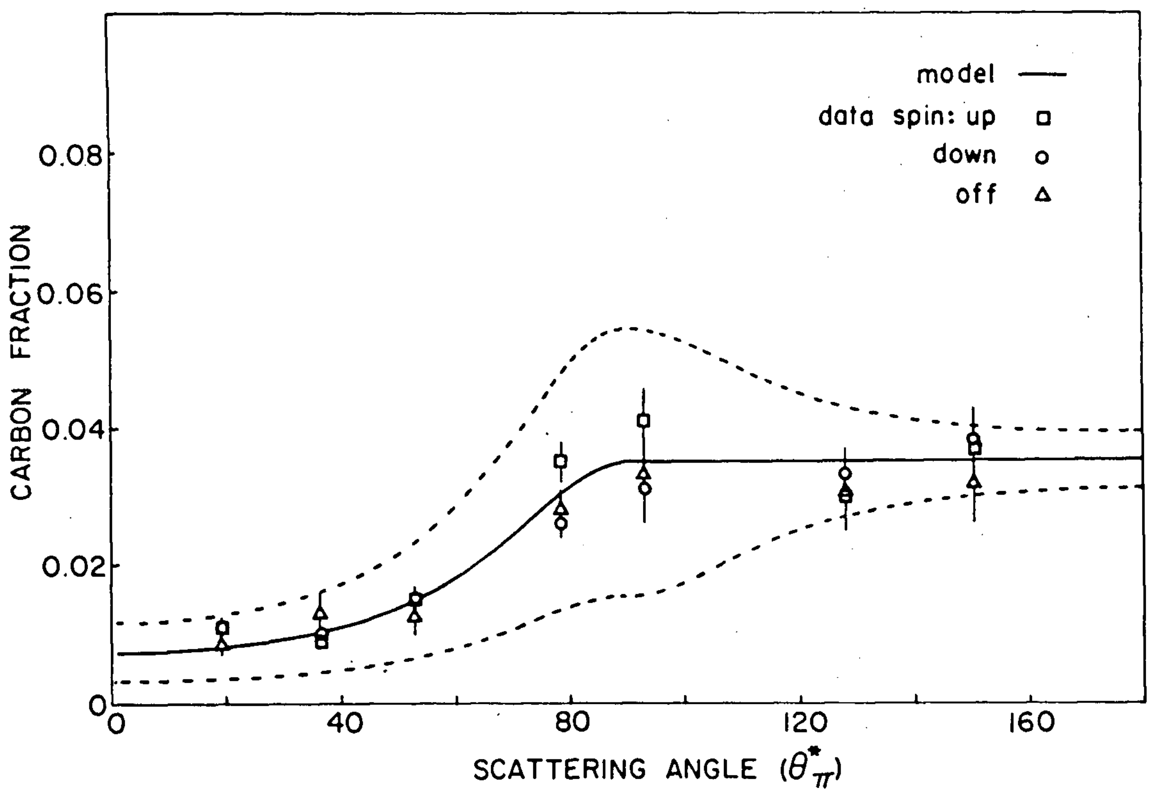

The number of detected carbon background events as a fraction of the number of detected pp→π^+d events. The solid line represents the predictions of the quasi-free pp→π^+d model of the carbon background. The error bars represent statistical uncertainties only.

published data[35].

4.6.2 QUASI-FREE PARAMETERIZATION OF THE CARBON BACKGROUND

The carbon background differential cross-section was parameterized on the basis of the quasi-free reaction model discussed above. It was assumed that the angular distribution of the carbon background differential cross-section would have the same shape, (but different magnitude) as that of the free $pp \rightarrow \pi^+ d$ reaction. Thus,

$$d\sigma_c/d\Omega = \lambda \; d\sigma/d\Omega \tag{54}$$

$$= \lambda \; a_0^{00}/(4\pi) \; \{ \sum_{i=0,2,\ldots} (a_i^{00}/a_0^{00}) \; P_i(\cos(\theta_\pi^*))$$

$$+ \; \bar{p}\cdot\bar{n} \sum_{i=1,2,\ldots} (b_i^{no}/a_0^{00}) \; P_i^1(\cos(\theta_\pi^*)) \; \}$$

Where the coefficient λ, scaled the magnitude of the angular distribution relative to that of the free $pp \rightarrow \pi^+ d$ reaction. When presented in this form the terms that define the shape of the angular distribution are inside the curly brackets. Since the carbon background typically represented a three percent correction to the $pp \rightarrow \pi^+ d$ differential cross-sections, its form could by reduced in complexity at the expense of only a small loss of precision (about ten per cent) by the following approximations:

1) The ratio a_2^{00}/a_0^{00} is approximatly constant over beam energies from 350 MeV to 500 MeV, that is

$$1.0 < a_2^{00}/a_0^{00} < 1.1$$

The value of this ratio averaged over the beam energies used to collect the data is therefore denoted k;

$$k = 1.08 \cong a_2^{oo}/a_0^{oo}$$

2) The higer order terms a_i^{oo}/a_0^{oo}, are neglected since their magnitudes are constrained by;

$$a_4^{oo}/a_0^{oo} < 0.1$$

$$a_6^{oo}/a_0^{oo} \cong 0.0$$

3) All polarization terms b_i^{no}/a_0^{oo}, are neglected since their magnitudes are constrained by;

$$|b_1^{no}/a_0^{oo}| \lesssim 0.1$$

$$b_2^{no}/a_0^{oo} \cong 0.0$$

$$b_3^{no}/a_0^{oo} < 0.05$$

$$b_4^{no}/a_0^{oo} \cong 0.0$$

Therefore, to this limited precision, only the first two terms of the unpolarized differential cross-section sum are required. That is;

$$d\sigma_c/d\Omega = \lambda\ a_0^{oo}/(4\pi)\ \{\ P_0(\cos(\theta_\pi^*)) + (a_2^{oo}/a_0^{oo})\ P_2(\cos(\theta_\pi^*))\ \} \tag{55}$$

Evaluating the Legendre functions and substituting the average value k for the a_2^{oo}/a_0^{oo} ratio, yields;

$$d\sigma_c/d\Omega = \lambda\ a_0^{oo}/(4\pi)\ \{\ 1 + k\ \cos^2(\theta_\pi^*)\ \} \tag{56}$$

In this approximation, the shape of the differential cross-section is independent of the beam energy and the magnitude is proportional to the total cross-section $a_0^{0°}$, of the $pp \rightarrow \pi^+ d$ reaction. In this way all of the carbon data can be considered simultaneously. Dividing both sides of this expression by the total cross-section $a_0^{0°}$, yields;

$$(a_0^{0°})^{-1}\, d\sigma_C/d\Omega = \lambda/(4\pi)\ \{\ 1 + k\ \cos^2(\theta_\pi^*)\ \} \qquad (57)$$

Therefore, all of the carbon background data could, in principle, be described by a simple quasi-free reaction model containing only one free parameter, λ.

The observed carbon background differential cross-section, however, appears to fall below this prediction in the forward hemisphere ($\theta_\pi^* < 90°$). This is depicted in figure (4.18) where the differential cross-section normalized to the total cross-section $a_0^{0°}$, is plot against the quantity $\cos(\theta_\pi^*)|\cos(\theta_\pi^*)|$. If equation (57) were satisfied, the plot would exhibit a mirror symmetry about the point $\cos(\theta_\pi^*)=0$.

An explanation of this asymmetry was based on differing acceptance of the apparatus for each of the two (quasi-free vs. free) reaction types. This resulted from the weak angular correlation of the quasi-free reaction final state particles. The quasi-free reaction effective acceptance solid angle could not be evaluated (with the existing Monte Carlos simulation procedure) since the angular distribution of the final state particles was unknown. Nonetheless the relative decrease of the quasi-free reaction (product) detection acceptance could be quantitivly explained by the

Figure (4.18)

The Effective Differential Cross-Section of the Carbon Background as a Function of cos(θ)|cos(θ)|.

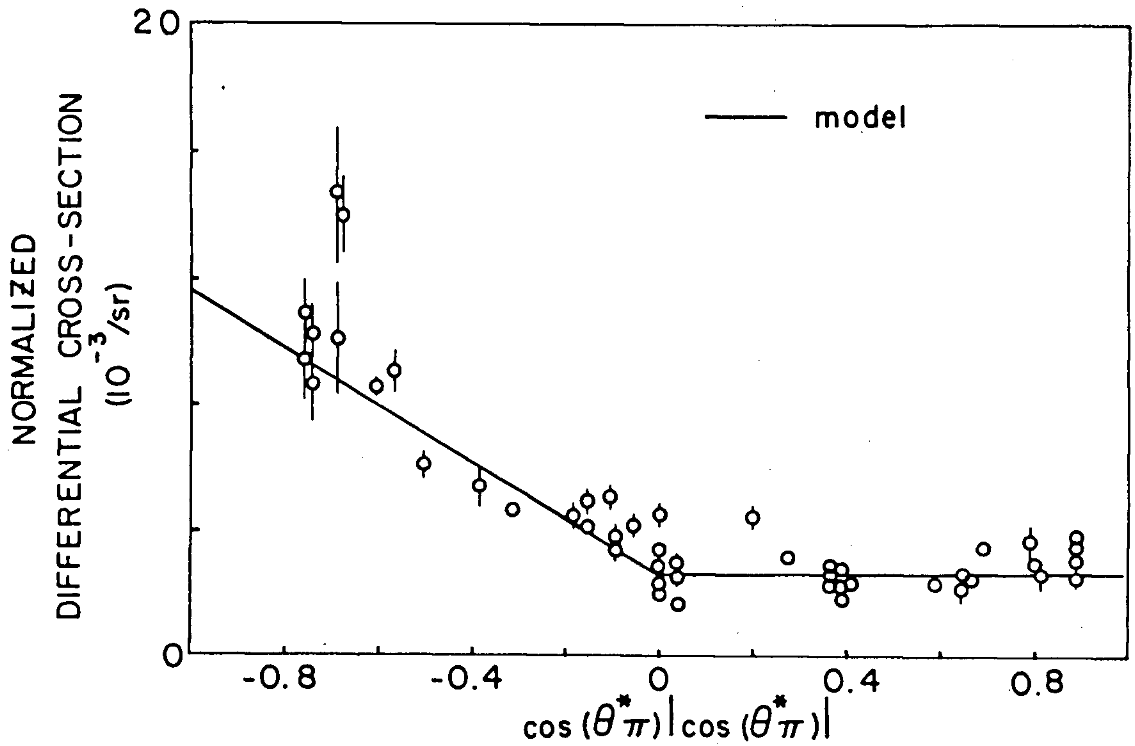

The carbon background differential cross-sections normalized to the total $pp \rightarrow \pi^+ d$ cross-section is plot as a function of cos(θ)|cos(θ)|. Carbon data of all energies is included. The line, again, represents the predictions of the model discussed in the text.

detector geometery and the ($pp \to \pi^+ d$) reaction kinematics.

In effect, then, the method of calculation of the carbon background differential cross-sections broke down in the forward hemisphere (in particular, assumption #2; section 4.6.1).

Nonetheless, the shape of the carbon background solid angle could be fit to the following semi-phenomenological model;

$$d\sigma_C/d\Omega/\, a_0^{0\circ} = \begin{cases} \lambda/(4\pi)\ \{\ 1 + k\ \cos^2(\theta_\pi^*)\ \}; & \text{if } \theta_\pi^* > 90^\circ. \\ \lambda/(4\pi)\ \{\ 1 + k\ \cos^2(90^\circ)\}; & \text{if } \theta_\pi^* \le 90^\circ. \end{cases} \qquad (58)$$

Where the shape of the carbon background in the forward hemisphere has been approximated with a constant function.

4.6.2.1 Fit of the Carbon Background to the Model

The two parameters λ, and k, were fit to the carbon data. The resulting coefficient k, was consistent with the average value of the ratio $a_2^{0\circ}/a_0^{0\circ}$.

Therefore, the carbon background was found to be described to sufficient accuracy by the relation;

$$d\sigma_c/d\Omega = \lambda \{ d\sigma/d\Omega \pm a_0^{0}{}^{\circ}\Delta \} \tag{59}$$

where:

$\lambda \quad = 0.07$

$\Delta \quad = 0.02$

The carbon data and this description of it are plotted in figure (4.19).

4.7 EXPERIMENTAL RESULTS.

4.7.1 THE DIFFERENTIAL CROSS-SECTIONS: UNPOLARIZED BEAM

The differential cross-sections presented here were calculated as discussed in section (4.2.). Here, equation (04) is rewritten as a function of ζ;

$$d\sigma/d\Omega = \zeta/\Delta\Omega^{\dagger} - \tfrac{1}{2}(d\sigma_c/d\Omega) \tag{60}$$

where,

$$\zeta = (N_p - N_r) / (N_{int} \epsilon) \tag{61}$$

Differential cross-sections evaluated by this means for the four data sets associated with the unpolarized incident beam energies of: 350 MeV, 375 MeV, 425 MeV,and 475 MeV, and are shown as a function of $\cos^2(\theta_\pi^*)$ in figures (4.20),(4.21),(4.22), and (4.24) respectively. The lines indicated on the figures represent a fit to the data using Legendre polynomials. In addition, the numerical values for the cross-section are tabulated in

Figure (4.19)

The Effective Differential Cross-Section of the Carbon Background.

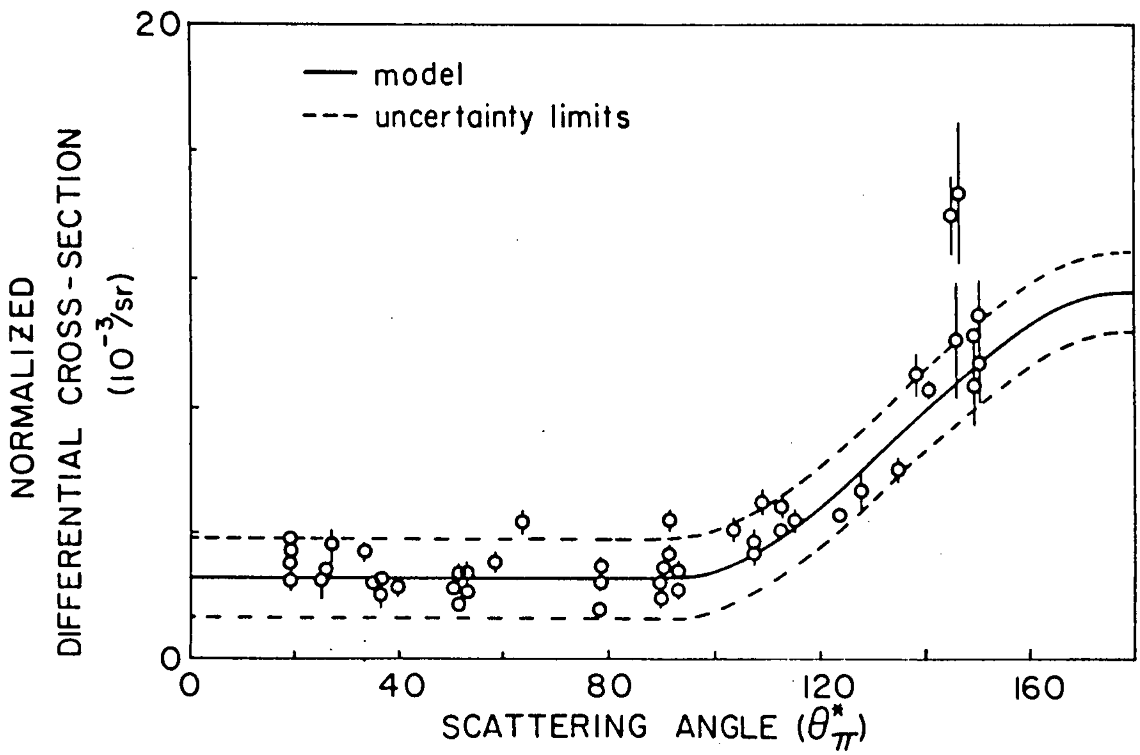

The carbon background differential cross-sections normalized to the total $pp \rightarrow \pi^+ d$ cross-section is plot as a function of the C.M. scattering angle. Carbon data of all energies is included. The line, again, represents the predictions of the model discussed in the text.

Figure (4.20)

The 350 MeV. Differential Cross-Sections.

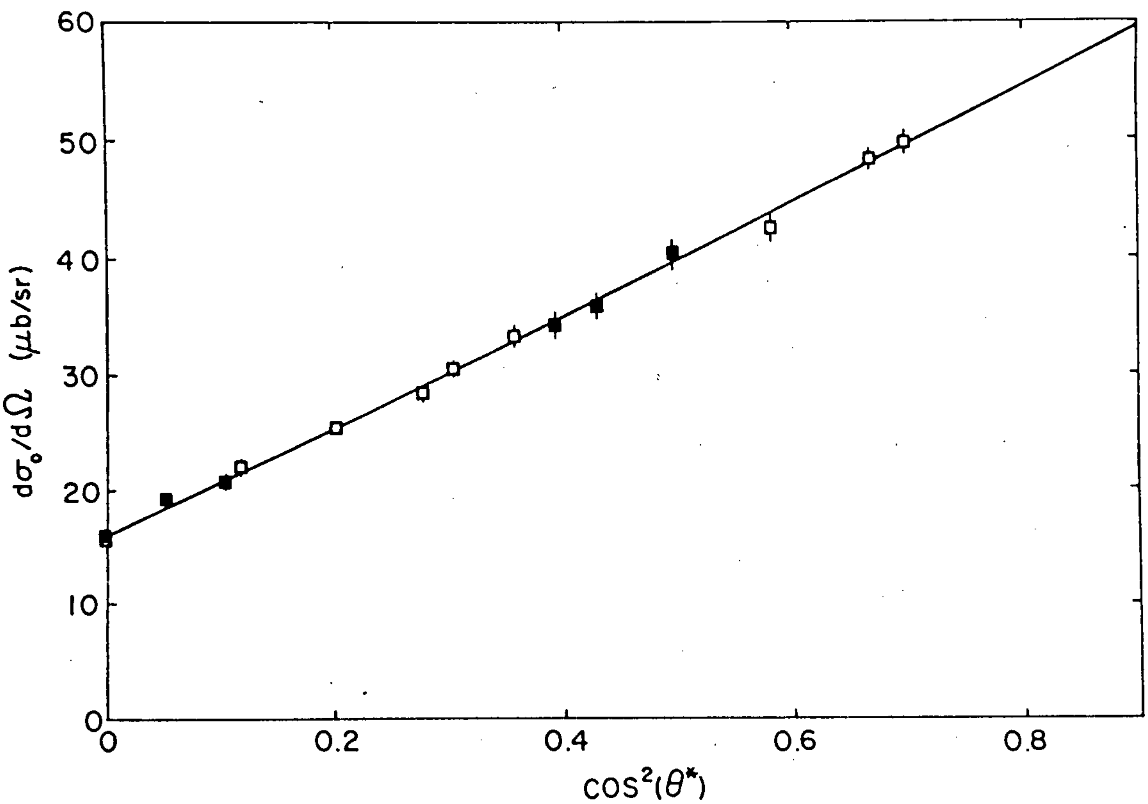

The differential cross-sections shown here are obtained from data collected with an unpolarized incident proton beam. Solid points indicate results deduced from measurements with the backward pion detection arm. The line represents the results of a fit of a fourth order Legendre polynomial to these results.

Figure (4.21)

The 375 MeV. Differential Cross-Sections.

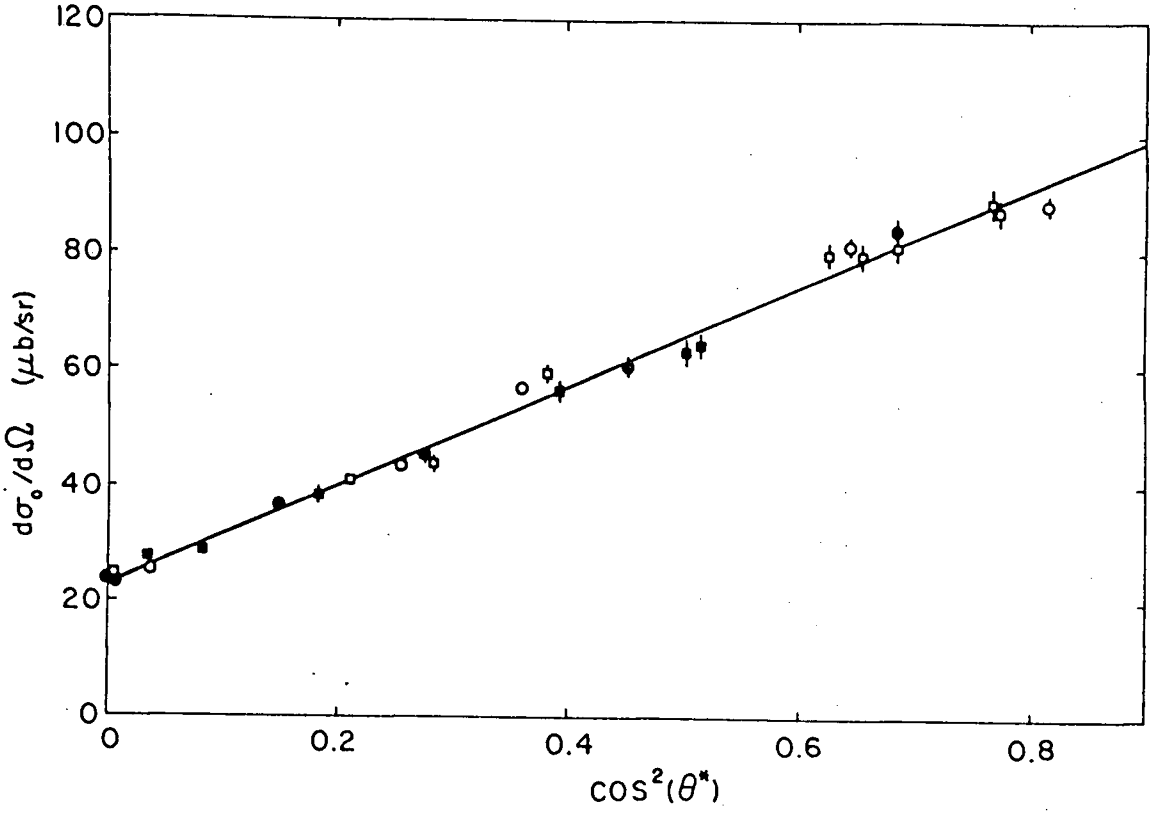

The differential cross-sections shown here are obtained from data collected with unpolarized and polarized incident proton beams, represented on the figure by circles and squares respectively. Solid points indicate results deduced from measurements with the backward pion detection arm. The line represents the results of fits of fourth order Legendre polynomials to these results.

Figure (4.22)

The 425 MeV. Differential Cross-Sections.

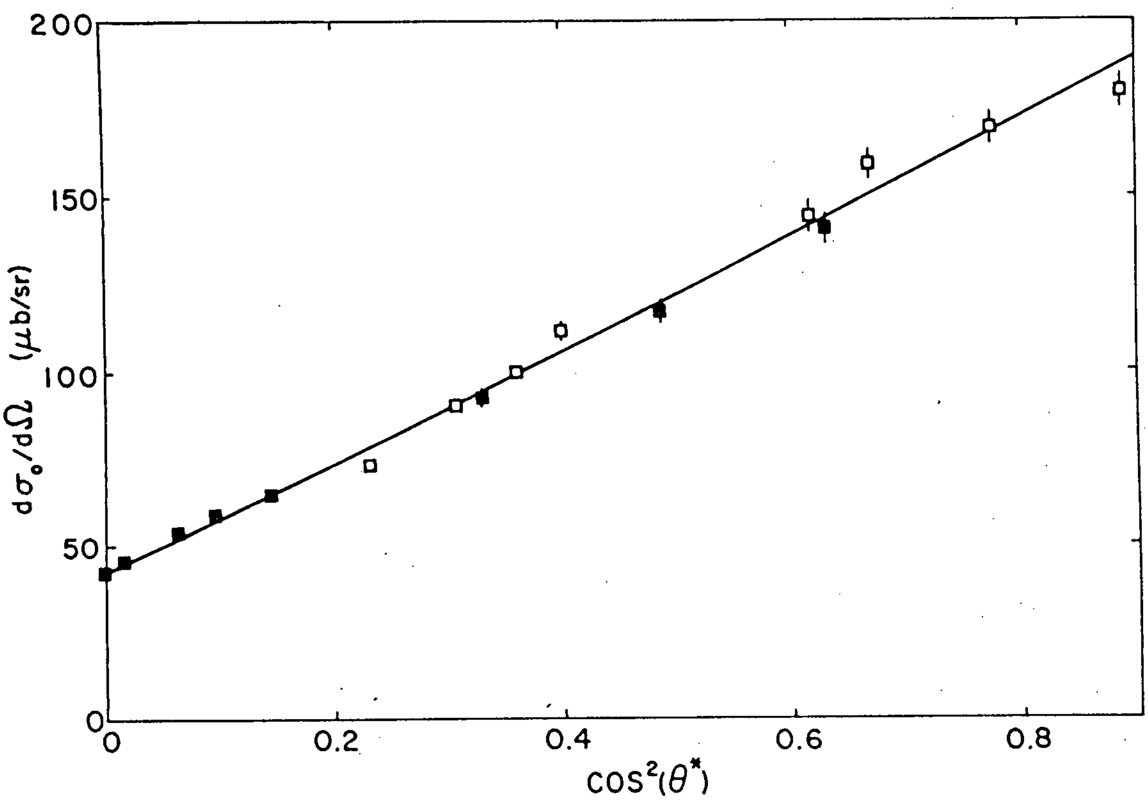

The differential cross-sections shown here are obtained from data collected with an unpolarized incident proton beam. Solid points indicate results deduced from measurements with the backward pion detection arm. The line represents the results of a fit of a fourth order Legendre polynomial to these results.

Figure (4.23)

The 450 MeV. Differential Cross-Sections.

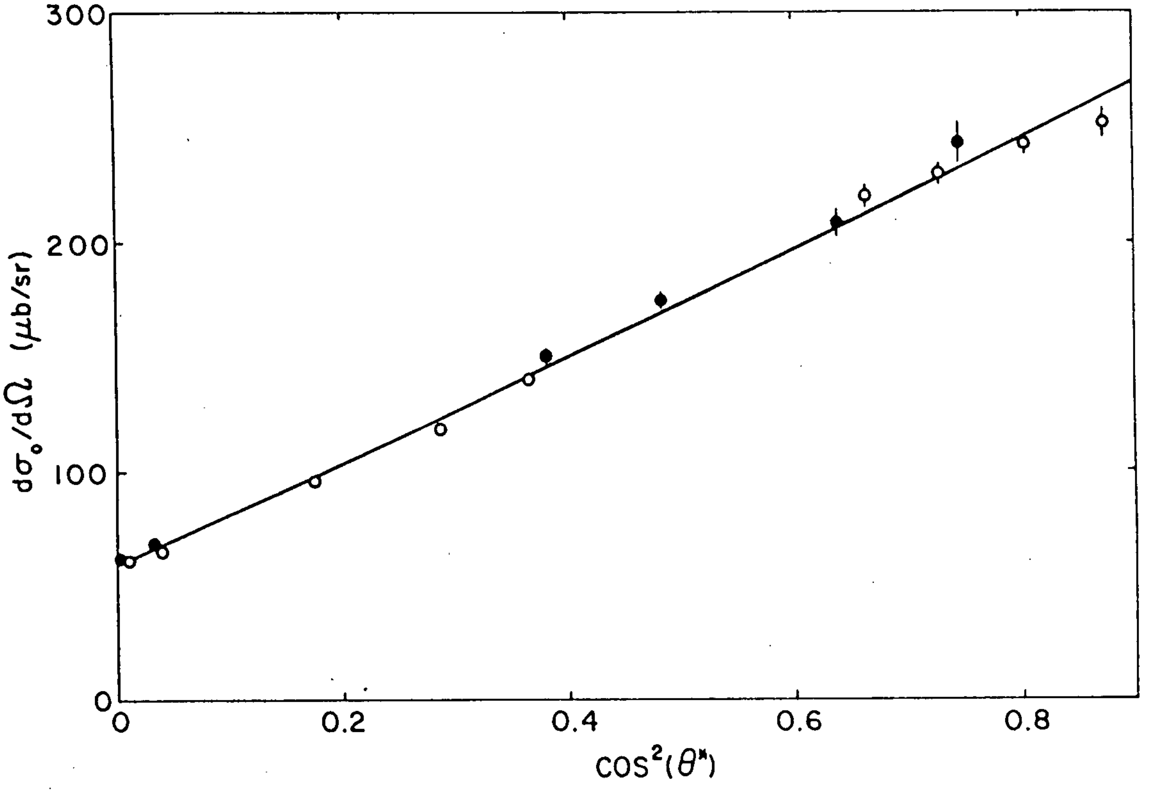

The differential cross-sections shown here are obtained from data collected with a polarized incident proton beam. Solid points indicate results deduced from measurements with the backward pion detection arm. The line represents the results of a fit of a fourth order Legendre polynomial to these results.

Figure (4.24)

The 475 MeV. Differential Cross-Sections.

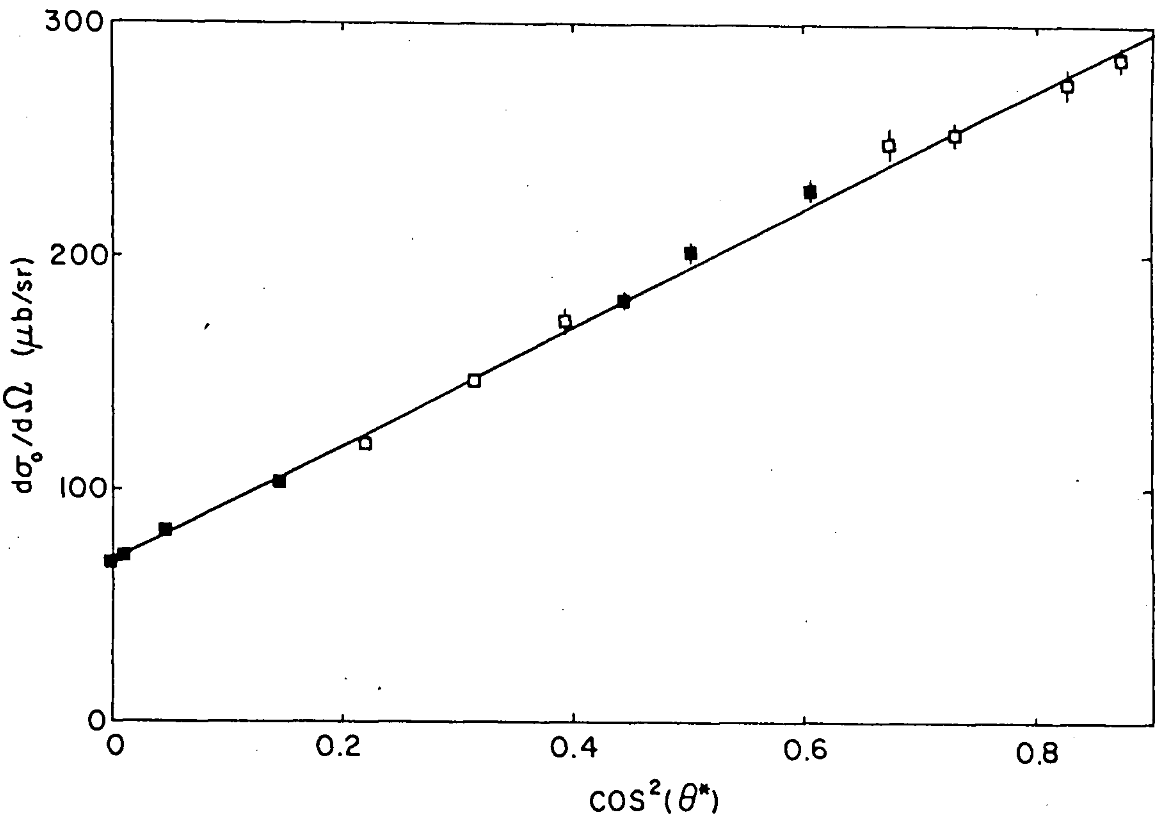

The differential cross-sections shown here are obtained from data collected with an unpolarized incident proton beam. Solid points indicate results deduced from measurements with the backward pion detection arm. The line represents the results of a fit of a fourth order Legendre polynomial to these results.

Figure (4.25)

The 498 MeV. Differential Cross-Sections.

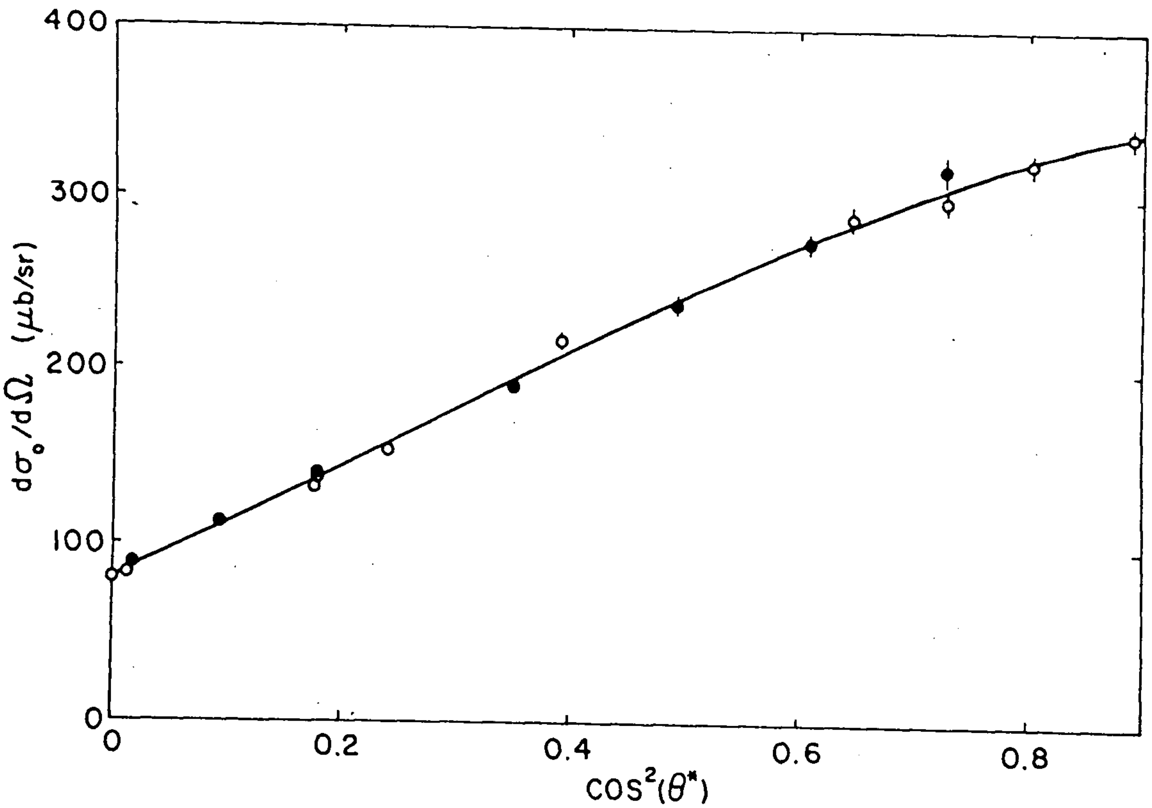

The differential cross-sections shown here are obtained from data collected with a polarized incident proton beam. Solid points indicate results deduced from measurements with the backward pion detection arm. The line represents the results of a fit of a fourth order Legendre polynomial to these results.

tables (4.5),(4.6),(4.7), and (4.9) respectively.

4.7.1.1 The Uncertainty of the Differential Cross-Sections: Unpolarized Beam

The uncertainty of the differential cross-sections contains both random and systematic contributions. Random quantities are expected to vary randomly about a mean value on a run to run basis. Systematic errors, however, have a uniform effect on all results. These effects are discussed in detail in section (4.9).

The uncertainty of the differential cross-section as a result of random fluctuations of the independent variables displayed by equation (60) above, is given by;

$$\{ \Delta[d\sigma/d\Omega] \}^2 = (\zeta/\Delta\Omega^{\dagger})^2 \{ [\Delta(\Delta\Omega^{\dagger})/\Delta\Omega^{\dagger}]^2 + (\Delta\zeta/\zeta)^2 \} + \{ \tfrac{1}{2}\Delta[d\sigma_c/d\Omega] \}^2 \tag{62}$$

where the uncertainty of the quantity ζ, $\Delta\zeta$, is;

$$\Delta\zeta^2 = \zeta^2 \{ (N_p + N_r)/(N_p - N_r)^2 + (\Delta N_{int}/N_{int})^2 + (\Delta\epsilon/\epsilon)^2 \} \tag{63}$$

A significant simplification with an insignificant loss of precision is achieved by approximating the leading factor of the above equation by the differential cross-section, that is;

$$\zeta/\Delta\Omega^{\dagger} \cong d\sigma/d\Omega \tag{64}$$

Then, the random uncertainty of the differential

Table (4.5)

The 350 MeV. Differential Cross-Sections.

Pion Angle		Differential Cross-Sections		Analyzing Powers
θ^*_π (degrees)	$\mathrm{Cos}^2(\theta^*_\pi)$	$d\sigma_0/d\Omega$ (μb/sr.)	$d\sigma_1/d\Omega$ (μb/sr.)	A_{no}
90.5	0.000	15.7(0.5)	-	-
90.6	0.000	15.9(0.4)	-	-
103.5	0.054	19.2(0.5)	-	-
108.9	0.105	20.7(0.7)	-	-
110.2	0.119	22.0(0.7)	-	-
63.3	0.202	25.4(0.6)	-	-
58.2	0.278	28.3(0.7)	-	-
56.5	0.305	30.4(0.7)	-	-
53.2	0.359	33.2(1.0)	-	-
128.9	0.394	34.1(1.2)	-	-
131.0	0.430	35.8(1.2)	-	-
134.9	0.498	40.3(1.4)	-	-
40.2	0.583	42.5(1.3)	-	-
35.1	0.669	48.3(1.0)	-	-
33.3	0.699	49.8(1.1)	-	-

Table (4.6)

The 375 MeV. Polarized and Unpolarized Differential Cross-Section and Analyzing Powers.

Pion Angle		Differential Cross-Sections		Analyzing Powers
θ^*_π (degrees)	$\mathrm{Cos}^2(\theta^*_\pi)$	$d\sigma_0/d\Omega$ (μb/sr.)	$d\sigma_1/d\Omega$ (μb/sr.)	A_{no}
89.9	0.000	23.7(0.7)	-	-
90.0	0.000	23.6(0.6)	-	-
100.8	0.035	27.4(0.7)	-	-
106.6	0.082	28.7(1.0)	-	-
115.3	0.183	38.3(1.2)	-	-
62.7	0.210	40.8(0.9)	-	-
58.0	0.281	43.9(1.3)	-	-
51.8	0.382	59.1(1.4)	-	-
128.8	0.393	56.2(1.9)	-	-
135.2	0.503	62.8(2.1)	-	-
135.9	0.516	63.9(2.2)	-	-
37.7	0.626	79.8(2.1)	-	-
35.9	0.656	79.6(2.3)	-	-
34.1	0.686	81.0(2.3)	-	-
28.4	0.774	87.3(2.3)	-	-
28.8	0.768	88.7(2.6)	-	-
91.4	0.001	23.7(0.6)	-11.5(0.3)	-0.48(.01)
84.2	0.010	23.0(0.6)	-10.8(0.3)	-0.47(.01)
95.5	0.009	24.6(0.7)	-11.8(0.4)	-0.48(.01)
78.3	0.041	25.3(0.7)	-9.9(0.3)	-0.39(.01)
113.0	0.153	36.8(1.3)	-9.4(0.8)	-0.26(.02)
59.5	0.258	44.1(1.0)	-6.0(0.5)	-0.14(.01)
121.8	0.278	45.4(1.4)	-8.2(0.5)	-0.18(.01)
52.9	0.364	56.7(1.2)	-3.6(0.5)	-0.06(.01)
132.5	0.456	60.2(2.0)	-6.0(0.6)	-0.10(.01)
36.4	0.648	81.5(2.0)	1.7(0.8)	0.02(.01)
146.1	0.689	83.7(3.0)	-2.6(0.8)	-0.03(.01)
25.1	0.820	88.4(1.9)	3.2(0.7)	0.04(.01)

Table (4.7)

The 425 MeV. Differential Cross-Sections.

Pion Angle		Differential Cross-Sections		Analyzing Powers
θ_π^* (degrees)	$\mathrm{Cos}^2(\theta_\pi^*)$	$d\sigma_0/d\Omega$ (μb/sr.)	$d\sigma_1/d\Omega$ (μb/sr.)	A_{no}
89.7	0.000	42.1(1.2)	-	-
89.8	0.000	42.2(1.2)	-	-
97.5	0.017	45.1(1.2)	-	-
104.7	0.064	53.5(1.3)	-	-
108.1	0.097	58.7(1.5)	-	-
112.5	0.146	64.5(1.6)	-	-
61.2	0.232	73.0(2.1)	-	-
56.3	0.308	90.6(2.0)	-	-
125.1	0.331	92.7(2.9)	-	-
53.1	0.361	99.9(2.2)	-	-
50.7	0.401	111.8(2.7)	-	-
134.3	0.488	117.2(3.6)	-	-
38.1	0.619	144.0(4.9)	-	-
142.7	0.633	140.5(4.3)	-	-
35.0	0.671	158.6(4.5)	-	-
28.1	0.778	168.7(4.8)	-	-
19.4	0.890	178.9(5.2)	-	-

Table (4.8)

The 450 MeV. Polarized and Unpolarized Differential Cross-Section Terms and Analyzing Powers.

Pion Angle		Differential Cross-Sections		Analyzing Powers
θ_π^* (degrees)	$\cos^2(\theta_\pi^*)$	$d\sigma_0/d\Omega$ (μb/sr.)	$d\sigma_1/d\Omega$ (μb/sr.)	A_{no}
93.1	0.003	62.1(1.7)	-15.7(0.8)	-0.25(.01)
83.9	0.011	61.1(1.7)	-12.6(0.7)	-0.21(.01)
100.4	0.033	68.7(1.8)	-13.7(0.7)	-0.20(.01)
78.4	0.040	64.8(1.7)	-10.6(0.8)	-0.16(.01)
100.4	0.033	68.8(1.8)	-14.0(0.9)	-0.20(.01)
65.3	0.175	96.0(2.2)	0.9(0.9)	0.01(.01)
57.6	0.287	118.7(2.6)	7.7(1 1)	0.07(.01)
52.8	0.366	139.8(3.0)	17.4(1.3)	0.12(.01)
128.2	0.382	149.8(3.5)	2.3(1.8)	0.02(.01)
134.1	0.484	174.1(4.0)	8.3(2.1)	0.05(.01)
143.2	0.641	208.1(6.2)	17.7(2.0)	0.09(.01)
35.3	0.666	219.3(5.2)	31.5(2.0)	0.14(.01)
31.3	0.730	228.7(4.8)	32.3(2.3)	0.14(.01)
149.9	0.748	242.8(9.3)	22.3(2.9)	0.09(.01)
26.1	0.806	241.9(4.8)	28.7(1.9)	0.12(.01)
20.7	0.875	251.4(6.5)	20.6(2.8)	0.08(.01)

Table (4.9)

The 475 MeV. Differential Cross-Sections.

Pion Angle		Differential Cross-Sections		Analyzing Powers
θ^*_π (degrees)	$\text{Cos}^2(\theta^*_\pi)$	$d\sigma_0/d\Omega$ (μb/sr.)	$d\sigma_1/d\Omega$ (μb/sr.)	A_{no}
90.1	0.000	68.6(2.0)	-	-
90.3	0.000	68.6(2.0)	-	-
95.3	0.009	71.6(2.0)	-	-
102.4	0.046	82.2(2.2)	-	-
112.3	0.144	103.4(2.6)	-	-
62.1	0.219	120.4(2.8)	-	-
55.9	0.314	147.0(3.3)	-	-
51.2	0.393	173.0(6.1)	-	-
131.8	0.444	181.7(4.2)	-	-
135.1	0.502	202.4(4.7)	-	-
141.1	0.606	228.8(5.1)	-	-
34.8	0.674	248.5(7.1)	-	-
31.3	0.730	252.5(5.2)	-	-
24.6	0.827	274.9(7.1)	-	-
20.9	0.873	286.1(5.8)	-	-

Table (4.10)

The 498 MeV. Polarized and Unpolarized Differential Cross-Section Terms and Analyzing Powers.

Pion Angle		Differential Cross-Sections		Analyzing Powers
θ^*_π (degrees)	$\cos^2(\theta^*_\pi)$	$d\sigma_0/d\Omega$ (μb/sr.)	$d\sigma_1/d\Omega$ (μb/sr.)	A_{no}
90.0	0.000	80.8(2.2)	-3.8(0.6)	-0.05(.01)
83.5	0.013	83.5(2.3)	-0.8(0.6)	-0.01(.01)
97.5	0.017	89.6(2.3)	-1.8(0.7)	-0.02(.01)
107.8	0.093	113.2(2.8)	3.7(1.3)	0.03(.01)
65.1	0.177	132.6(3.1)	20.8(1.3)	0.16(.01)
115.0	0.179	141.1(3.3)	14.1(1.4)	0.10(.01)
115.1	0.180	138.3(3.2)	14.6(1.6)	0.11(.01)
60.6	0.241	154.3(3.4)	29.9(1.4)	0.19(.01)
126.4	0.352	190.9(4.3)	27.9(2.3)	0.15(.01)
51.2	0.393	216.5(4.5)	51.0(2.1)	0.24(.01)
134.7	0.495	237.9(5.5)	45.2(3.3)	0.19(.01)
141.4	0.611	273.8(6.0)	42.4(2.6)	0.16(.01)
36.4	0.648	289.0(8.2)	67.4(3.4)	0.23(.01)
148.6	0.729	316.8(9.1)	47.8(3.3)	0.15(.01)
31.3	0.730	299.1(6.1)	67.9(3.0)	0.23(.01)
26.2	0.805	320.9(6.5)	67.5(3.5)	0.21(.01)
19.2	0.892	338.2(6.6)	55.4(2.5)	0.16(.01)

cross-section is given by;

$$\{\ \Delta[d\sigma/d\Omega]\ \}^2 = (\ d\sigma/d\Omega\ )^2\ \{\ [\ \Delta(\Delta\Omega^\dagger)/\Delta\Omega^\dagger\ ]^2 + (\ \Delta\zeta/\zeta\ )^2\ \} + \{\ \tfrac{1}{2}\Delta[d\sigma_c/d\Omega]\ \}^2 \qquad (65)$$

4.7.2 THE DIFFERENTIAL CROSS-SECTIONS: POLARIZED BEAM

The unpolarized differential cross-section is evaluated according to the equation:

$$d\sigma_0/d\Omega = \tfrac{1}{2}(\ d\sigma\uparrow/d\Omega + d\sigma\downarrow/d\Omega\ ) - \tfrac{1}{2}(\ d\sigma\uparrow/d\Omega - d\sigma\downarrow/d\Omega)\ P \qquad (66)$$

where:

$$P = (\ P\uparrow - P\downarrow\ )/(\ P\uparrow + P\downarrow\ )$$

$\uparrow$ - Indicates a quantity measured with the spin (direction) up.

$\downarrow$ - Indicates a quantity measured with the spin (direction) down.

$P\uparrow, P\downarrow$ - The magnitude (a positve quantity) of the beam polarizations.

Substituting the spin dependent values of the experimentally determined quantities into the above differential cross-section expression yields;

$$d\sigma_0/d\Omega = \tfrac{1}{2}(\ \zeta\uparrow + \zeta\downarrow\ )/\Delta\Omega^{\dagger} - \{\ \tfrac{1}{2}(\ \zeta\uparrow - \zeta\downarrow\ )/\Delta\Omega^{\dagger}\ \}\ P$$

$$- \tfrac{1}{2}\{\ \tfrac{1}{2}(\ d\sigma_C\uparrow/d\Omega + d\sigma_C\downarrow/d\Omega\ )$$

$$- \tfrac{1}{2}(\ d\sigma_C\uparrow/d\Omega - d\sigma_C\downarrow/d\Omega\ )\ P\ \} \tag{67}$$

The differential cross-sections are evaluated for the three data sets associated with the incident polarized beam energies: 375, 450 and 498 MeV, and are shown in figures (4.21),(4.23), and (4.25) respectively. The line indicated on the plots represent the results of a fit of Legendre polynomials to the data. The associated numeric values are tabulated in tables (4.6), (4.8), and (4.10). The following values were used for the polarimeter analysing power: 0.409 at 375 MeV, 0.422 at 450 MeV, and 0.432 at 498 MeV. See section (4.9) for a discussion of this quantity.

4.7.2.1 The Uncertainty of the Differential Cross-Section: Polarized Beam

As a basis for error calculations, equation (67) was simplified using the following assumptions:

1) The magnitude of the spin up and spin down polarizations are approximately equal, then;

$$(\ P\uparrow - P\downarrow\ )/(\ P\uparrow + P\downarrow\ ) = P \cong 0 \tag{68}$$

2) The spin averaged value of the carbon background differential cross-section is approximately its unpolarized

value, that is;

$$d\sigma_c/d\Omega \cong \tfrac{1}{2}(\ d\sigma_c\uparrow/d\Omega + d\sigma_c\downarrow/d\Omega\ ) \tag{69}$$

Then the differential cross-section expression is approximated by;

$$d\sigma_0/d\Omega = \tfrac{1}{2}(\ \zeta\uparrow + \zeta\downarrow\ )/\Delta\Omega^\dagger - \tfrac{1}{2}d\sigma_c/d\Omega \tag{70}$$

It follows that the uncertainty of the differential cross-section is then given by;

$$\begin{aligned} \{\ \Delta[d\sigma_0/d\Omega]\ \}^2 &= \{\ \tfrac{1}{2}(\ \zeta\uparrow + \zeta\downarrow\ )/\Delta\Omega^\dagger\ \}^2 \\ &\quad \{[\Delta(\Delta\Omega^\dagger)/\Delta\Omega^\dagger]^2 + (\ \Delta\zeta\uparrow^2 + \Delta\zeta\downarrow^2)/(\ \zeta\uparrow + \zeta\downarrow\ )^2\} \\ &\quad + \{\ \tfrac{1}{2}\Delta[d\sigma_c/d\Omega]\ \}^2 \end{aligned} \tag{71}$$

A Further simplification is obtained using the approximation

$$\tfrac{1}{2}(\ \zeta\uparrow + \zeta\downarrow\ )\ /\ \Delta\Omega^\dagger \cong d\sigma_0/d\Omega \tag{72}$$

Finally, the uncertainty of the differential cross-section due to random fluctuations of the independent quantities on which it depends, is;

$$\begin{aligned} \{\Delta[d\sigma_0/d\Omega]\}^2 &= \{\ d\sigma_0/d\Omega\ \}^2 \\ &\quad \{[\ \Delta(\Delta\Omega^\dagger)/\Delta\Omega^\dagger]^2\ (\ \Delta\zeta\uparrow^2 + \Delta\zeta\downarrow^2\ )/(\ \zeta\uparrow + \zeta\downarrow\ )^2\} \\ &\quad + \{\ \tfrac{1}{2}\Delta[d\sigma_c/d\Omega]\ \}^2 \end{aligned} \tag{73}$$

4.7.3 THE POLARIZED DIFFERENTIAL CROSS-SECTION

The polarized differential cross-sections are calculated according to the expression,

$$d\sigma_1/d\Omega = (d\sigma\uparrow/d\Omega - d\sigma\downarrow/d\Omega)/(P\uparrow + P\downarrow) \tag{74}$$

Upon substitution of the spin dependent measured quantities, the expression is:

$$d\sigma_1/d\Omega = [(\zeta\uparrow - \zeta\downarrow)/\Delta\Omega^{\dagger}] / (P\uparrow + P\downarrow) - \tfrac{1}{2}\{ (d\sigma_c\uparrow/d\Omega - d\sigma_c\downarrow/d\Omega) \} / (P\uparrow + P\downarrow) \tag{75}$$

The polarized portion of the differential cross-sections are evaluated for the three data sets associated with the unpolarized incident beam energies of; 375, 450,and 498 MeV, and are shown in figures (4.26),(4.27), and (4.28). The lines indicated on the plots represent the results of a fit of Associated Legendre polynomials to the data. Additionally, the numerical results are tabulated in tables (4.6),(4.8), and (4.10). The following values were used for the polarimeter analysing power: 0.409 at 375 MeV, 0.422 at 450 MeV, and 0.432 at 498 MeV. See section (4.9) for a discussion of this quantity.

4.7.3.1 The Uncertainty of the Polarized Differential Cross-Section

As a basis for calculation of the random uncertainties, equation (75) can be approximated by assuming that the

Figure (4.26)

The 375 MeV. Differential Cross-Section Polarized Term.

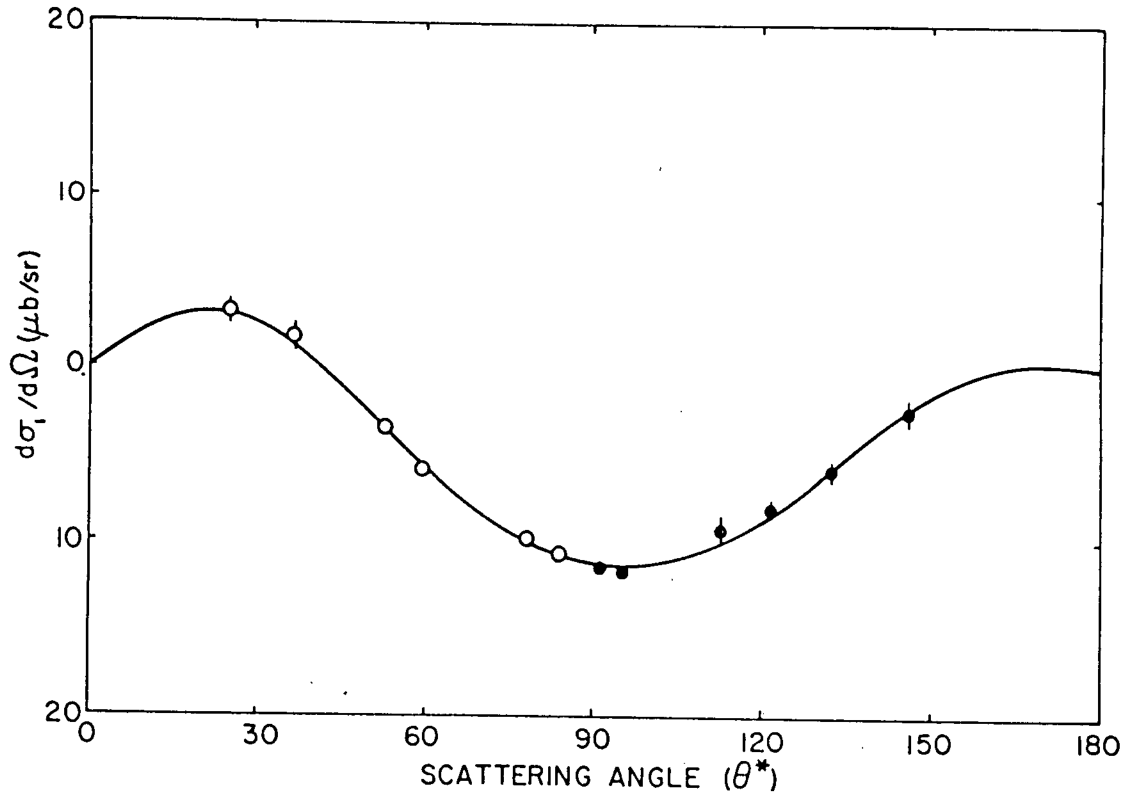

Solid points indicate results deduced from measured with the backward pion detection arm. The line represents the results of a fit of a fifth order Associated Legendre polynomial to these results .

Figure (4.27)

The 450 MeV. Differential Cross-Sections: Polarized Term.

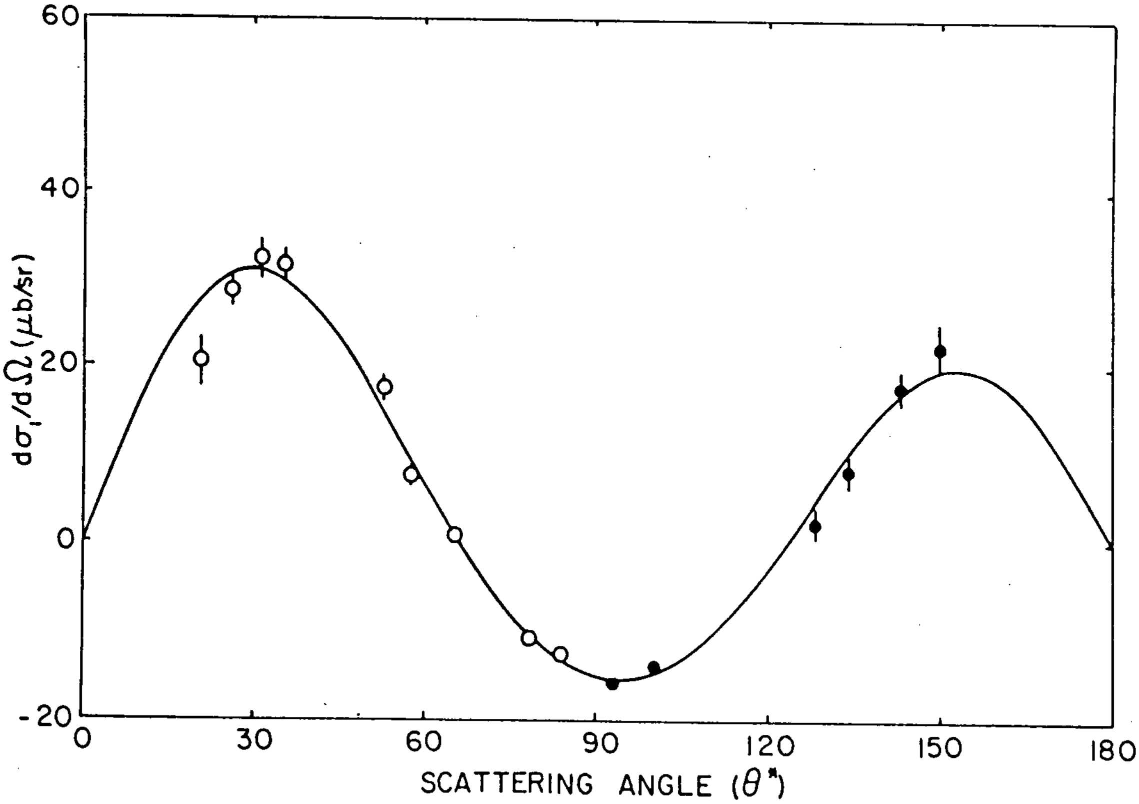

Solid points indicate results deduced from measured with the backward pion detection arm. The line represents the results of a fit of a fifth order Associated Legendre polynomial to these results .

Figure (4.28)

The 498 MeV. Differential Cross-Sections: Polarized Term.

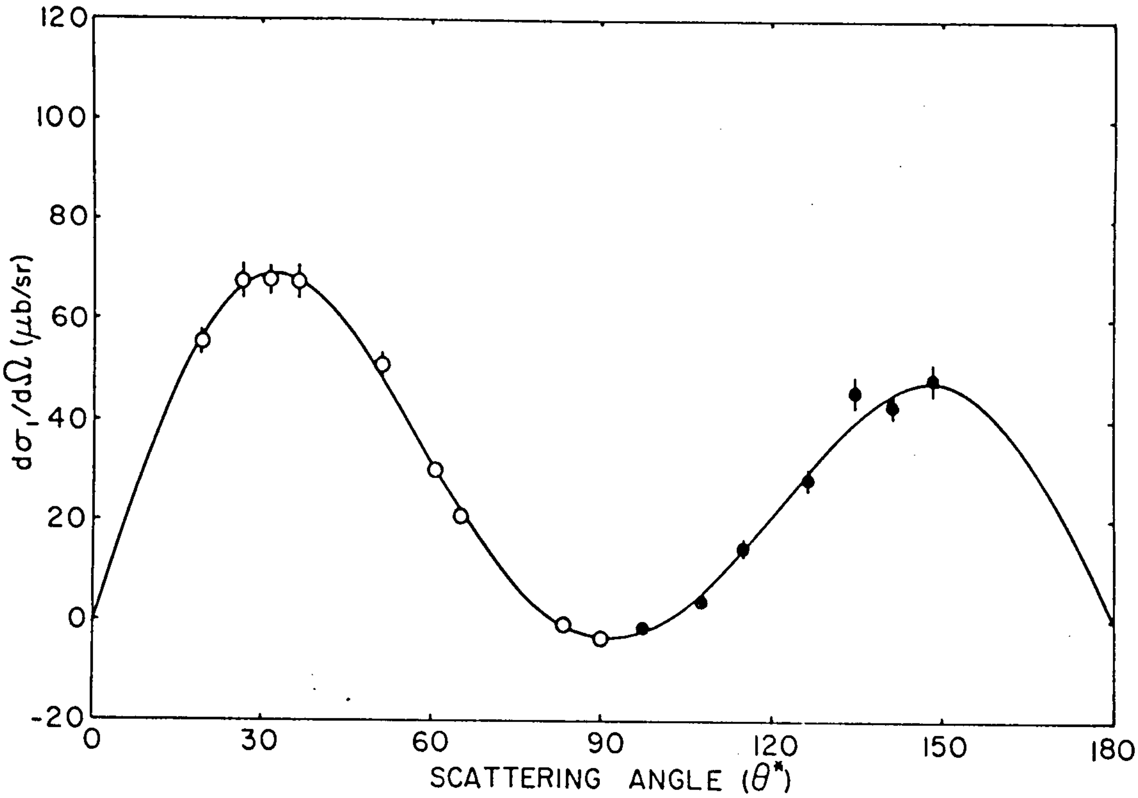

Solid points indicate results deduced from measured with the backward pion detection arm. The line represents the results of a fit of a fifth order Associated Legendre polynomial to these results .

contribution of the carbon background term to the overall uncertainty is insignificant. That is the following term, and its associated contribution towards the uncertainty can be neglected;

$$\tfrac{1}{2}\{ (d\sigma_C\uparrow/d\Omega - d\sigma_C\downarrow/d\Omega) \} / (P\uparrow + P\downarrow) \cong 0 \quad (76)$$

thus;

$$d\sigma_1/d\Omega \cong [(\zeta\uparrow - \zeta\downarrow)/\Delta\Omega^\dagger] / (P\uparrow + P\downarrow) \quad (77)$$

Then, on the basis of this approximation of the differential cross-section, the associated uncertainty becomes;

$$\{ \Delta[d\sigma_1/d\Omega] \}^2 = \{[(\zeta\uparrow - \zeta\downarrow)/\Delta\Omega^\dagger]/(P\uparrow + P\downarrow)\}^2$$

$$\{[\Delta(\Delta\Omega^\dagger)/\Delta\Omega^\dagger]^2 + (\Delta\zeta\uparrow^2 + \Delta\zeta\downarrow^2)/(\zeta\uparrow - \zeta\downarrow)^2$$

$$+ (\Delta P\uparrow^2 + \Delta P\downarrow^2)/(P\uparrow + P\downarrow)^2 \} \quad (78)$$

Approximating the leading factor by the polarized differential cross-section leads to the following expression for the uncertainty in the polarized differential cross-section.

$$\{ \Delta[d\sigma_1/d\Omega] \}^2 = \{ d\sigma_1/d\Omega \}^2$$

$$\{[\Delta(\Delta\Omega^\dagger)/\Delta\Omega^\dagger]^2 + (\Delta\zeta\uparrow^2 + \Delta\zeta\downarrow^2)/(\zeta\uparrow - \zeta\downarrow)^2$$

$$+ (\Delta P\uparrow^2 + \Delta P\downarrow^2)/(P\uparrow + P\downarrow)^2 \} \quad (79)$$

4.7.4 THE ANALYZING POWER

The analyzing power is simply the ratio of the polarized differential cross-section to the unpolarized differential crosssection, that is;

$$A_{no} = (d\sigma_1/d\Omega)/(d\sigma_0/d\Omega) \qquad (80)$$

The analyzing powers of the 375 MeV, 450 MeV, and 498 MeV data are shown in figure (4.29), figure (4.30), and figure (4.31) respectively. The data can also be found alphanumerically encoded into tables (4.6),(4.8), and (4.10). The following values were used for the polarimeter analysing power: 0.409 at 375 MeV, 0.422 at 450 MeV, and 0.432 at 498 MeV. See section (4.9) for a discussion of this quantity.

4.7.4.1 The Uncertainty of the Analyzing power.

As the basis of the analysis of uncertainties, the analyzing powers can be approximated in the following form;

$$A_{no} \cong \{ (\zeta\uparrow - \zeta\downarrow) / (\zeta\uparrow + \zeta\downarrow) \}$$

$$\{ 2 / (P\uparrow + P\downarrow) \}$$

$$\{ 1 + \tfrac{1}{2}[d\sigma_c/d\Omega]/[d\sigma/d\Omega] + \ldots \} \qquad (81)$$

Which results (with some manipulation) from the ratio (of right hand sides) of equations (77) to (70). The leading term of the denominator has been factored out and the denominator expanded (the final factor in the above expression) such that the solid angles cancel out of the

Figure (4.29)

The 375 MeV. Analyzing Powers.

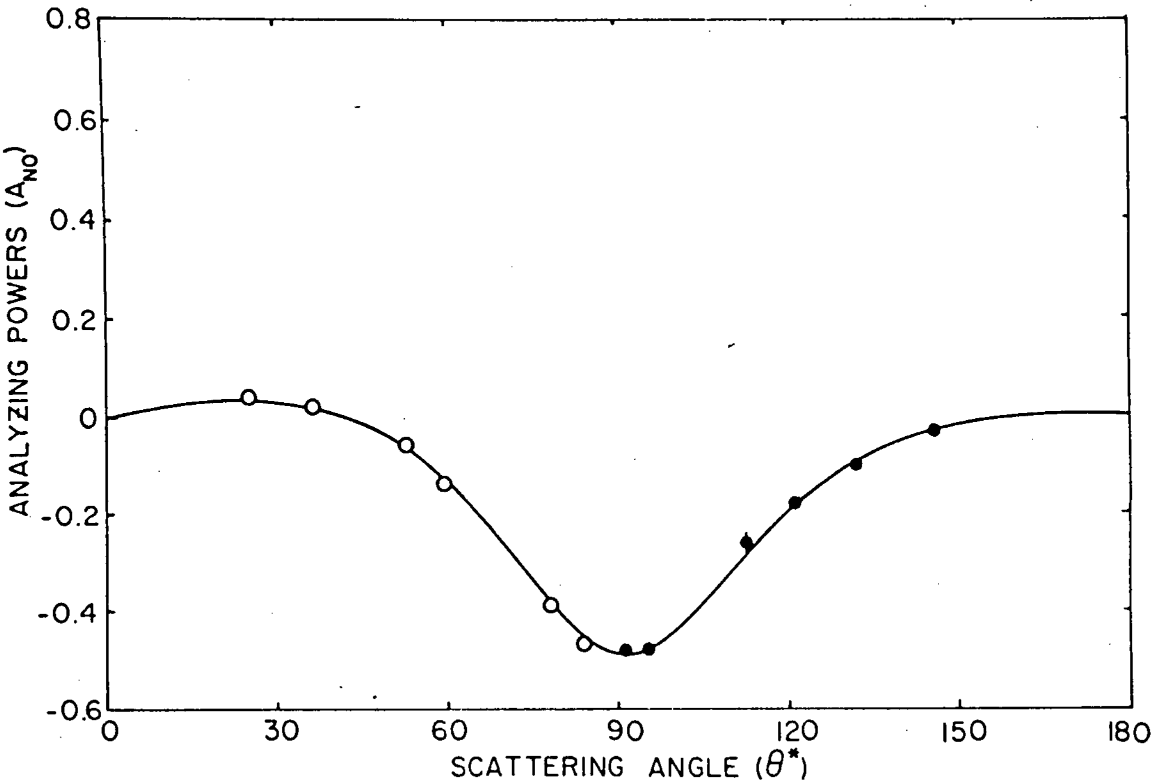

Solid points indicate results deduced from measured with the backward pion detection arm. The line represents the analysing power deduced from the fits to the unpolarized and polarized differential cross-sections .

Figure (4.30)

The 450 MeV. Analyzing Powers.

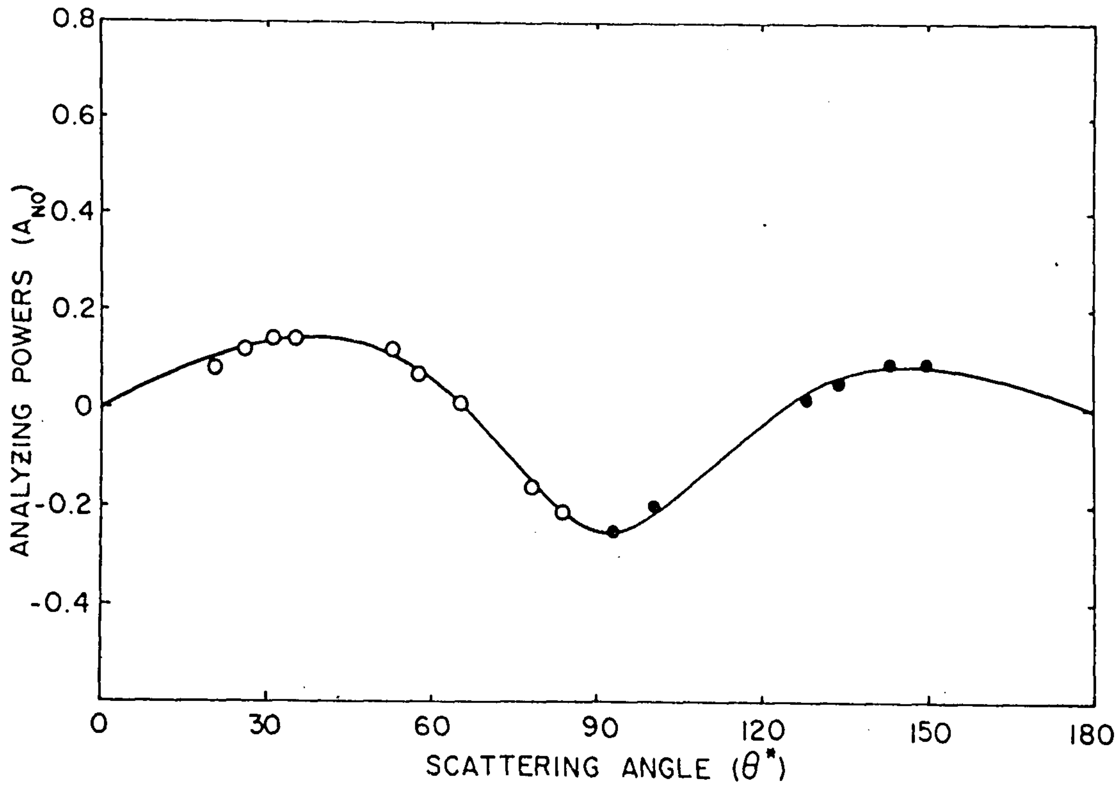

Solid points indicate results deduced from measured with the backward pion detection arm. The line represents the analysing power deduced from the fits to the unpolarized and polarized differential cross-sections .

Figure (4.31)

The 498 MeV. Analyzing Powers.

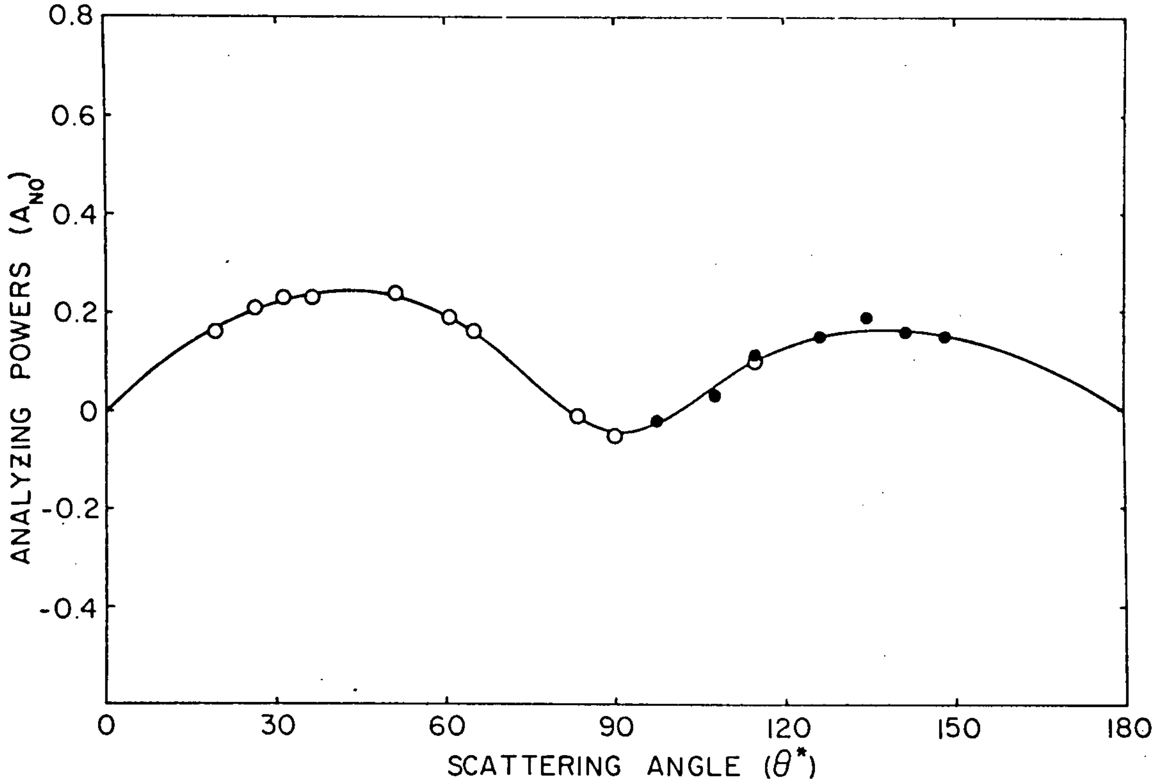

Solid points indicate results deduced from measured with the backward pion detection arm. The line represents the analysing power deduced from the fits to the unpolarized and polarized differential cross-sections .

ratio. The term representing the denominator is then approximated by unity since the relative carbon background contribution is taken to be insignificant and the analyzing power is approximated by;

$$A_{no} \cong \{ (\zeta\uparrow - \zeta\downarrow) / (\zeta\uparrow + \zeta\downarrow) \}$$
$$\{ 2 / (P\uparrow + P\downarrow) \}$$
$$\{ 1 \} \tag{82}$$

The uncertainty (random) of the analyzing powers is then given by;

$$(\Delta A_{no})^2 \cong A_{no}^2 \{ (\Delta\zeta\uparrow^2 + \Delta\zeta\downarrow^2) / (\zeta\uparrow - \zeta\downarrow)^2$$
$$\{ (\Delta\zeta\uparrow^2 + \Delta\zeta\downarrow^2) / (\zeta\uparrow + \zeta\downarrow)^2$$
$$\{ (\Delta P\uparrow^2 + \Delta P\downarrow^2) / (P\uparrow + P\downarrow)^2 \} \tag{83}$$

4.8 ANALYZING POWERS: KINEMATIC EVENT DEFINITION

The analyzing powers of the $pp \rightarrow \pi^+ d$ reaction were derived from the polarized beam data utilizing the kinematic correlation of the final state particles as a constraint to reduce the relative background level to the point where a background subtraction was unnecessary.

The results, which are published (Giles et al.[9]), are reproduced in Appendix (3). The numerical values of the analyzing powers were not published, thus, they are tabulated here in Tables (4.11),(4.12), and (4.13).

Table (4.11)

The 375 MeV. Analyzing Powers.

Pion Angle θ^*_π (degrees)	Analyzing Powers / Target Material		
	Polyethylene CH_2	Carbon C	$pp \rightarrow \pi^+ d$ (Hydrogen)
25.4	0.036±0.006	-0.001±0.001	0.035±0.006
37.7	0.016±0.006	-0.001±0.001	0.015±0.006
53.1	-0.064±0.005	-0.001±0.001	-0.065±0.005
59.7	-0.115±0.005	-0.002±0.002	-0.117±0.005
66.2	-0.195±0.008	-0.004±0.002	-0.199±0.008
78.5	-0.355±0.007	-0.006±0.002	-0.361±0.007
84.4	-0.438±0.007	-0.011±0.002	-0.449±0.007
91.5	-0.472±0.007	-0.017±0.002	-0.489±0.007
95.6	-0.466±0.008	-0.015±0.002	-0.481±0.008
99.6	-0.428±0.009	-0.013±0.002	-0.441±0.009
104.7	-0.375±0.007	-0.010±0.002	-0.385±0.007
113.1	-0.268±0.008	-0.006±0.002	-0.274±0.008
121.9	-0.165±0.008	-0.006±0.005	-0.171±0.009
132.6	-0.097±0.007	-0.005±0.005	-0.102±0.009
146.1	-0.032±0.006	-0.005±0.005	-0.037±0.008

Table (4.12)

The 450 MeV. Analyzing Powers.

Pion Angle θ^*_π (degrees)	Analyzing Powers		
	Target Material		
	Polyethylene CH_2	Carbon C	$pp \rightarrow \pi^+ d$ (Hydrogen)
19.4	0.077±0.006	0.0±0.0	0.077±0.006
26.4	0.120±0.005	0.0±0.0	0.120±0.005
31.6	0.132±0.008	0.0±0.0	0.132±0.008
36.6	0.141±0.006	0.0±0.0	0.141±0.006
53.1	0.122±0.006	0.001±0.001	0.123±0.006
57.8	0.070±0.005	0.001±0.001	0.071±0.005
65.5	0.003±0.007	0.001±0.001	0.004±0.007
78.6	-0.159±0.008	0.0±0.001	-0.159±0.008
84.0	-0.208±0.008	0.0±0.001	-0.208±0.008
93.2	-0.254±0.008	0.001±0.001	-0.253±0.008
100.5	-0.195±0.006	0.001±0.001	-0.194±0.006
107.4	-0.131±0.006	0.0±0.001	-0.131±0.006
128.2	0.031±0.010	-0.001±0.001	0.030±0.010
134.1	0.057±0.009	-0.0±0.001	0.057±0.009
143.2	0.077±0.007	0.0±0.001	0.077±0.007
150.5	0.087±0.006	0.001±0.001	0.088±0.006

Table (4.13)

The 498 MeV. Analyzing Powers.

Pion Angle θ^*_π (degrees)	Analyzing Powers — Target Material		
	Polyethylene CH_2	Carbon C	$pp \rightarrow \pi^+ d$ (Hydrogen)
19.5	0.162±0.004	0.0±0.0	0.162±0.004
26.4	0.206±0.008	0.0±0.001	0.206±0.008
31.6	0.229±0.007	0.0±0.001	0.229±0.007
36.7	0.240±0.006	0.0±0.001	0.240±0.006
51.5	0.232±0.006	0.0±0.001	0.232±0.006
60.8	0.192±0.006	0.0±0.001	0.192±0.006
65.4	0.159±0.006	0.001±0.001	0.160±0.006
78.3	0.036±0.008	0.001±0.001	0.037±0.008
83.7	-0.008±0.005	0.001±0.001	-0.007±0.005
90.2	-0.047±0.005	0.001±0.001	-0.046±0.005
97.6	-0.023±0.005	0.002±0.001	-0.021±0.005
107.8	0.043±0.007	0.002±0.001	0.045±0.007
115.1	0.105±0.008	0.002±0.001	0.107±0.008
120.0	0.154±0.009	0.002±0.001	0.156±0.009
126.4	0.153±0.009	0.002±0.001	0.155±0.009
134.7	0.184±0.006	0.001±0.001	0.185±0.006
141.5	0.163±0.006	0.001±0.001	0.164±0.006
149.6	0.156±0.005	0.001±0.001	0.157±0.005

Differential cross-section results could not be obtained with this technique, as the kinematic constraints used to elimimate the background also eliminated from the data set, an unknown fraction of $pp \rightarrow \pi^+ d$ events (in particular, of those events for which the pion decayed and the subsequent muon was detected). Thus, for the differential cross-sections, a background subtraction technique as described in section (4.3) had to be employed.

4.9 DISCUSSION OF UNCERTAINTIES

Systematic uncertainties and uncertainties other than those associated with counting statistics or otherwise randomly distributed sources are discussed in this section.

There is an overall uncertainty of 1.8% in the absolute values of the differential cross-sections due to the uncertainty of the effective solid angle of the $pp \rightarrow pp$ elastic beam current monitor. This uncertainty is the same as that described in our published $pp \rightarrow pp$ differential cross-section results. It, of course, cancels out when the ratio of the pion production to $pp \rightarrow pp$ differential cross-sections (at 90°cm) is considered. It also cancels out when considering the a_i^{oo}/a_0^{oo} or b_i^{no}/a_0^{oo} ratios that define the angular shapes of the unpolarized and polarized differential cross-sections respectively.

Additionally, there is an uncertainty of ±1 MeV associated with the incident proton energy.

The analyzing powers and polarized differential cross-sections are subject to a systematic uncertainty that is associated with the polarization of the incident proton beam. This uncertainty, estimated at 5 percent, arises as a result of calibration (uncertainties) of the beam energy dependent analyzing power (A_p) of the beam-line polarimeter. If calibrations to higher precision are ever attained, the systematic uncertainties of the analyzing powers and the polarization-dependent differential cross-sections could be determined more accuratly.

Systematic uncertainties associated with solid angles and carbon background subractions are, in general, angle dependent. Because of the forward-backward symmetry of the $pp \rightarrow \pi^+ d$ reaction, such uncertainties can simulate random errors where both forward and backward angle data are superimposed (as happens, for example, when the cross-section is plotted as a function of $\cos^2(\theta^*_\pi)$ (see, for example, Figure (4.20)). Consider, for example, the systematic uncertainties associated with the measurement of the MWPC dimensions, the pion-decay and energy-loss corrections to the solid angles, and the carbon background subtractions; all of which are expected to be reasonably smooth function of the proton beam energy and pion laboratory angle. As such, the systematic uncertainties characterizing the differential cross-sections for a few closely spaced pion lab angles may not be apparent. This is not the case when points of similar $\cos^2(\theta^*_\pi)$ but very different laboratory angles are compared (take as an extreme case, the pion laboratory angles associated with $\cos^2(\theta_\pi^*) \gtrsim 1$).

Such points of similar $\cos^2(\theta_\pi^*)$ were measured with different detection systems at different pion laboratory energies and angles. Furthermore, the pion-decay, energy-loss and carbon background corrections will be very different for these points as will their associated systematic uncertainties. Therefore, some of the deviation between two points of similar $\cos^2(\theta_\pi^*)$ (but different laboratory angle) can be due, in part, to systematic uncertainties.

If the errors ascribed for the data points are not 'normally' distributed, but are, nonetheless, used in the usual minimum χ^2 criterion to establish a fit, then the use of common statistical tests (such as the F test) to evaluate the goodness of the fit so obtained are not rigorously justified.

Notwithstanding, the estimated systematic errors associated with the solid angles (that is, of the detector dimensions and of the pion-decay and energy-loss corrections) and with the carbon background subtractions were combined with the random errors and treated as incoherent errors on a point-by-point basis. Although this leads to reasonable values of χ^2/ν for the fits, (see table (4.14), for example) due caution must be exercised in the interpretation of the errors assigned to the extracted coefficients, and the goodness of the fits as indicated by the (χ^2/ν and F) statistical tests.

4.10 FIT OF THE UNPOLARIZED DIFFERENTIAL CROSS-SECTIONS TO A SUM OF LEGENDRE POLYNOMIALS

The unpolarized differential cross-sections were expanded in terms of even-order Legendre polynomials, and the expansion coefficients (the a_i^{00}) were determined by the method of least squares, using general-purpose fitting routines[36]. For each set of differential cross-sections (for example, at each proton energy) a number of such fits were carried out, each with the expansion series truncated at a different order of Legendre polynomial (second, fourth, sixth, and eighth order truncations were examined). The results of these fits are tabulated in table (4.14) and (4.15). In the following we first discuss the statistical significance of adding fourth order terms to second order fits, and then discuss the effect of the addition of sixth and eighth order terms to the expansion function series. The higher order terms (in particular, those associated with the a_4^{00} and a_6^{00} coefficients) are, in the intermediate energy region, expected to be insignificant (near zero) for energies below some "turn-on threshold", above which they might be expected to display an appropriate energy dependence.

Globally, when averaged over all data sets for all energies, the reduced χ^2 (χ^2/ν) changes insignificantly (from an average value of 1.4) when the fourth order terms

Table (4.14)

Fits of the Unpolarized Differential Cross-Sections to a Sum of Legendre Polynomials.

a_0^{00}	a_2^{00}	a_4^{00}	a_6^{00}	a_8^{00}	ν	χ^2	χ^2/ν
350 MeV data; 15 points							
399(3)	397(8)				13	6.16	0.47
401(4)	405(13)	9(12)			12	5.60	0.47
407(7)	430(26)	44(35)	26(24)		11	4.49	0.41
398(20)	392(80)	6(103)	16(87)	-20(40)	10	4.24	0.41
375 MeV data; 28 points							
645(4)	707(8)				26	49.9	1.92
645(4)	706(12)	-1(13)			25	49.9	2.00
637(5)	676(16)	-61(24)	-60(21)		24	41.7	1.74
635(6)	664(27)	-78(40)	-78(40)	-15(27)	23	41.4	1.80
425 MeV data; 17 points							
1200(10)	1340(20)				15	22.4	1.49
1200(10)	1350(30)	20(30)			14	21.9	1.56
1200(10)	1330(40)	-30(50)	-60(40)		13	19.7	1.52
1190(10)	1310(40)	-80(50)	130(60)	-70(50)	12	17.3	1.44
450 MeV data; 16 points							
1700(10)	1910(30)				14	25.7	1.84
1700(10)	1940(40)	50(40)			13	23.9	1.84
1680(20)	1880(40)	-100(60)	-210(60)		12	12.5	1.04
1680(20)	1870(50)	-120(80)	-240(90)	30(70)	11	12.3	1.12
475 MeV data; 17 points							
1930(20)	2130(30)				13	9.67	0.74
1930(20)	2130(40)	0(50)			12	9.67	0.81
1920(20)	2100(40)	-90(60)	-130(60)		11	4.72	0.43
1920(20)	2090(50)	-110(70)	-160(90)	-40(70)	10	4.49	0.45

a_0^{00}	a_2^{00}	a_4^{00}	a_6^{00}	a_8^{00}	ν	χ^2	χ^2/ν
498 MeV data; 17 points							
2320(20)	2570(40)				15	29.7	1.98
2310(20)	2500(40)	-130(50)			14	21.2	1.51
2310(20)	2470(40)	-230(70)	-140(60)		13	15.7	1.21
2310(20)	2460(50)	-240(70)	-150(90)	-20(70)	12	15.7	1.31

The coefficients are measured in μb/sr.

Table (4.15)

Ratio of the Unpolarized Differential Cross-Section Expansion Coefficients to the Total Cross-Section.

a_2^{00}/a_0^{00}	a_4^{00}/a_0^{00}	a_6^{00}/a_0^{00}	χ^2/ν	Fx	Probability of Exceeding Fx Randomly
350 MeV results;					
0.99(2)			0.47		
1.01(3)	0.02(3)		0.47	1.19	10%→25%
1.06(7)	0.11(9)	0.06(6)	0.41	2.7	10%→25%
375 MeV results;					
1.10(2)			1.92		
1.10(2)	0.00(2)		2.00	0	
1.06(3)	-0.10(4)	-0.10(3)	1.74	4.7	2.5%→5%
425 MeV results;					
1.12(2)			1.49		
1.13(3)	0.02(3)		1.56	0.3	>50%
1.11(3)	-0.03(4)	-0.05(3)	1.52	1.5	25%→50%
450 MeV results;					
1.12(2)			1.84		
1.14(2)	0.03(2)		1.84	1.0	~40%
1.12(2)	-0.06(3)	-0.13(4)	1.04	11	.5%→1%
475 MeV results;					
1.10(2)			0.74		
1.10(2)	0.00(3)		0.81	0	
1.09(2)	-0.05(3)	-0.07(3)	0.43	12	.5%→1%

a_2^{00}/a_0^{00}	a_4^{00}/a_0^{00}	a_6^{00}/a_0^{00}	χ^2/ν	Fx	Probability of Exceeding Fx Randomly
498 MeV results;					
1.11(2)			1.98		
1.08(2)	-0.06(2)		1.51	5.6	2.5%→5%
1.07(2)	-0.10(3)	-0.06(3)	1.21	4.6	5%→10%

are incorporated into the fits. It is questionable whether a more detailed analysis of the (individual) χ^2 distributions would be appropriate in this case. Nonetheless, inspection of the statistical tests of a_4^{00} coefficients indicates that only for the case of the 498 MeV data is the term significantly different from zero. The largest reduced χ^2 (χ^2/ν = 2.00) is associated with the 375 MeV data, and the lowest (χ^2/ν = 0.47) with the 350 MeV data.

The 375 MeV data set consists of unpolarized differential cross-sections extracted from runs with both polarized and unpolarized incident beams. This data set has the largest number of points that differ from the fit by more than two standard deviations (4/28 compared to an expectation of .046 based on pure random Gaussian errors). The poorer quality of this data may be the result of uncertainties associated with the restrictions (more for this data set than for any of the others) applied to the detector sizes required to correct for their misplacement. Determination of the adequacy of these fits was supplemented using standard statistical analysis based on the F distribution[37]. This test is based on evaluation of appropriate ratios of χ^2 values associated with different functional forms fit to the data. The ratios are defined in such a way that systematic multiplicative factors affecting these χ^2 values will cancel. The Fx quantity is defined as:

$$Fx = \{ \chi^2(n-1) - \chi^2(n) \}/\{ \chi^2(n)/(N-n-1) \}$$

$$= \Delta\chi^2/(\chi^2/\nu) \tag{84}$$

Where

N - The number of data points

n - The number of coefficients (less one for the constant term) being fit to the data.

The value of Fx is as an indication of the quality of the fit on a term-by-term basis. It tests the significance of the highest order term incorporated into the fit. It does not give an indication of the absolute validity of the fit in question. On the basis of the Fx test above, the a_4^{00} term is most significant in the case of the 498 MeV data (Fx=5.6). This value of Fx has less than a 5% probabilty of being exceeded by that of a randomly distributed data set.

In general, the addition of sixth order terms, unlike that of fourth order, according to the Fx test, has statistical significance. Globally, the energy averaged reduced χ^2 decreases from the previous value of 1.4 to 1.1. Furthermore, all of the Fx values indicate that this term is significant. the results of the fits, (with the exception of the forementioned 375 MeV results, which still has the largest χ^2/ν value), suggest that the data can be split into two groups. The first group consists of the two low energy (350 and 425 MeV) results, and the second consists of the three highest energy (450, 475, and 498 MeV results. The relative sizes of the Fx values associated with these two groups suggests the significance of the sixth order term is increasing with energy.

In general, inclusion of the a_6^{00} terms into the fits results in a decreased value of the a_4^{00} terms. The correlation is such that the a_4^{00} terms all change sign and become negative, with the exceptions of the 350 MeV a_4^{00} coefficient which remains positive, and of the 498 MeV term which was already negative. Overall, (with the exception of the 375 MeV and the 450 MeV data) the changes in a_4^{00} are within the errors associated with this quantity as determined by the fitting procedure. The value of a_4^{00} associated with the 498 MeV data exhibits the smallest change. Interestingly, the magnitudes of both the a_4^{00} and a_6^{00} coefficients are similar at a given energy.

The incorporation of eighth order terms into the expansion series results in generally insignificant a_8^{00} coefficients. Globally, the energy averaged reduced χ^2 remains unchanged (at a value of 1.1). For only the 425 MeV data does the χ^2/ν decrease (slightly) whereas for all other energies the χ^2/ν values increase (slightly). Ideally, the Fx value associated with the 425 MeV would be greater in only 10% to 25% of randomly distributed data sets, suggesting a moderate significance for this term. Nonetheless, given the none ideal distribution of the uncertainties, all a_8^{00} coefficients are considered insignificant. As the a_8^{0} coefficients are expected to be very small in the intermediate energy region, that they are insignificant provides an indication of a lack of systematic contributions to the differential cross-section, to the eighth order at least.

4.11 FIT OF THE POLARIZED DIFFERENTIAL CROSS-SECTION TO A SUM OF ASSOCIATED LEGENDRE POLYNOMIALS

The expansion coefficients b_i^{no} characterizing the expansion of the polarized differential cross-section in terms of Associated Legendre polynomials were obtained from fits of the measured angular distributions. Again, for each data set, fits were done for a varying number of terms. The results are listed in tables (4.16) and (4.17). Addition of the b_5^{no} term is statistically significant (as defined by the F test) for all data sets. It is by far most significant in the case of the 498 MeV data. Addition of a b_6^{no} term to the fits does not significantly change the values of b_5^{no}, indicating a very small inter-correlation of these coefficients. However, there is very little statistical reason for adding it, as the χ^2/ν are affected only slightly by adding this term. The b_6^{no} term is most significant in the case of the 450 MeV data, although it deviates from zero by just over one error bar.

Table (4.16)

Fits of the Polarized Differential Cross-Sections to a Sum of Associated Legendre Polynomials.

b_1^{no}	b_2^{no}	b_3^{no}	b_4^{no}	b_5^{no}	b_6^{no}	ν	χ^2	χ^2/ν
375 MeV. data; 12 points								
-108(3)	17(2)	24(2)	3(2)			8	8.47	1.06
-109(2)	17(2)	26(2)	2(2)	3(2)		7	3.32	0.47
-109(2)	17(2)	25(2)	3(2)	2(2)	1(2)	6	2.21	0.37
450 Mev. data; 16 points								
6(5)	48(5)	133(4)	9(3)			12	33.7	2.81
2(5)	49(5)	139(4)	3(4)	12(4)		11	20.4	1.85
-1(6)	51(5)	143(4)	4(5)	17(4)	-8(5)	10	13.1	1.31
498 MeV. data; 17 points								
316(6)	78(6)	245(5)	22(4)			13	34.9	2.68
315(6)	72(6)	259(5)	19(4)	16(3)		12	10.3	0.85
315(6)	72(6)	259(6)	17(5)	16(4)	-1(4)	11	10.2	0.93

The coefficients are measured in μb/sr.

Table (4.17)

Ratio of the Polarized Differential Cross-Section Expansion Coefficients to the Total Cross-Section.

b_1^{no}/a_0^{oo}	b_2^{no}/a_0^{oo}	b_3^{no}/a_0^{oo}	b_4^{no}/a_0^{oo}	b_5^{no}/a_0^{oo}	b_6^{no}/a_0^{oo}	Fx
375 MeV. results; a_0^{oo} = 645μb.						
-.167(5)	0.026(3)	0.037(3)	0.006(3)		0.012(3)	
-.169(3)	0.026(3)	0.040(3)	0.003(3)	0.006(3)		11
-.169(3)	0.026(3)	0.039(3)	0.006(3)	0.003(3)	0.002(3)	3.0
450 MeV. results; a_0^{oo} = 1700μb.						
0.004(3)	0.028(3)	0.078(2)	0.005(2)			
0.001(3)	0.029(3)	0.082(2)	0.002(2)	0.007(2)		7.5
-.001(4)	0.030(3)	0.084(2)	-0.002(3)	0.010(2)	-0.005(2)	5.6
498 MeV. results; a_0^{oo} = 2310μb.						
0.137(3)	0.034(3)	0.106(2)	0.010(2)			
0.136(3)	0.031(3)	0.112(2)	0.008(2)	0.007(1)		29
0.136(3)	0.031(3)	0.112(2)	0.007(2)	0.007(2)	0.00(2)	0.1

5. DISCUSSION OF THE RESULTS

5.1 INTRODUCTION

The expansion coefficients of both the unpolarized and the polarized differential cross-sections are plotted and compared with existing results in figures (5.1) through (5.9). In addition, the predictions of several theoretical approaches are shown, one is a Coupled Channel Model, and the other two are Unitary Model predictions. The differential cross-sections are considered here as functions of pion center-of-mass momentum η, expressed in units of m_π/c. Because of the importance of phase-space in this near-threshold region, pion momentum was considered to be a convenient variable to use when comparing the differential cross-sections resulting from measurements of the $pp \rightarrow \pi^+ d$ reaction (and its inverse, the $\pi^+ d \rightarrow pp$ reaction) to those deduced form measurements of the $np \rightarrow \pi^0 d$ reaction

All expansion coefficients for both the unpolarized and polarized differential cross-sections (other than the isotropic part of the unpolarized differential cross-section, a_0^{00}) are shown here normalized to the total cross-section a_0^{00}, in order to remove the gross energy dependence of the coefficients (which, in general, are similar to that of the total cross-section). This method of displaying the coefficients also eliminates effects of some of the systematic uncertainties characterizing the individual data sets. The significance of the sixth order expansion coefficient of the unpolarized differential cross-section, a_8^{00}, which was found to be generally more significant at higher energies (discussed in section (4.10)), is also discussed.

5.2 THE UNPOLARIZED DIFFERENTIAL CROSS-SECTION

The total cross-section a_0^{00} is plotted in figure (5.1) and the remaining a_i^{00}/a_0^{00} ratios describing the shape of the unpolarized differential cross-section angular distributions are plotted in figures (5.2), (5.3), and (5.4). Also indicated on these plots are relevant existing precision measurements (surveyed by G. Jones[35,38]) and the theoretical predictions of Niskanen[25] (the Coupled Channel Model), Blankleider[39] and Lyon group[40] (both using Unitary Models). The theoretical curves illustrate the extent to which the current theories are able to describe this fundamental reaction. On each plot our data is represented by two sets of coefficients. The first set results from fits of the data to Legendre series terminated at the fourth order terms, and the second set results from fits of the data to the expansion series truncated at the sixth order terms. The set of a_i^{00} coefficients considered to most reasonable (significant) are indicated by solid symbols on the respective plots.

Consider first the total differential cross-section, a_0^{00}, depicted in figure (5.1). This coefficient is relatively large and is, as expected, quite insensitive to

Figure (5.1)

The Total Cross-Sections.

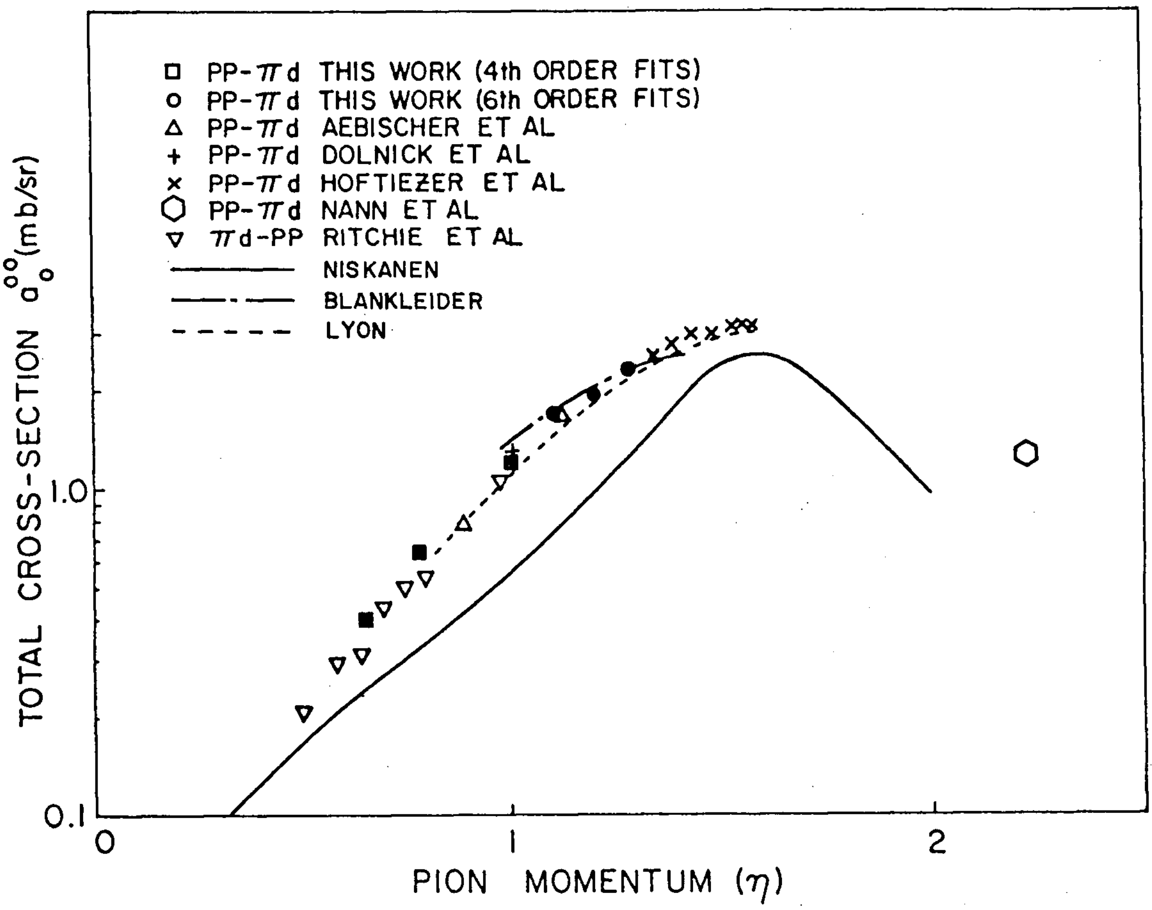

The coefficients of the zeroth order (the isotropic) term of the Legendre polynomial expansion of the unpolarized differential cross-section as a function of the pion centre-of-mass momentum η. Here, the coefficient associated with the recommended order of truncation (either fourth or sixth) of the Legendre polynomial series is identified by a solid symbol.

Figure (5.2)

Ratio of the Coefficients of the Second Order Legendre Polynomial Terms to the Total Cross-Section.

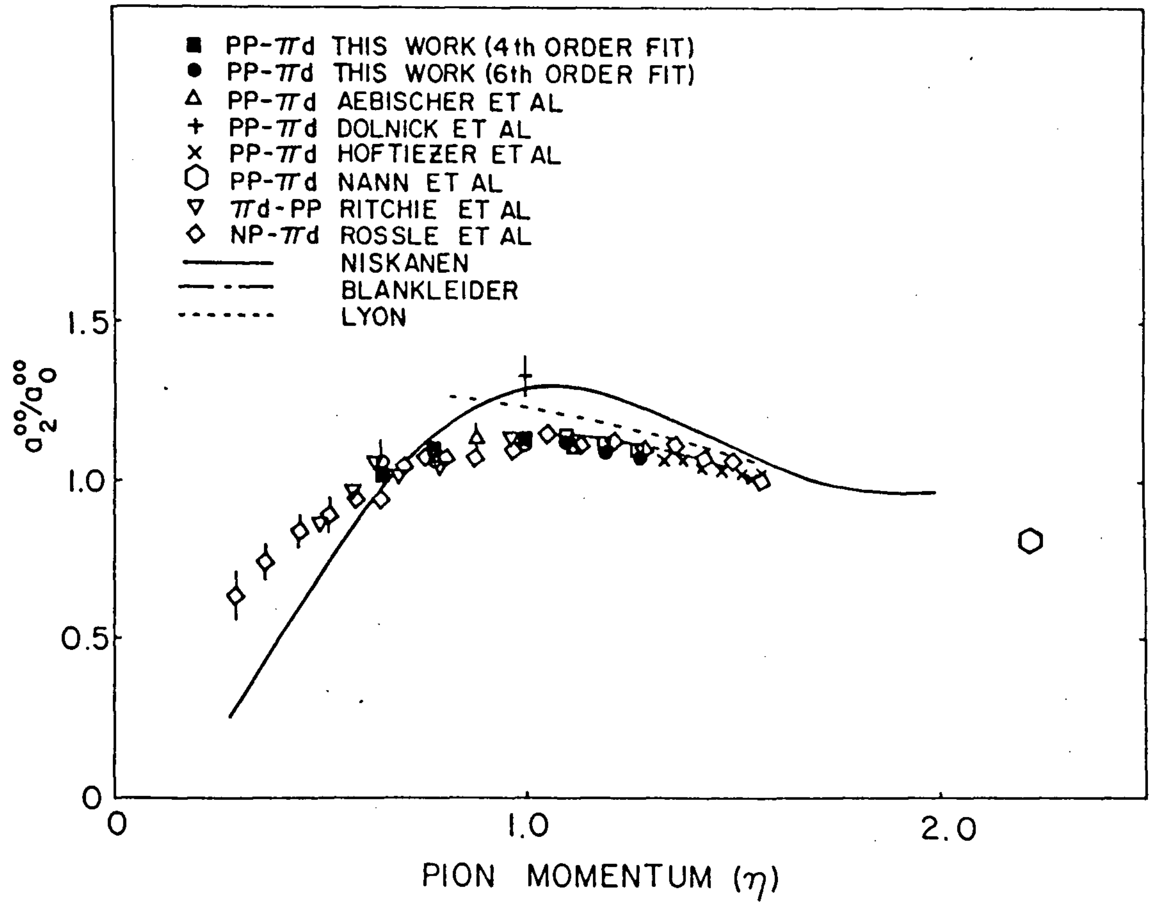

The coefficients of the second order term of the Legendre polynomial expansion of the unpolarized differential cross-section normalized to the total cross-section a_0^{oo} is shown as a function of the pion centre-of-mass momentum η. Here, the coefficient associated with the recommended order of truncation (either fourth or sixth) of the Legendre polynomial series is identified by a solid symbol.

Figure (5.3)

Ratio of the Coefficients of the Fourth Order Legendre Polynomial Terms to the Total Cross-Section.

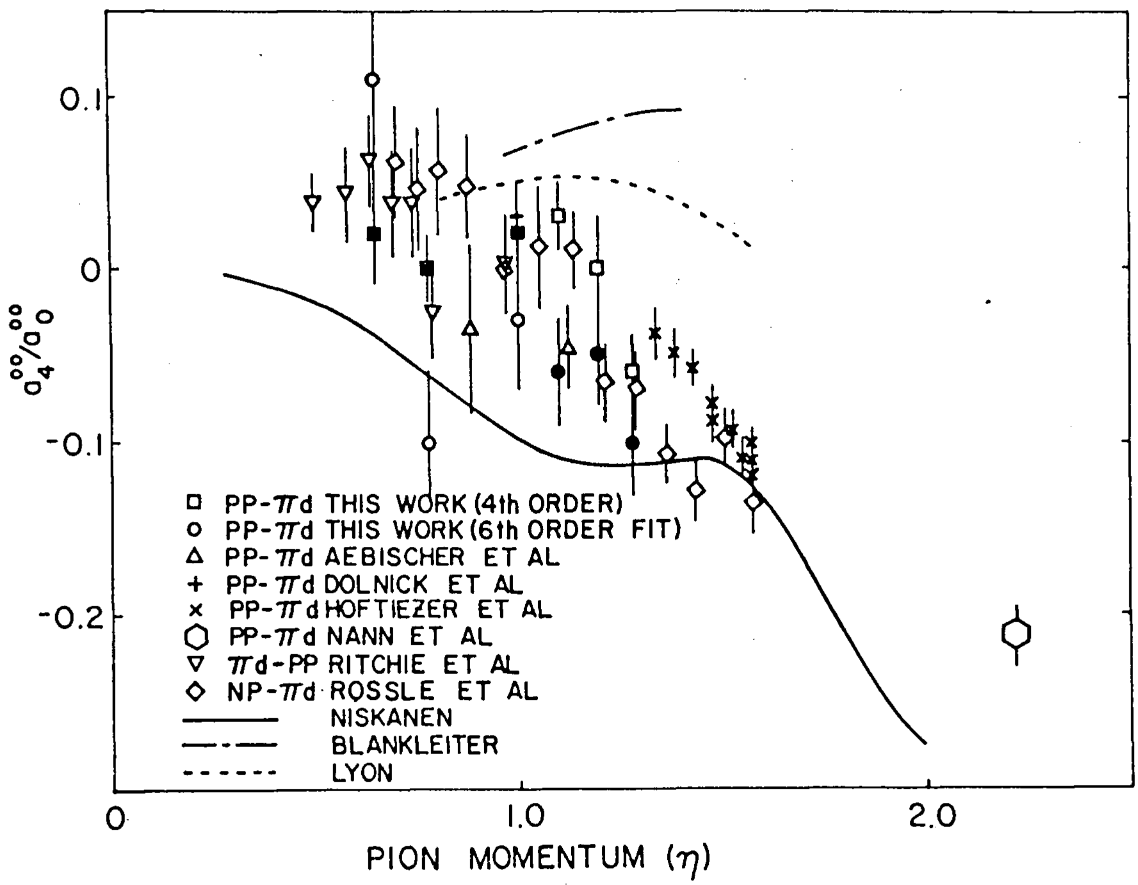

The coefficients of the fourth order term of the Legendre polynomial expansion of the unpolarized differential cross-section normalized to the total cross-section a_0^{oo} is shown as a function of the pion centre-of-mass momentum η. Here, the coefficient associated with the recommended order of truncation (either fourth or sixth) of the Legendre polynomial series is identified by a solid symbol.

Figure (5.4)

Ratio of the Coefficients of the Sixth Order Legendre Polynomial Terms to the Total Cross-Section.

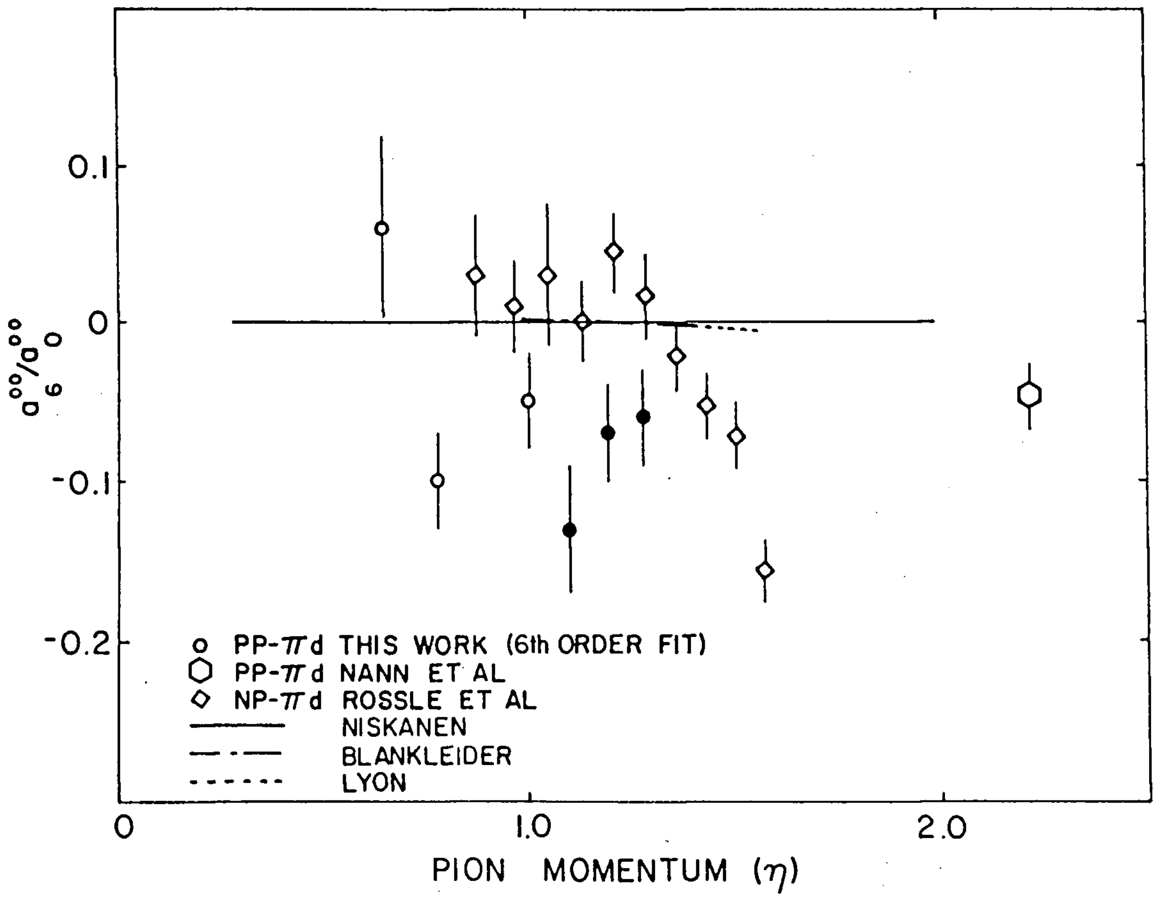

The coefficients of the sixth order term of the Legendre polynomial expansion of the unpolarized differential cross-section normalized to the total cross-section $a_0^{o o}$ is shown as a function of the pion centre-of-mass momentum η. Here, the coefficient associated with the recommended order of truncation (either fourth or sixth) of the Legendre polynomial series is identified by a solid symbol.

the number of terms in the fit. Our total cross-sections are in good agreement with the precision measurements of Hoftiezer et al.[41] at higher values of η. They are in significant disagreement however, (that is, by typically many standard deviations, depending on the point) with those of Ritchie et al.[42] over the lower values of η where the two data sets overlap. The origin of this large discrepancy is probably the result of a large systematic uncertainty associated with the normalization of the incident pion beam current for the $\pi^{+}d \rightarrow pp$ measurements of Ritchie et al.[42] As the method of normalization of the incident proton beam current used in our experiment is based on measurements of the well known pp-elastic reaction cross-sections[10], no such large systematic error is expected to contibute to our uncertainties. The Coupled Channel Model[25] reproduce the trend of the total cross-section but not its magnitude, whereas the Unitary Models[39,40] are in relatively good agreement with the data.

The coefficient governing the relative contribution of the second order Legendre term a_2^{00}/a_0^{00}, is the dominant term describing the shape of the unpolarized differential cross-section angular distribution in the intermediate energy region. It is depicted in figure (5.2). As seen in the figure, the value of this ratio was found to be quite insensitive to the number of terms included in the Legendre polynomials fit to the data. The agreement between the various data sets is, with the exception of the old datum of

Dolnick et al.[43] (renormalized as suggested by Jones[35]), quite satisfactory. Reasonable agreement should be expected, however, since both a_2^{00} and a_0^{00} are large relative to the higher order coefficients and any common systematic uncertainty associated with a particular experiment will cancel when such a ratio is formed. Theoretically,the Coupled Channel Model[25] under estimates the a_2^{00}/a_0^{00} ratio for $\eta \lesssim 0.65$(350 MeV) and over estimates it for larger values of η. The theoretical predictions shown in the figure do, however, correctly reproduce the overall trend of the data with Blankleider's[39] unitary theory giving the best aggreement in this energy region.

The magnitudes of the higher order terms (a_4^{00} and a_6^{00}) are an order of magnitude smaller than those of the leading terms. In fact, the combined contribution to the differential cross-section of these terms at a typical data point is similar in magnitude (a few percent) to that of the uncertainty associated with that point. As such, some degree of correlation between the a_4^{00} and a_6^{00} coefficients is expected to be present. Such a correlation is manifested by the observation of a dependence of the value for the a_4^{00} coefficient on the order assumed for the Legendre polynomial fit to the data.

The ratios of the fourth to zeroth order expansion coefficients, a_4^{00}/a_0^{00}, are depicted in figure (5.3). Since, as discussed in Section (4.10), there appears to be statistical significance to the sixth order terms at the three highest energies (450, 475, and 498 MeV), the recomended values for the a_4^{00}/a_0^{00} are thus obtained from fits to the sixth order Legendre functions. For the three lower energy points, the a_4^{00}/a_0^{00} ratios recomended are those derived from the results of fits of the data to fourth order Legendre functions. These "recommended" values are designated as solid symbols on the figures. As such, our a_4^{00}/a_0^{00} ratios are consistent with zero for energies from 350 to 425 MeV ($0.65 \lesssim \eta \lesssim 1.00$). In this energy region, our data are not inconsistent with those of Ritchie et al.[42] ($\pi^+ d \rightarrow pp$) or Rössle et al.[44] ($np \rightarrow \pi^0 d$). If anything, our results in this region are somewhat closer to zero than the overall positive trend charaterizing the other data. For energies greater than 425 MeV ($\eta > 1$) our data displays a negative trend consistent with the data of Rössle et al.[44] ($np \rightarrow \pi^0 d$), Ritchie et al.[42] ($\pi^+ d \rightarrow pp$) and the datum of Aebischer et al. [45] ($pp \rightarrow \pi^+ d$), but disagree in magnitude with the precision results of Hoftiezer et al.[41]. In fact, the weight of the evidence suggests that the results of Hoftiezer et al.[41] are incorrect, perhaps by an overall systematic factor.

For the higer order terms, the theoretical predictions are much less satisfactory, with only the Coupled Channel Model predicting the correct sign of the measured results in this energy region. Interestingly, booth Unitary Models predict a small positive value of a_4^{00}/a_0^{00} for $\eta < 1$.

The ratio of the sixth order to the zeroth order expansion coefficients a_6^{00}/a_0^{00}, are shown in figure (5.4). Of the values from our fits presented on this plot, only the three highest energy results are believed to be statistically significant. They are negative in the region over which Rössle et al.[44] ($np \rightarrow \pi^0 d$) results are essentially zero. Nonetheless, the Rössle results are negative at slightly higher energies. Overall, there appears to be evidence of a negative trend for this ratio although its magnitude is not clearly determined. Expectations based on the formentioned current theories are negligable in this energy region.

5.3 THE POLARIZED DIFFERENTIAL CROSS-SECTION

The b_i^{no}/a_0^{00} results are depicted in figures (5.5),(5.6),(5.7),(5.8) and (5.9). They are derived from the first direct precision measurements of the polarized differential cross-sections in this energy region and compliment those of Hoftiezer et al.[41] at higher energies. Previous results in this energy region (Mathie et al.[46] were based on the product of estimated (or measured) unpolarized differential cross-sections together with measured analyzing powers. The b_i^{no} coefficients presented here were obtained from fits (see table (4.16)) to our polarized differential cross-sections, wheras our published results (see figure (2) in appendix (3)) were deduced from the measured analyzing powers (see

Figure (5.5)

Ratio of the Coefficients of the First Order Associated Legendre Polynomial Terms to the Total Cross-Section.

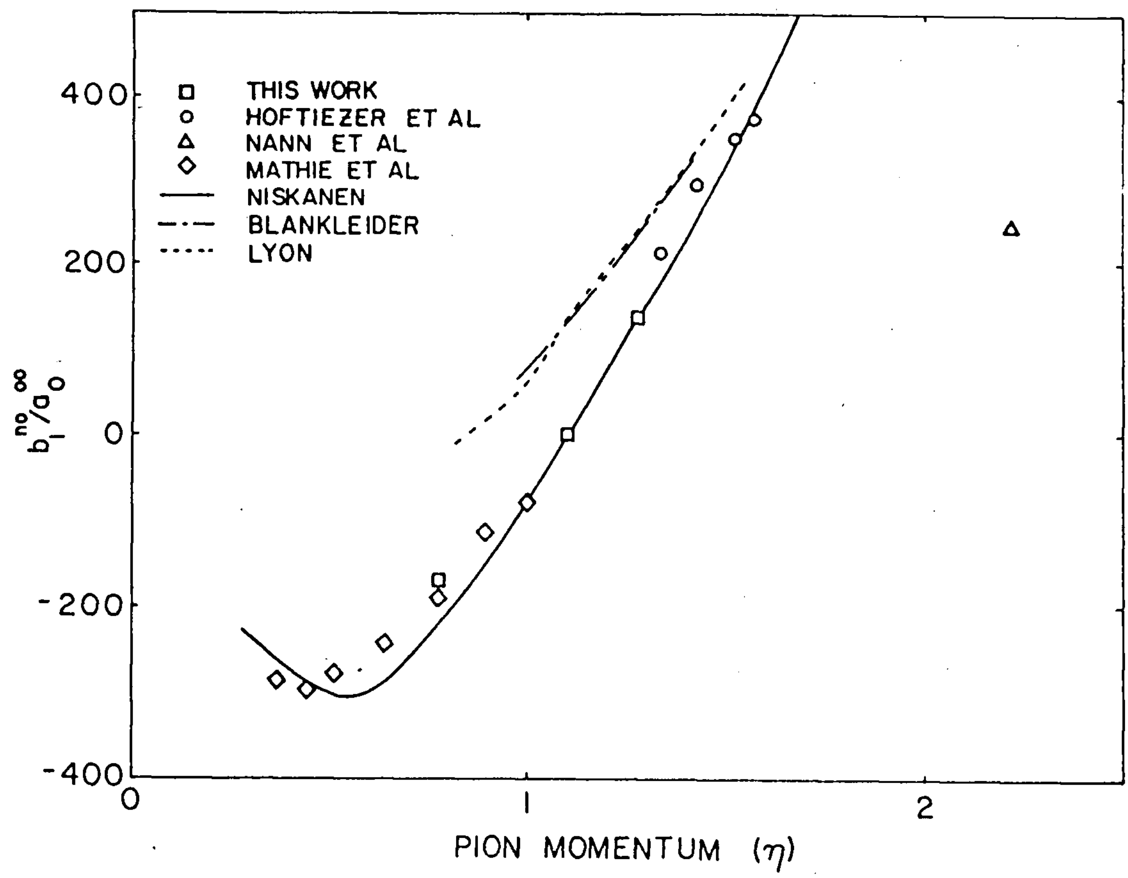

The coefficients of the first order term of the Associated Legendre polynomial expansion of the polarized differential cross-section normalized to the total cross-section a_0^{oo} is shown as a function of the pion centre-of-mass momentum η.

Figure (5.6)

Ratio of the Coefficients of the Second Order Associated Legendre Polynomial Terms to the Total Cross-Section.

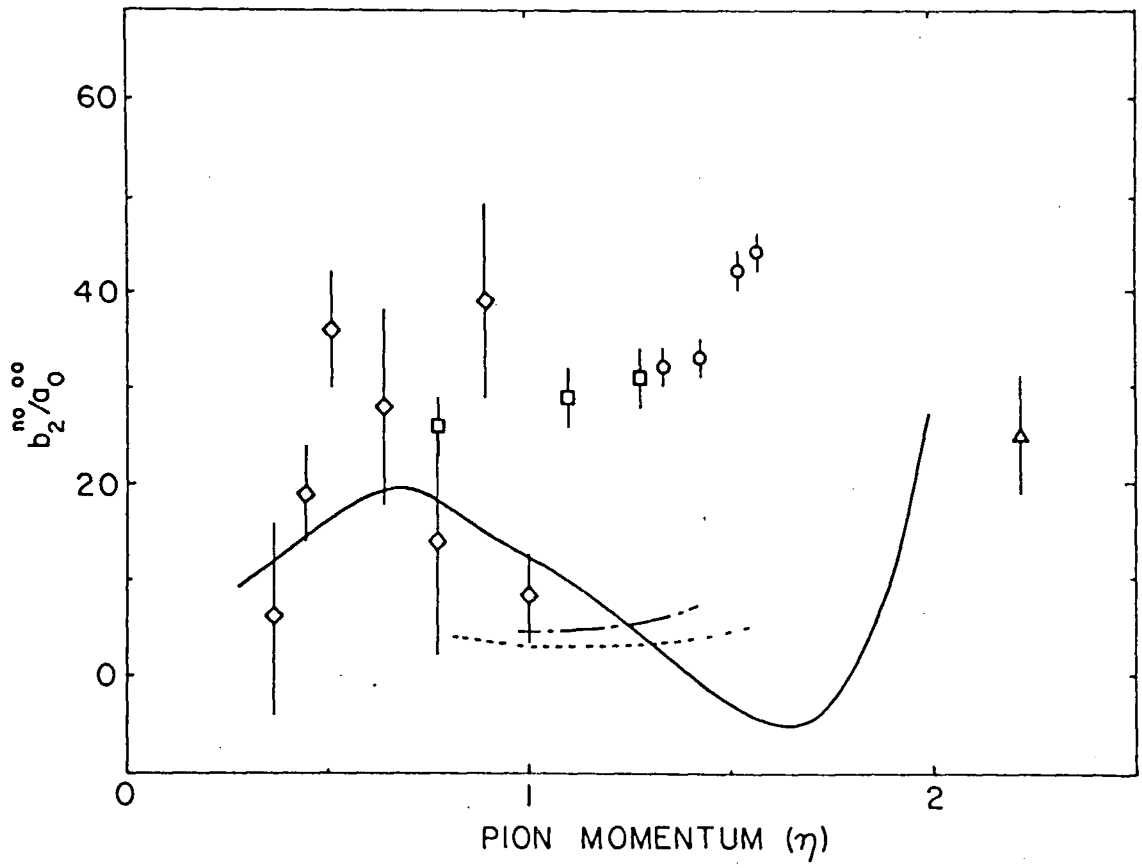

The coefficients of the second order term of the Associated Legendre polynomial expansion of the polarized differential cross-section normalized to the total cross-section a_0^{oo} is shown as a function of the pion centre-of-mass momentum η.

Figure (5.7)

Ratio of the Coefficients of the Third Order Associated Legendre Polynomial Terms to the Total Cross-Section.

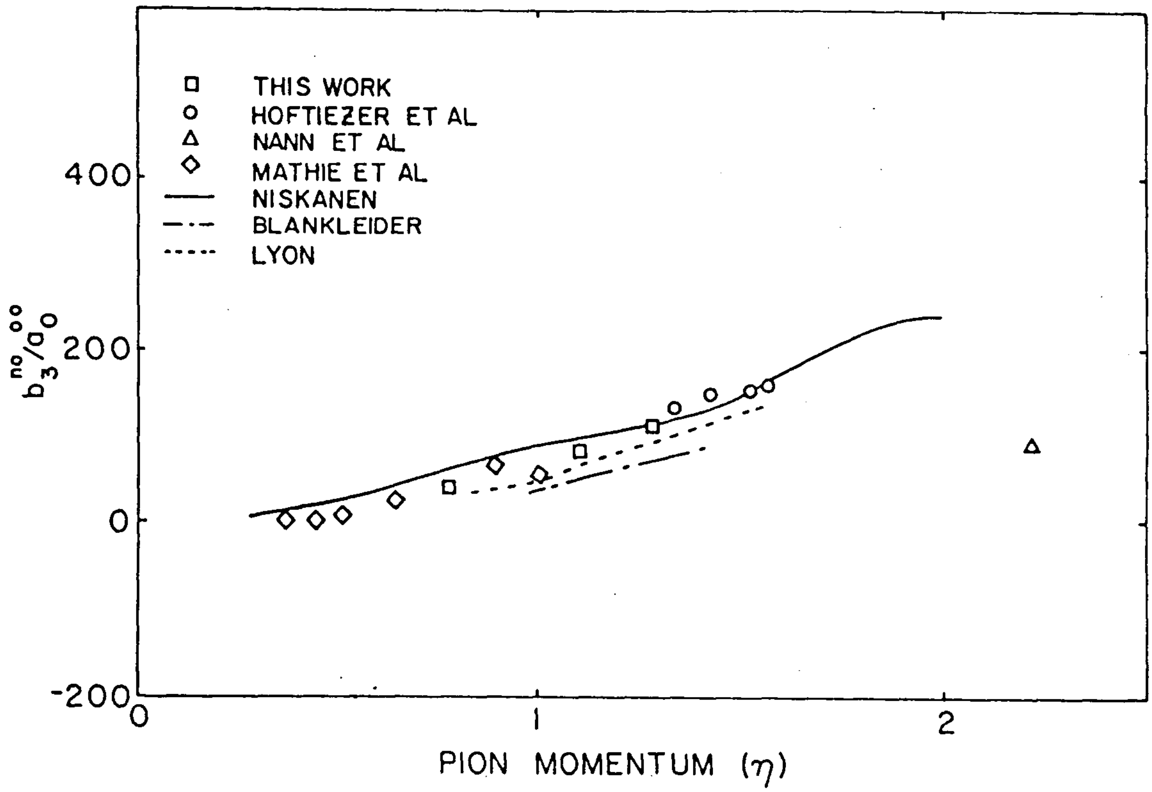

The coefficients of the third order term of the Associated Legendre polynomial expansion of the polarized differential cross-section normalized to the total cross-section a_0^{oo} is shown as a function of the pion centre-of-mass momentum η.

Figure (5.8)

Ratio of the Coefficients of the Fourth Order Associated Legendre Polynomial Terms to the Total Cross-Section.

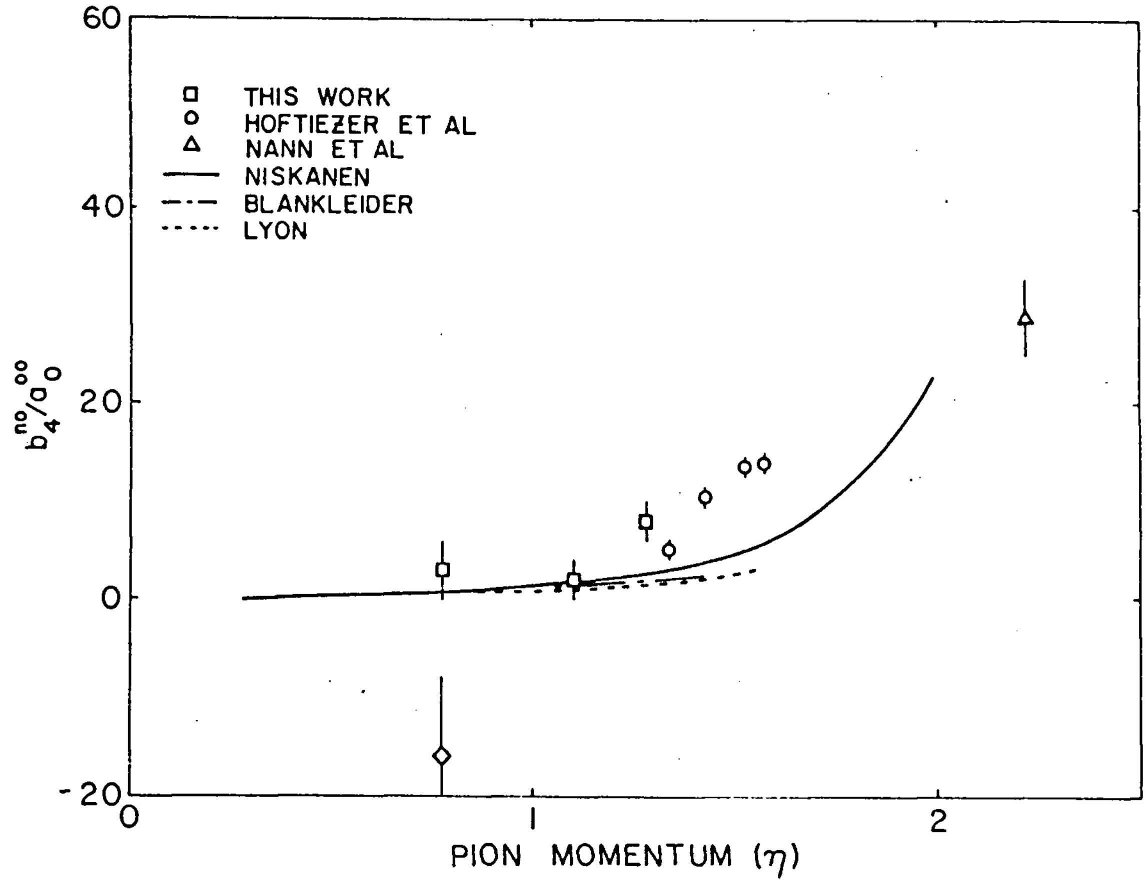

The coefficients of the fourth order term of the Associated Legendre polynomial expansion of the polarized differential cross-section normalized to the total cross-section a_0^{0o} is shown as a function of the pion centre-of-mass momentum η.

Figure (5.9)

Ratio of the Coefficients of the Fifth Order Associated Legendre Polynomial Terms to the Total Cross-Section.

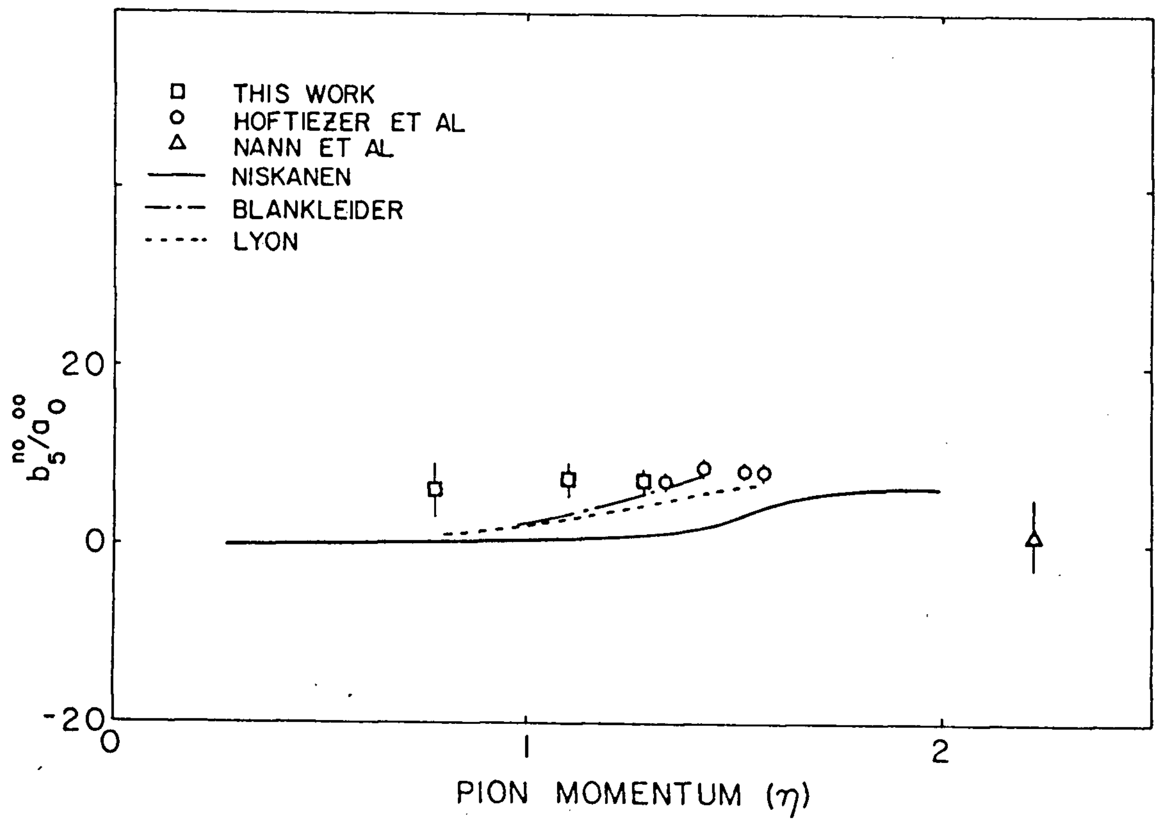

The coefficients of the fifth order term of the Associated Legendre polynomial expansion of the polarized differential cross-section normalized to the total cross-section a_0^{00} is shown as a function of the pion centre-of-mass momentum η.

figures (4.29), (4.30), and (4.31)) together with estimates of the shape of the unpolarized differential cross-sections obtained from published differential cross-section data. Only minor changes from our published values caharacterized the more exact analysis.

The b_5^{no} coefficient is, according to the F test results, significant in all cases (see table (4.17)). This significance is reflected in the drop of the associated χ^2/ν values. This term is most significant (according to the F test) and thus the smallest uncetainty at 498 MeV. At 375 MeV the b_5^{no} term, although statistically significant according to the F test, is not inconsistent with zero when the magnitude of the error bars is considered.

Addition of a sixth order term to the expansion series yields b_6^{no} values consistent with zero for the 375 and 498 MeV data even though this term is deemed significant by the F test and the associated drop in χ^2/ν of the fit. The correlations of the b_i^{no} coefficients, evident through the variations in value of the lower order b_i^{no} coefficients as a function of the order (number of terms) of the Associated Legendre polynomial fit to the data, are greatest within the 450 MeV data set. Overall, however, such variations are within the uncertainty limits derived from the error matrix.

The values of the b_i^{no}/a_0^{oo} fifth order expansion of these results are consistent with our published results, results obtained from a significantly less rigourous analysis of our data.

Values of the b_i^{no} coefficients together with a comparison to other data and predictions of the Coupled Channel Model are presented in detail in our previous publication[9]. Predictions of the Unified Models of Blankleider and Lyon are indicated on the figures presented here[25,39,40]. In general, the Unified Models qualitatively reproduce the trend of the energy dependence of the b_i^{no}/a_0^{oo} ratios but, again, inadequate quantitativly.

6. CONCLUSION

In this thesis the first direct precision measurements of the polarized differential cross-sections and precision measurements of the unpolarized differential cross-sections for proton energies less than 498 MeV are presented. A two-arm apparatus consisting of scintillation counters and multi-wire proportional chambers was constructed of simple geometric properties, capable of measuring $pp \rightarrow \pi^+ d$ differential cross-sections over an angular range of 20° to 150° C.M., for both polarized and unpolarized incident proton beams. Trajectory reconstruction using information from the proportional chambers, together with employment of redundant counter systems which enabled on-line determination of counter efficiencies facilitated event definition to an accuracy required for the precision desired.

In addition, the incident proton beam current normalization, a critical element of a precision experiment such as this, was based on the simultaneous measurement of the $pp \rightarrow pp$ elastic reaction and of the $pp \rightarrow \pi^+ d$ reaction from the same production target. This development required knowledge of the 90° C.M. differential cross-section to a higher accuracy than existed. Prior to this experiment, such measurements were made and the results published[10]. This method eliminates uncertainties associated with either the target thickness or the angle of the target relative to the beam direction. In addition, uncertainties resulting from beam loss that can result when the production target and the beam current monitoring device are physically separated were also eliminated.

The relativistic transformation properties of the forward-backward symmetry of the reaction kinematics in the center-of-mass system into the laboratory system were exploited to estimate and reduce systematic uncertainties associated with the apparatus acceptance solid angles, and pion-decay and energy-loss corrections.

Carbon background contributions, although small initially, were clearly identified through measurements carried out with a pure carbon target. A model for the carbon background was constructed and used as a basis for a background subtraction technique. Furthermore, in the case of the analyzing power results (results that have already been published, Giles <u>et al.</u>[9]) the background was reduced to an insignificant level by a method based on the kinematic reconstruction of each event. The reliability of our background handling techiques is demonstrated by the consistency of the results obtained by the two methods.

Prior to this experiment, knowledge of the total cross-section of this fundamental reaction was surprisingly poorly known in this energy region. The work of Hofteizer <u>et al.</u>[41] defined the magnitude of the cross-section over the energy region of 514 to 583 MeV, while at lower energies the best measurements were those of Ritchie <u>et al.</u>[42] obtained through investigation of the

$\pi^+ d \rightarrow pp$ reaction. Unfortunately, their results suffered from internal inconsistencies of the order of ten percent.

Reliable precision measurements of the total cross-section (a_0^{00}) are now available from 350 to 498 MeV as a result of the work presented here.

Since the two terms associated with the a_0^{00} and a_2^{00} coefficients dominate the angular dependence of the reaction, and since common systematic errors cancel when calculating their ratio, the a_2^{00}/a_0^{00} ratio is experimentally the most straightforward to measure precisely. Our measurements of this quantity verify the trends already evident in published results. Nonetheless, when considering the much smaller a_4^{00}/a_0^{00} ratio, the results of previous workers are much less consistent with each other. In this case, our results are reasonably consistent with those of Rössle et al.[44] (obtained from measurements of the $np \rightarrow \pi^0 d$ reaction) and Ritchie et al.[42] ($\pi^+ d \rightarrow pp$), neither of which were deduced from direct measurements of the $pp \rightarrow \pi^+ d$ system. However, our results disagree with those of Hofteizer et al.[41] (which may suffer an overall systematic uncertainty) who, like ourselves, measured the differential cross-section of the $pp \rightarrow \pi^+ d$ reaction directly.

Our a_6^{00}/a_0^{00} results at the highest energy measured tend to support the negative trend established at higher energies by Rössle et al.[44] ($np \rightarrow \pi^0 d$).

There is no statistical requirement for an eighth order term (associated with the a_8^{00} coefficient) to describe our data. If one assumes that the a_8^{00} coefficient is indeed zero (as predicted by, for example, the Coupled Channel Model of Niskanen[25]) then the observation that it is insignificant suggests the absence of an angular dependent systematic uncertainty, to the eighth order at least.

The first ever direct precision measurement of the polarized differential cross-sections below 498 MeV are presented in this thesis. The b_i^{no} expansion coefficients derived from these results are in agreement, within the stated uncertainties, with our previously published results (Giles <u>et al.</u>[9]).

The b_1^{no} and b_3^{no} coefficients are dominant in this energy region and our results in this case, again, verify a trend indicated by published work.

This is not the case, however, when the significantly smaller (by an order of magnitude) b_2^{no}, b_4^{no}, and b_5^{no} coefficients are considered. Of these coefficients only the b_2^{no} term has been published for energies below 498 MeV, and the errors associated with these data are large. Thus, our results provide the only precision determination of the spin dependent b_2^{no}, b_4^{no} and of b_5^{no} coefficients at energies below 498 MeV.

Interestingly, the only (if limited) evidence of a non-zero b_6^{no} coefficient is present at 450 MeV, which is the same energy as our largest (in magnitude) determined a_6^{00}/a_0^{00} ratio.

A non-zero a_6^{00} coefficient requires a significant contribution from the partial wave amplitude of designation a_8 or higher, which in turn is associated with a $^1G_4$ (or higher relative angular momentum configuration) NN initial state. When compared to the theoretical descriptions of this reaction, the Coupled Channel Model[25] which provides the best qualitative predictions of our results, fails to take into account contributions from such channels, the $^1G_4$ in particular, and thus cannot be expected to yield realistic results in the 498 MeV energy region.

As high precision results such as ours become available it is increasingly clear that the present theoretical description of this fundamental process, even in the near threshold region, requires substantial refinement, a development that will undoubtedly be guided by the availability of such results.

APPENDIX I: THE DIFFERENTIAL CROSS SECTION FOR PROTON-PROTON ELASTIC SCATTERING AT 90°C.M. BETWEEN 300 AND 500 MEV.

Nuclear Physics A412 (1984) 189–194

THE DIFFERENTIAL CROSS SECTION FOR PROTON–PROTON ELASTIC SCATTERING AT 90° c.m. BETWEEN 300 AND 500 MeV

D. OTTEWELL and P. WALDEN

TRIUMF, 4004 Wesbrook Mall, Vancouver, BC, Canada V6T 2A3

E.G. AULD, G. GILES, G. JONES, G.J. LOLOS, B.J. McPARLAND and W. ZIEGLER

Physics Department, University of British Columbia, Vancouver, BC, Canada V6T 2A6

and

W. FALK

Physics Department, University of Manitoba, Winnipeg, Man., Canada R3T 2N2

Received 18 July 1983

Abstract: The absolute differential cross section for proton–proton elastic scattering has been measured at 90° c.m. for 300, 350, 400, 450 and 500 MeV. The statistical uncertainty of the measurements is 0.5% with an additional systematic normalization uncertainty of 1.8%. The results are compared to phase-shift analyses.

E

NUCLEAR REACTION ^{1}H(p, p), $E = 300, 350, 400, 450, 500$ MeV; measured $\sigma(\theta = 90°)$. Comparison with phase-shift analyses.

The motivation for the experimental measurement of the pp elastic cross section reported here stemmed from the need to use it as a calibration in another proton-induced reaction. Measurements of the differential cross section of the ^{1}H(p, π)^{2}H reaction [1]) were facilitated by simultaneously measuring the protons elastically scattered at 90° from the target protons. By this means, the ^{1}H(p, π)^{2}H cross section was measured relative to the pp elastic cross section. Prior to the ^{1}H(p, π)^{2}H measurements, consideration of the elastic data available in the energy range of 300 to 500 MeV [ref. [2])] revealed both lack of precision of the relevant data (5 or 10%) and inconsistency of the existing data with some of the phase-shift fits to similar levels. This was much larger than the accuracy desired (1%). Clearly a precise knowledge of the pp elastic cross section was required to provide an adequate constraint for the phase-shift analyses of nucleon–nucleon scattering. These are, in turn, useful for predicting cross sections in other energy regions as well as other observables.

For these reasons the pp elastic cross section was measured at 90° for 5 energies from 300 MeV to 500 MeV to a precision of approximately 1.8%. The experiment

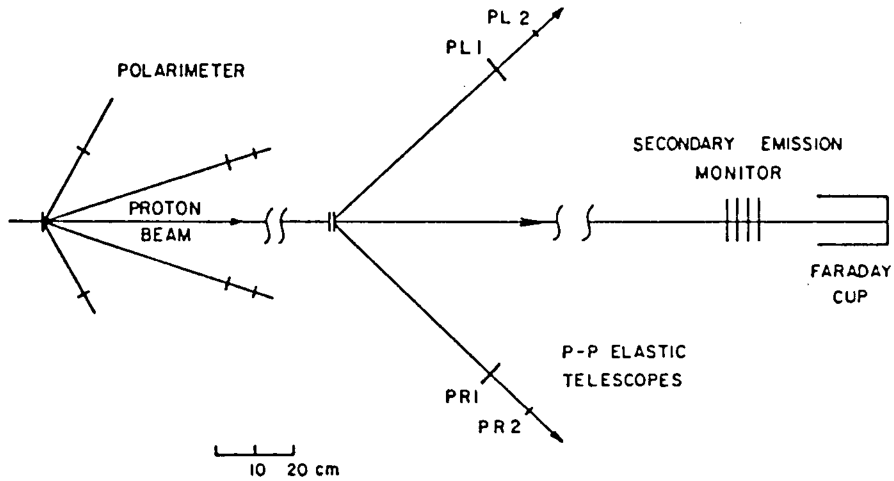

Fig. 1. Schematic representation of the experimental set-up. The scattered protons were detected in the two-arm system. Proton intensities were measured with a secondary emission monitor and a Faraday cup downstream of the target and a polarimeter located upstream of the target. The scale shown applies only to the polarimeter and the pp elastic telescope.

was performed using the variable energy unpolarized beam at the T1 target position on the 4B external proton beam at TRIUMF. The experimental set-up is shown in fig. 1. The protons resulting from the pp elastic scattering were detected in coincidence by the two-arm system shown. The 90° (c.m.) scattering angle was chosen because the 90° analyzing power is zero providing optimal reference data even for experiments using polarized beams. The rear detectors of the telescopes ($5\times2\times0.64\ \mathrm{cm}^3$ at 71.9 cm) defined the solid angle. The logic for each event was $(\mathrm{PL1}\cdot\mathrm{PL2})\cdot\mathrm{PR1}+(\mathrm{PR1}\cdot\mathrm{PR2})\cdot\mathrm{PL1}$, or left-arm events plus right-arm events. The percentage of events counted twice by this logic never exceeded 10%. Monte Carlo calculations at each energy defined the energy dependence of the solid angle. The experimental targets used were two small CH_2 targets ($5\times5\times0.163\ \mathrm{cm}^3$ and $5\times5\times0.511\ \mathrm{cm}^3$) together with one (background) C-target ($5\times5\times0.196\ \mathrm{cm}^3$).

Proton beam intensities were monitored by three independent devices. A double three-arm polarimeter located 2.7 m upstream, normally used for polarized beam experiments, monitored pp elastic scattering from an independent target. The beam passed through a secondary emission monitor located 21 m downstream of the target before being stopped in a Faraday cup which provided a measure of the total beam charge transmitted.

Beam intensities were varied from 0.01 nA to 2.5 nA to test for rate effects on all the counters. The accidental rates in the pp elastic telescopes ranged from 0.2% to 4% (the higher value came from the thick-target, high-current runs). Although the results were all consistent when corrected properly for these accidental rates, the nominal currents throughout the experiment were kept to 0.1 nA. In addition, tests of other systematics were made by deliberately steering the beam by amounts varying up to 1.5 cm to the left and right of target center. No measurable effect on the total pp elastic telescope counting rate was observed.

All singles and coincidence rates for the scintillation detector system were recorded along with number of cyclotron r.f. timing pulses. Due to the high counting rates involved the contents of all the CAMAC scalers were recorded by a PDP11/34 on magnetic tape every 2.5 s, thus providing a running log of the experiment.

The cross sections reported here were normalized to the Faraday cup beam charge measurement. Of all four beam monitors, the polarimeter, the pp elastics, the SEM and the Faraday cup, it was found that the ratio of the pp elastic telescope events and the Faraday cup charge was the most consistent over time, the consistency being within 0.5%. A detailed analysis of correlations and ratios between each of the beam monitors showed that the other two beam monitors, the polarimeter and the SEM, drifted and could not be trusted to less than 2%. Relating such drifts to changes in experimental data taking such as beam current, targets, etc. was not successful.

The Faraday cup and the pp elastic telescope demonstrated reliable consistency over a wide range of beam current rates, target thickness variations and beam tunes. For the results presented here, it was assumed that all the beam charge was detected by the Faraday cup.

All the counting rates were expressed as a mean number per beam burst and manipulated[3]) by Poisson statistics to correct for pulse pile-up and accidentals during individual proton beam "buckets". This careful correction procedure was done because the simplistic method of determining accidentals in the telescopes by delaying one arm with respect to the other by the r.f. period is only an order of magnitude estimate of the real accidental rate. In order to do these corrections all appropriate single, double and triple coincidence rates plus a simple model relating the geometry, rate and size of the telescope counters was utilized to give an appropriate correction. For example, a 4% effect as determined by simple delay line technique in the hardware logic actually corresponded to a 3% real accidental rate. This correction agreed with that required to establish consistency between the high-rate runs and low-rate runs.

Corrections to the data were also made for nuclear reaction losses in the target, scintillation counter and window materials. Protons that were absorbed before scattering did not present a problem as they were lost from both the elastic counters as well as from the Faraday cup. However, corrections were made for scattered protons that were subsequently absorbed in the target, the vacuum windows, the air, or the front detectors of the telescopes. In addition, corrections were necessary to account for loss of beam before the Faraday cup due to the material of the secondary emission monitor. Consideration of such corrections increased the differential cross sections by 0.6 to 1.1% depending on the beam energy and the thickness of the target.

The differential cross section of pp elastic scattering from a CH_2 target is

$$\left.\frac{d\sigma}{d\Omega}\right|_{pp}=\frac{1}{2}\left\{\frac{N_s}{N_p n_t 2\Delta\Omega}-\left.\frac{d\sigma}{d\Omega}\right|_C\right\}, \quad (1)$$

where $d\sigma/d\Omega|_C$ is a measure of events from proton–carbon scattering (discussed below), N_s is the total number of scattered protons detected both pp elastic telescope arms each with c.m. solid angle $\Delta\Omega$, N_p is the number of incident protons determined by charge integration and n_t is the number of target molecules (CH_2) per cm^2. Both N_s and N_p have been corrected for nuclear absorption. The solid angle $\Delta\Omega$ was determined from a Monte Carlo program which included effects of beam profile and multiple scattering. The results of the pp elastic cross section calculated via eq. (1) are shown in table 1.

The contribution of the carbon contained in the CH_2 target was deduced from measurements at each energy using a graphite target. The quantity $d\sigma/d\Omega|_C$ was defined by the equation

$$N_s=N_p n_t \left.\frac{d\sigma}{d\Omega}\right|_C \Delta\Omega\,, \quad (2)$$

where N_s, N_p and n_t are similar quantities to those in eq. (1) except applied to the carbon target runs, and $\Delta\Omega$ is the same solid angle as in eq. (1). The differential cross sections from carbon obtained by this method are also given in table 1.

The values presented in table 1 were obtained from several independent runs (12 runs at 500 MeV, 4 to 6 runs at each of the other energies). The results from the individual runs were averaged to give the final values. The errors presented came from two sources, the counting statistics, and the fluctuations in the ratio of the pp elastic events versus the Faraday cup charge. The latter source, the ratio, had a rms deviation of 0.5% averaged over all runs at all energies. For the CH_2 target runs the fluctuations in the ratio dominated the error whereas for the C-target runs the counting statistics dominated the error.

TABLE 1

The pp elastic absolute differential cross section at 90° c.m. for proton energies E_p; also included is the contribution due to carbon contained in the CH_2 target

E_p (MeV)	Carbon $d\sigma/d\Omega$ (mb/sr)	pp elastic $d\sigma/d\Omega$ 90° c.m. (mb/sr)
300	0.432 ± 0.007	3.769 ± 0.019
350	0.509 ± 0.009	3.759 ± 0.019
400	0.568 ± 0.010	3.742 ± 0.019
450	0.604 ± 0.010	3.682 ± 0.019
500	0.638 ± 0.011	3.471 ± 0.018

In addition there is 1.8% systematic error due to the change in aperture between the front face and rear face of the solid-angle-defining counters due solely to the thickness of the counters. This was not an oversight in the design of the pp elastic telescope as the telescope was originally intended as a beam current monitor which is not influenced by this uncertainty.

To check the reliability of the results, an independent measurement of the beam current was made at 500 MeV by reducing the primary beam current to a level where individual protons were detected with a 3-counter transmission telescope mounted directly downstream of the target chamber. It was necessary to reduce the normal minimum beam intensity by a factor of 1000 to keep the beam rate below $1 \times 10^7 \text{ sec}^{-1}$. This was accomplished by the installation of a 5 cm thick Cu collimator containing a 1 mm hole prior to two bending magnets situated 14 m upstream of the target.

Unfortunately, the collimated beam had a low-energy tail which was the result of beam particles going through energy degradation in the collimator, then going through a larger bending angle in two subsequent downstream dipoles. Such effects were discovered by noticing anomalous behaviour of the in-beam telescope counters and subsequently verified by beam profiles produced on photographic film. It was decided that the geometry of this set-up was bad in that a beam particle passing through the target could not be certain to pass through the beam counter and vice versa. However, since such effects were estimated to be on the order of 3% the measurement nevertheless would serve as a useful check on the Faraday cup data. The data point at 500 MeV with its statistical error, calculated from the beam counter data, is shown in fig. 2 which indicates the degree to which direct beam counting agreed with the Faraday cup results.

The experimental results of the differential cross section are plotted in fig. 2. Included also are the recent results of Chatelain *et al.* from 500 to 600 MeV [ref. [3])]. The two sets of data are in good agreement. The most significant contribution of the two experiments certainly is the precise knowledge of the energy dependence of the cross section in this energy region.

Also plotted in fig. 2 are the "Winter 1982" phase-shift predictions of Arndt [2]) showing the energy dependence of the 0–1 GeV fit. Our data and the Chatelain data have been included in this nucleon–nucleon elastic scattering data base. For comparison the BASQUE phase-shift predictions [4]) are also plotted. It is remarkable how similar the two analyses are considering that the BASQUE results predated the measurements of both Chatelain and ourselves.

It is interesting to compare the Arndt solutions before and after inclusion of the recent data. The "Winter 1981" energy-dependent solution (which predates the data of Chatelain and ourselves) is also plotted in fig. 2. The two solutions agree in the 300 to 400 MeV range but differ by 9% at 500 MeV and 10% at 600 MeV. Some of this "time dependence" may result from the effects of data outside the range of concern.

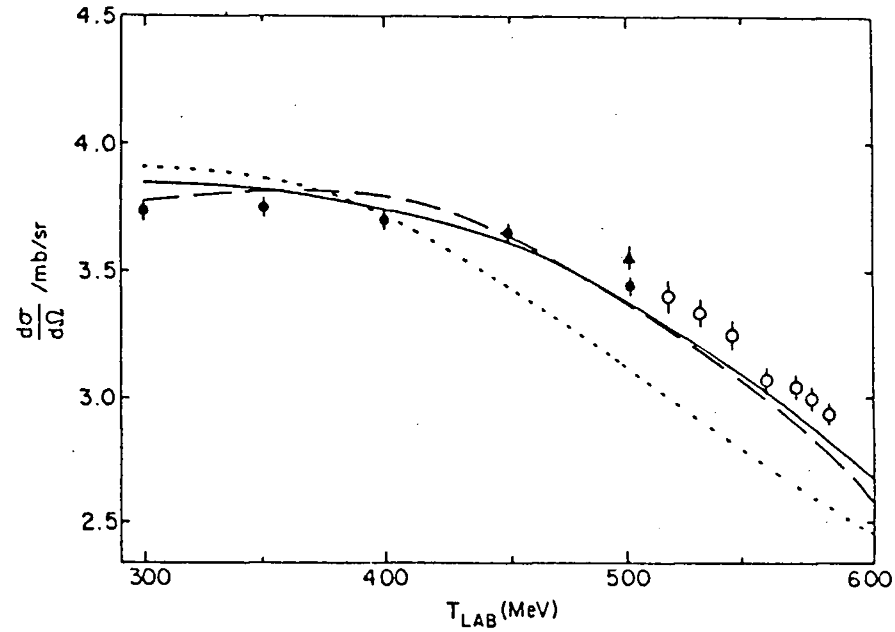

Fig. 2. Comparison of our experimental results (full circles) and those of Chatelain et al. [3]) (open circles) of the pp elastic differential cross section (90° c.m.) with the phase-shift predictions of SAID [2]) Winter 82 (solid line), SAID Winter 81 (dotted line) and BASQUE [4]) (dashed line). The triangular data point at 500 MeV is calculated from the beam counter data.

A "single-energy" solution at 450 MeV (based on data within a 50 MeV bin) was compared over this time frame. The cross-section prediction decreased by only 0.2% (from 3.623 to 3.615 mb/sr) although the errors assigned decreased from 1.6% to 1.1% from the earlier version to the later version.

The assistance of Mrs. D. Sample in the data analysis and Mr. C. Chan in the design of the vacuum vessel is gratefully acknowledged. This work is supported in part by the Natural Sciences and Engineering Research Council of Canada.

References

1) G. Giles, E.G. Auld, W. Falk, G. Jones, G.J. Lolos, B.J. McParland, D. Ottewell, P. Walden and W. Ziegler, Phys. Rev. C, submitted
2) R.A. Arndt and L.D. Roper, "SAID", Scattering analysis interactive dial-in (VPI, Blacksburg, 1982), and private communication
3) P. Chatelain, B. Favier, F. Foroughi, J. Hoftiezer, S. Jaccard, J. Piffaretti, P. Walden and C. Weddigen, J. Phys. 8 (1982) 643
4) R. Dubois, D. Axen, D.V. Bugg, A.S. Clough, M. Comyn, J.A. Edgington, R. Keeler, G.A. Ludgate, J.R. Richardson and N.M. Stewart, Nucl. Phys. A377 (1982) 554

APPENDIX II: THE MONTE CARLO

II.1 INTRODUCTION

Monte Carlo techniques were used to evaluate the solid angle integrals defined in the text. This method of numerical integration was more capable of evaluating the effective solid angles characterizing the system (solid angles depending on complex physical properties) than could be accomodated analytically. Thus, models (such as that of the pion component of the effective solid angle, $\Delta\Omega_{\pi}^{*}$) based on simplifying assumptions could be verified. Furthermore, the muon component of the effective solid angle could only be evaluated using a Monte Carlo technique.

The event detection efficiency was not known explicitly; therefore it was integrated implicitly. Since the event detection efficiency is an implicit function of the apparatus geometry and material, the solid angle integral could be evaluated by simulating events, and tracking the particles through the apparatus to their detection point, if any. In-flight, the particles were subject to the geometrical constraints of the apparatus (for example; walls and apertures) in addition to the simulated influence of pion-decay, multiple-scattering, and energy-loss interactions. Since any of these processes could be removed from the simulation, it was possible to determine which processes or constraints were most significant. In the Monte Carlo system used, randomly distributed particle directions were generated over a given solid angle in the center-of-mass system. The particles were then tracked and the effective solid angle determined from the fraction of particles detected. Two such systems (computer programs) designated PEPI, and REVMOC[47], each with different capabilities were utilized:

1) PEPI: Designed for a two arm detector. This system was capable of simulating:

- A two-arm detection system; both the pion and deuteron were tracked.
- Energy-loss effects <u>not</u> included.
- Small-angle multiple scattering (optional)
- Pion decay (optional)
- A finite size beam spot
- A finite beam energy distribution width.

2) REVMOC[47]: A general purpose beam (particle) transport system supported and maintained at TRIUMF. With supplementary routines developed where necessary, it could simulate:

- A quasi-two arm system; Events with deuterons that would escape detection on the basis of their <u>initial</u> direction only were rejected. Otherwise the deuteron was assumed detected, and only the pion tracked in detail.
- Energy-loss effects (optional)
- Small angle multiple scattering (optional)
- Pion decay (optional)

- A finite size beam spot
- A monochromatic proton beam energy distribution was required.

REVMOC[47] in its original form was not capable of simulating the experiment. It was unable to duplicate the correct random pion momentum and angular coordinate distributions. Furthermore, it was inherently oriented to a one-arm system; that is, it could only track one of the two particles required. The following improvements were thus implemented. The angular coordinates of correlated pions and deuterons were evenly distributed over a given solid angle in the center-of-mass system. These angular coordinates and the associated particle momenta were then transformed into the laboratory system. The resulting deuteron coordinates were then examined and a test performed to determine whether the deuteron would hit the deuteron detector. If it did not, the event was rejected. Thus, the assumption that the deuteron travelled in a straight line was enforced, and REVMOC[47] was not required to track the second particle (the deuteron) in detail. If the deuteron was detected, the coordinate system, initially with the Z-axis in the beam direction, was rotated about the vertical (Y-axis) such that the Z-axis direction was along the central axis of the pion detector system. Finally, the momenta and resultant angular coordinates associated with the pions were transferred to REVMOC[47] which carried out the tracking of the pion through the remaining arm.

II.2 APPARATUS GEOMETRY AND MATERIAL

The apparatus was divided into elements or regions in the format required by the Monte Carlo systems. Each region of a detection arm was defined by a section of uniform material. In general, the material contained within each region was different from that of the region on either side. Table (1) shows an example. The depth of a region (Z) corresponds to the length of the material along the central axis of the arm. The other two dimensions define a rectangular aperture associated with each region. Particles passing outside of an aperture were considered stopped.

The physical properties of the materials are listed in Table (1b). REVMOC[47] only considers a material specified by three or less atomic species (elements). Thus, the composition of some materials (eg. magic gas) were approximated by the three dominant species indicated in Table (1b).

II.3 PHYSICAL INTERACTIONS

The three physical interactions invoked were pion decay, small-angle multiple-scattering, and energy-loss. A description of these processes is given in the appendix of the REVMOC[47] documentation which is reproduced in Table (2). When both the energy-loss and pion decay interactions were invoked (within REVMOC[47]) subsequent energy-loss of the muons subsequent to the pion decay was disregarded. This omission was corrected with the following method. Since most

Table 1

1a) DEFINITION OF A DETECTION ARM BY REGIONS

REGION		DIMENSION				
#	description	Z (cm)	X (cm) to	< from	Y (cm) to	< from
1	TARGET	0.088	1.0	-1.0	1.0	-1.0
2	VACUUM	0.507	30.0	-30.0	30.0	-30.0
3	MYLAR #1	0.025	40.7	-40.7	6.4	-6.4
4	AIR #1	8.468	100.0	-100.0	100.0	-100.0
5	MYLAR #2	0.025	100.0	-100.0	100.0	-100.0
6	MAGIC GAS #1	0.925	100.0	-100.0	100.0	-100.0
7	CATHODE #1	0.006	100.0	-100.0	100.0	-100.0
8	MAGIC GAS #2	0.472	100.0	-100.0	100.0	-100.0
9	ANODE	0.002	5.0	-5.0	5.0	-5.0
10	MAGIC GAS #3	0.472	100.0	-100.0	100.0	-100.0
11	CATHODE #2	0.006	100.0	-100.0	100.0	-100.0
12	MAGIC GAS #4	0.925	100.0	-100.0	100.0	-100.0
13	MYLAR #3	0.025	100.0	-100.0	100.0	-100.0
14	AIR #2	5.476	100.0	-100.0	100.0	-100.0
15	WRAPPING #1	0.066	100.0	-100.0	100.0	-100.0
16	SCINTILLATOR #1	0.159	6.35	-6.35	6.35	-6.35
17	WRAPPING #2	0.066	100.0	-100.0	100.0	-100.0
18	AIR #3	1.539	100.0	-100.0	100.0	-100.0
19	WRAPPING #3	0.066	6.35	-6.35	6.35	-6.35
20	SCINTILLATOR #1	0.683	6.35	-6.35	6.35	-6.35

The geometry of a typical pion arm is defined by the above regions.

1b) TABLE OF ASSUMED PHYSICAL PROPERTIES OF THE MATERIALS

MATERIAL	ATOMIC COMPOSITION	DENSITY g/cm^3	COMMENTS
Polyethylene	$(CH_2)n$	0.93	Target
Mylar	$C_5H_4O_2$	1.39	Used for wrapping
Air	$1O_2 + 4N_2$	0.00121	
Magic Gas	70% Ar + 30% C_4H_{10}	0.00200	Ratios by volume
Cathode wires	Be + Cu	5.40	
Anode wires	Au + W	19.3	
Scintillators	(CH)n	1.032	

The composition of the materials above has, in some cases, been approximated.

of the pions decay prior to the first scintillator, the integrated areal density of the system from this point on was calculated. A cut-off muon energy was defined, below which muons could not be expected to traverse the detector. The final number of successful events was then reduced by the number of muons with energies below the cut-off value resulting in a proportional drop of the muon effective solid angle.

APPENDIX 3: ANALYZING POWER OF THE pp→π^+d AT 375, 450, AND 500 MEV INCIDENT PROTON ENERGIES.

RAPID COMMUNICATIONS

PHYSICAL REVIEW C VOLUME 28, NUMBER 6 DECEMBER 1983

Analyzing power of the $\vec{p}p \to \pi^+d$ reaction at 375, 450, and 500 MeV incident proton energies

G. L. Giles, E. G. Auld, G. Jones, G. J. Lolos, B. J. McParland, and W. Ziegler

Physics Department, University of British Columbia, Vancouver, British Columbia, Canada V6T 2A6

D. Ottewell and P. Walden

TRIUMF, 4004 Wesbrook Mall, Vancouver, British Columbia, Canada V6T 2A3

W. R. Falk

Physics Department, University of Manitoba, Winnipeg, Manitoba, Canada R3T 2N2

(Received 4 April 1983)

The analyzing power A_{N0} of the $\vec{p}p \to \pi^+d$ reaction was measured to a statistical precision of better than ± 0.01 at incident proton beam energies of 375, 450, and 500 MeV, for center-of-mass angles from 20° to 150°. The polarization-dependent differential cross sections were fitted by associated Legendre functions (using published data for the shapes of the unpolarized differential cross sections). The energy dependence of the resulting b_k^{N0} coefficients were compared with existing data and theoretical expectations.

[NUCLEAR REACTIONS $\vec{p}p \to \pi^+d$; polarized protons; $E=375$, 450, 500 MeV; measured $A_{N0}(E,\theta)$; $\theta=20$–150° c.m.; deduced $b_1^{N0}(E) - b_5^{N0}(E)$.]

The $pp \to \pi^+d$ reaction is the simplest pion production process that can be studied. Because the inverse reaction represents the elementary pion absorption process, knowledge of the reaction is therefore an essential ingredient to understanding the absorption of low energy pions in nuclei.[1] Much recent interest in the reaction has been associated with the fact that the study of the $pp \to \pi^+d$ channel provides a major source of information towards the understanding of the complete nucleon-nucleon system. The importance of spin-dependent observables of the nucleon-nucleon system has been enhanced by the observation of unexpected energy dependence of the $\Delta\sigma_L$ and $\Delta\sigma_T$ parameters of the proton-proton subsystem.[2,3] Exotic reaction mechanisms, such as those which include a highly inelastic intermediate state that contains a so-called "dibaryon resonance," have been proposed to explain this type of observation.[4] If such a mechanism should exist, it could be expected to manifest itself in the inelastic $pp \to \pi^+d$ nucleon-nucleon channel. In fact, spin-dependent observables (such as the analyzing power) provide particularly stringent constraints on the theoretical models constructed to describe the $pp \to \pi^+d$ reaction.[5] Existing theoretical models fail to provide an adequate description of the precision data from 517–578 MeV.[6] At lower energies, nearer threshold, where a theoretical description should be simpler because of the reduced number of angular momentum components, no precision analyzing power data exist over a range of angles sufficient to permit a definitive comparison with existing theories.[7]

In this paper we present analyzing powers with statistical precision of better than ± 0.01 over a wide angular range for the incident proton energies 375, 450, and 500 MeV. The analyzing power data presented here were collected together with extensive measurements of the unpolarized differential cross section, a body of results which is currently being analyzed.

The experiment was mounted on an external proton beam line at the TRIUMF cyclotron. The polarization of the beam was continuously monitored during the experimental runs using an upstream polarimeter which monitored the asymmetry of $\vec{p}p$ elastic scattering. The beam intensity was measured by a number of devices, the most important of which involved the detection of the 90° [center-of-mass (c.m.)] elastically scattered protons from the target itself.[8] The time of flight, energy-loss, and angular coordinates of coincident deuterons and pions were measured with a two-arm detection system for pions with center-of-mass angles between 20° and 150°. A single 38.3 mg/cm^2 polyethylene $[(CH_2)_n]$ target was used for all the pion production measurements. Data were also obtained from a 24.9 mg/cm^2 carbon target in order to delineate the contribution of the carbon background. Each of the arms used for detecting the pion and deuterons consisted of a pair of thin scintillation counters together with a multiwire proportional chamber used for determining the angular coordinates of the trajectories. The hardware event definition consisted of (any) threefold coincidence of the four scintillators. Thus the efficiencies of all detectors could be extracted from the data. The data were recorded on magnetic tape for subsequent off-line analysis. Only time-of-flight and energy-loss constraints were required for the off-line event definition for the 375 MeV data. Only a small (typically 0.01) correction to the analyzing power resulted from the carbon subtraction. For the 450 and 500 MeV data, additional angular correlation and angular coplanarity constraints were applied with the result that no carbon background subtractions were required. In all cases, the error in the analyzing powers associated with both carbon background and counting statistics is less than ± 0.01. In addition, an overall systematic uncertainty of 2% for the 375 and 450 MeV data and 4% for the 500 MeV data arises from uncertainties in the polarimeter calibration.[9]

Figure 1 depicts the analyzing power data reported in this paper, together with those of W. R. Falk *et al.*[10] at 450 MeV. The agreement of the two 450 MeV data sets is excellent. Although the data of Ref. 10 are also from TRI-

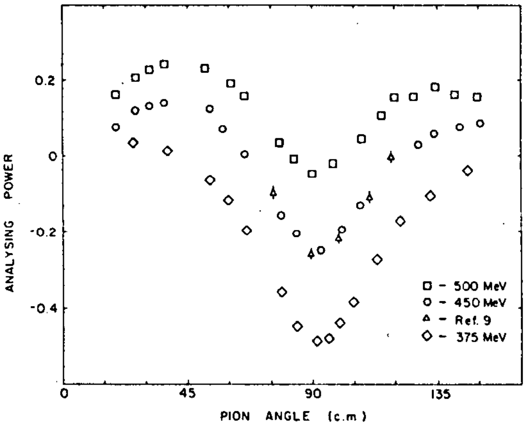

FIG. 1. Analyzing power for the $\vec{p}p \rightarrow \pi^+d$ reaction as a function of the pion angle (c.m.). The error bar is smaller than the corresponding symbol unless otherwise indicated. The data of Ref. 10 at 450 MeV are included.

UMF, they were obtained on a different beam line with a single-arm experimental configuration employing a magnetic spectrometer.

The analyzing powers at each energy were combined as shown in Eq. (1) with an estimate of the differential cross section (i.e., values of a_j/σ, where σ is the total cross section) obtained from published data,[7] and fit using associated Legendre functions to yield the b_k^{N0}/σ coefficients.[7,11] These normalized b_k^{N0}/σ coefficients are referred to in this paper as b_k coefficients, unless otherwise noted:

$$A_{N0}(\theta) \sum_{\text{even } j} \frac{a_j}{\sigma} P_j(\cos\theta) = \sum_k \frac{b_k^{N0}}{\sigma} P_k^1(\cos\theta) \ . \qquad (1)$$

The resulting b_k coefficients are plotted in Figs. 2(a) and 2(b), along with the results of J. Hoftiezer *et al.*[6] (for $\eta > 1.3$) and those of Mathie *et al.*[12] (for $\eta \leq 1$) as functions of η, where η represents the pion momentum (c.m.) in units of $m_\pi c$. The error bars shown for our b_k coefficients are those associated with the carbon background subtraction and counting statistics only. The sensitivity of the b_k coefficients to variations within reasonable limits of the a_j coefficients, and to the inclusion of an additional b_k term in the series, was found to be less than 0.01 for the odd terms, whereas for the even terms they were the order of the indicated error bars at 375 and 500 MeV, and up to twice that of the error bars at 450 MeV. The 500 MeV results presented here are completely consistent with the trends established by the precision data obtained at somewhat higher energy by J. Hoftiezer *et al.*[6] The momentum dependence of the odd b_k coefficients is smooth over the indicated η region, with a marked increase in the b_5 coefficient resulting for η greater than 0.75. No precise values for the even k terms, which are an order of magnitude smaller than the odd k terms, have been reported for η less than 1.3. Our data clarify this situation. For example, for the case of b_2^{N0}/σ, the data indicate a shoulder on the otherwise increasing b_2^{N0}/σ coefficient for η between 0.75 and 1.25, as well as a noticeable increase in the b_4^{N0} coefficient for η greater than 1. Although the model of Niskanen,[13]

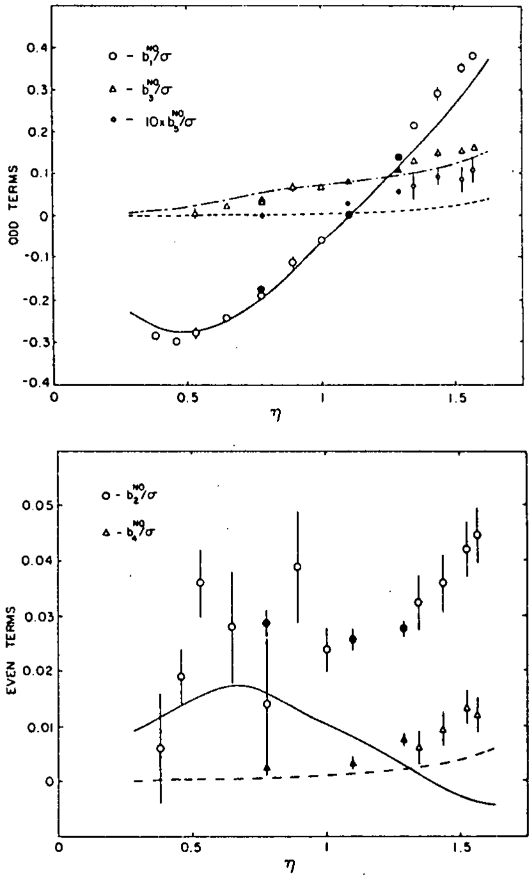

FIG. 2. Coefficients b_k^{N0}, of the associated Legendre functions relative to the total cross section σ, as a function of the pion momentum (c.m.) η. The solid symbols represent our results [the b_5^{N0} coefficient at 375 MeV ($\eta = 0.774$) is set to zero]. The remaining symbols represent the results of Ref. 1 for η less than 1 and Ref. 6 for η greater thaan 1.3. In (a) the solid line depicts a Niskanen (Ref. 13) prediction for b_1^{N0}/σ, the dashed curve for b_3^{N0}/σ, and the dotted curves for $10 \times b_5^{N0}/\sigma$. In (b) the solid curve is the prediction for b_2^{N0}/σ and the dashed curve for b_4^{N0}/σ. The error bars include only the uncertainties associated with the counting statistics and the background subtraction.

which is based on a coupled-channel formalism for the treatment of the $N\Delta$ intermediate state, provides a good overall description of the energy dependence of the polarization-dependent cross section, the theoretical values of the b_k coefficients are generally more negative than observed experimentally. In addition, the experimental value of the b_2 coefficients fails to cross zero in the neighborhood of $\eta = 1.5$ as predicted by Niskanen. As the quality of the experimental data improves, it is becoming increasingly clear that the present theoretical models require refinement, even in the near-threshold region pertinent to these measurements. This indicates a clear need for more theoretical effort, as well as further experimental measurement of the various $pp \rightarrow \pi^+d$ reaction parameters.

The extensive assistance of D. Sample and C. Grein in the data analysis is gratefully acknowledged. This work was supported in part by the Natural Sciences and Engineering Research Council of Canada.

[1]A. W. Thomas and R. H. Landau, Phys. Rep. 58, 121 (1980).

[2]I. P. Auer, E. Colton, H. Halpern, D. Hill, H. Spinka, G. Theodosiou, D. Underwood, Y. Watanabe, and A. Yokosawa, Phys. Rev. Lett. 41, 354 (1978).

[3]E. K. Biegert, J. A. Buchanan, J. M. Clement, W. H. Dragoset, R. D. Felde, J. H. Hoftiezer, K. R. Hogstrom, J. Hudomalj-Grabitzsch, J. S. Lesikar, W. P. Madigan, G. S. Mutchler, G. C. Phillips, J. B. Roberts, and T. M. Williams, Phys. Lett. 73B, 235 (1978).

[4]H. Hidaka, A. Beretvas, K. Nield, H. Spinka, D. Underwood, Y. Watanabe, and A. Yokosawa, Phys. Lett. 70B, 479 (1977).

[5]M. Betz, B. Blankleider, J. A. Niskanen, and A. W. Thomas, in *Pion Production and Absorption in Nuclei—1981 (Indiana University Cyclotron Facility)*, Proceedings of the Conference on Pion Production and Absorption in Nuclei, AIP Conf. Proc. No. 79, edited by R. D. Bent (AIP, New York, 1982), p. 65.

[6]J. Hoftiezer, C. Weddigen, P. Chatelain, B. Favier, F. Foroughi, J. Riffaretti, S. Jaccard, and P. Walden, Phys. Lett. 100B, 462 (1981).

[7]G. Jones, in Ref. 5, p. 15.

[8]D. Ottewell, P. Walden, E. G. Auld, G. L. Giles, G. Jones, G. J. Lolos, B. J. McParland, W. Ziegler, and W. R. Falk (unpublished).

[9]R. Dubois, M.Sc. thesis, University of British Columbia, 1978.

[10]W. R. Falk, E. G. Auld, G. Giles, G. Jones, G. J. Lolos, P. Walden, and W. Ziegler, Phys. Rev. C 25, 2104 (1982).

[11]J. A. Niskanen, in *Polarization Phenomena in Nuclear Physics—1980 (Fifth International Symposium, Santa Fe)*, Proceedings of the Fifth International Symposium on Polarization Phenomena in Nuclear Physics, AIP Conf. Proc. No. 69, edited by G. G. Ohlson, R. E. Brown, N. Jarmie, M. W. McNaughton, and G. M. Hale (AIP, New York, 1981), p. 62.

[12]E. L. Mathie, G. Jones, T. Masterson, D. Ottewell, P. Walden, E. G. Auld, A. Haynes, and R. R. Johnson, Nucl. Phys. A397, 469 (1983).

[13]J. A. Niskanen, Nucl. Phys. A298, 417 (1978); Phys. Lett. 79B, 190 (1978).

LIST OF REFERENCES

[1] *Pion Production and Absorption in Nuclei--1981 (Indiana University Cyclotron Facility)*, Proceedings of the Conference on Pion Production and Absorption in Nuclei, AIP Conf. Proc. No. 79, edited by R. D. Bent (AIP, New York, 1982), p. 65.

[2] A. W. Thomas and R. H. Landau, Phys. Rep. 58, 121 (1980).

[3] D.F. Measday and G.A. Miller Ann. Rev. Nucl. Part. Sci. 29, 121 (1979)

[4] I. P. Auer, E. Colton, H. Halpern, D. Hill, H. Spinka, G. Theodosiou, D. Underwood, Y. Watanabe, and A. Yokosawa, Phys. Rev. Lett. 41, 354 (1978).

[5] E.K. Biegert, J. A. Buchanan, J. M. Clement, W. H. Dragoset, R. D. Felde, J. H. Hoftiezer, K. R. Hogstrom, J. Hudomalj-Grabitzsch, J. S. Lesikar, W. P. Madigan, G.S. Mutchler, G. C. Phillips, J. B. Roberts, and T. M. Williams, Phys. Lett. 73B, 235 (1978).

[6] H. Hidaka, A. Beretvas, K. Nield, H. Spinka, D. Underwood, Y. Watanabe, and A. Yokosawa, Phys. Lett. 70B, 479 (1977).

[7] D.V. Bugg, Nucl. Phys. A416 227 (1984).

[8] M.P. Locher, Nucl. Phys. A416 243 (1984).

[9] G. L. Giles, E. G. Auld, G. Jones, G. J. Lolos, B. J. McParland, and W. Ziegler, Phys. Rev. C 28, 2551 (1983).

[10] D. Ottewell, P. Walden, E. G. Auld, G. L. Giles, G. Jones, G. J. Lolos, B. J. McParland, W. Ziegler, and W. R. Falk, Nucl. Phys. A412, 189 (1984).

[11] C. Weddigen, Nucl. Phys. A312, 330 (1978).

[12] F. Foroughi, J. Phys. G: Nucl. Phys. 8, 1345 (1982).

[13] C. Bourrely, E. Leader, and J. Soffer, Phys. Rep. 59, 95 (1980).

[14] F. Mandl and T. Regge, Phys. Rev. 99, 1478 (1955).

[15] B. Blankleider and I. R. Afnan, *Manuscript submitted for publication.*

[16] A. H. Rosenfeld, Phys. Rev. 96, 139 (1954).

[17] S. Mandelstam, Proc. Roy. Soc. A244, 491 (1958).

[18] J. A. Niskanen, in *Polarization Phenomena in Nuclear Physics--1980 (Fifth International Symposium, Santa Fe)*, Proceedings of the Fifth International Symposium on Polarization Phenomena in Nuclear Physics, AIP Conf. Proc. No. 69, edited by G. G. Ohlson, R. E. Brown, N. Jarmie, M. W. McNaughton, and G. M. Hale (AIP, New York, 1981), P. 62.

[19] M. Betz, B. Blankleider, J. A. Niskanen, and A. W. Thomas, in *Pion Production and Absorption in Nuclei--1981 (Indiana University Cyclotron Facility)*, Proceedings of the Conference on Pion Production and Absorption in Nuclei, AIP Conf. Proc. No. 79, edited by R. D. Bent (AIP, New York, 1982), p. 65.

[20] D. A. Geffen, Phys. Rev. 99, 1534 (1955).

[21] G. Chew et al., Phys. Rev. 84, 581 (1951).

[22] D. B. Lichtenberg, Phys. Rev. 105, 1084 (1957).

[23] A. M. Green and J. A. Niskanen, Nucl. Phys. A271, 503 (1976).

[24] J. A. Niskanen, Nucl. Phys. A298, 417 (1978).

[25] J. A. Niskanen, Phys. Lett. 79B, 190 (1978).

[26] I. R. Afnan and A. W. Thomas, Phys. Rev. C10 109 (1974).

[27] T. Mizutani and D. Koltun, Ann. Phys. 109 1 (1977).

[28] M.K. Craddock, Nature 270, 671 (1978)

[29] W. Ziegler M.Sc. thesis, University of British Columbia, 1978.

[30] G. Charpak, Ann. Rev. Nucl. Sci. 20, 195 (1970)

[31] T. Miles and A. Safanove, IEEE Trans. Nucl.Sci. NS-30, 3746 (1983).

[32] U. Fano, Ann. Rev. Nucl. Sci. 13, 1 (1963).

[33] Handbook of Mathematical Tables with Formulas, Graphs and Mathematical Tables, edited by Milton Abramowitz and Irene A. Stegun (Department of Commerce, United States of America, 1964) p. 17

[34] W.R. Falk, E.G. Auld, G. L. Giles, G Jones, G. Lolos W. Ziegler and P.L. Walden *Manuscript submitted for publication.*

[35] G. Jones (Alis Indiana Jones), in *Pion Production and Absorption in Nuclei--1981 (Indiana University Cyclotron*

Facility), Proceedings of the Conference on Pion Production and Absorption in Nuclei, AIP Conf. Proc. No. 79, edited by R. D. Bent (AIP, New York, 1982), p. 65.

[36] F. James and M. Roos, Computer Physics Communications 10, 343 (1975).

[37] P. R. Bevington, Data Reduction and Error Analysis for the Physical Sciences (McGraw-Hill Book Co., Inc., New York, 1969), p. 200.

[38] G. Jones, Nucl. Phys. A416 157 (1984).

[39] B. Blankleider and I. R. Afnan Phys. Rev. C24, 1572 (1981).

[40] Extracted from theoretical partial wave amplitudes supplied to G. Jones (private comunication)

[41] J. Hoftiezer, C. Weddigen, P. Chatelain, B. Favier, F. Foroughi, J. Riffaretti, S. Jaccard, and P. Walden, Phys. Lett. 100B, 462 (1981).

[42] B. G. Ritchie et al., Phys. Rev. C24, 552 (1981).

[43] C. L. Dolnick, Nucl. Phys. B22, 461 (1970).

[44] E. Rössle, private communication (1981).

[45] D Aebischer et al. Nucl. Phys. B108, 214 (1976).

[46] E. L. Mathie, . Jones, T. Masterson, D. Ottewell, P. Walden, E. G.·Auld, A. Haynes, and R. R. Johnson, Nucl. Phys. A397, 469 (1983).

[47] C. Kost and P Reeve, TRIUMF Design Note, 1982, (unpublished); and references contained within.

Gordon Giles

REFEREED PAPERS IN SCIENTIFIC JOURNALS

THE ANALYZING POWER OF THE $pp \rightarrow \pi^{+}d$ REACTION AT 375, 450, AND 500 MeV INCIDENT PROTON ENERGIES
G.L. Giles, E.G. Auld, G. Jones, G.J. Lolos, B.J. McParland, W. Ziegler, D. Ottewell, P. Walden, and W. Falk.
Phys. Rev. C28 (1983) 2551

THE DIFFERENTIAL CROSS-SECTION FOR PROTON-PROTON ELASTIC SCATTERING AT 90° c.m. BETWEEN 300 AND 500 MeV
D. Ottewell, P. Walden, E.G. Auld, G.L. Giles, G. Jones, G.J. Lolos, B.J. McParland, W. Ziegler and W. Falk.
Nucl. Phys. A412 (1984) 189

ANGULAR DEPENDENCE OF THE $^{6}Li(\pi^{+}, ^{3}He)^{3}He$ REACTION AT 60 AND 80 MeV
B.J. McParland, E.G. Auld, P. Couvert, G.L. Giles, G. Jones, X. Aslanoglou, G.M. Huber, G.J. Lolos, S.I.H. Naqvi, Z. Papandreou, P.R. Gill, D.F. Ottewell, and P.L. Walden.
Manuscript submitted for publication to Physics Letters.

POLARIZED-PROTON-INDUCED EXCLUSIVE PION PRODUCTION IN ^{12}C AT 200, 216, 225, 237 AND 250 MeV INCIDENT ENERGIES
G.J. Lolos, E.G. Auld, W.R. Falk, G.L. Giles, G. Jones, B.J. McParland, R.B. Taylor, and W. Ziegler.
Phys. Rev. C30 (1984) 574

ANALYSING POWER OF THE $pp \rightarrow \pi^{+}d$ REACTION AT 400 AND 450 MeV
W.R. Falk, E.G. Auld, G.L. Giles, G. Jones, G.J. Lolos, P.L. Walden and W. Ziegler.
Phys. Rev. C25 (1982) 2104

ANALYZING POWER OF THE $pp \rightarrow \pi^{+}t$ REACTION AT 305, 330, 375 AND 400 MeV
G.J. Lolos, E.L. Mathie, G. Jones, E.G. Auld, G.L. Giles, B.J. McParland, P.L. Walden, W. Ziegler, and W. Falk.
Nucl. Phys. A386 (1982) 477

PION PRODUCTION FROM DEUTERIUM BOMBARDED WITH POLARIZED PROTONS OF 277 and 500 MeV
G.J. Lolos, E.G. Auld, G.L. Giles, G. Jones, B.J. McParland, D. Ottewell, P.L. Walden, and W. Ziegler.
Nucl. Phys. A422 (1984) 582

SPECTROSCOPY OF DOUBLY RESONANT THIRD HARMONIC GENERATION IN I_2
L. Tai, F.W. Dalby, and Gordon L. Giles.
Phys. Rev. A20, (1978) 233